A SYSTEMATIC COMPARISON OF THE ANISOTROPY OF MAGNETIC SUSCEPTIBILITY (AMS) AND ANISOTROPY OF REMANENCE (ARM) FABRICS OF IGNIMBRITES:

EXAMPLES FROM THE QUATERNARY BANDELIER TUFF, JEMEZ MOUNTAINS, NEW MEXICO AND MIOCENE IGNIMBRITES NEAR GOLD POINT, NEVADA

by

Ranyah Lycka

APPROVED BY SUPERVISORY COMMITTEE:

____
Dr. John W. Geissman, Chair

____
Dr. Robert J. Stern

____
Dr. John F. Ferguson

A SYSTEMATIC COMPARISON OF THE ANISOTROPY OF MAGNETIC SUSCEPTIBILITY (AMS) AND ANISOTROPY OF REMANENCE (ARM) FABRICS OF IGNIMBRITES:

EXAMPLES FROM THE QUATERNARY BANDELIER TUFF, JEMEZ MOUNTAINS, NEW MEXICO AND MIOCENE IGNIMBRITES NEAR GOLD POINT, NEVADA

by

RANYAH LYCKA, BA

THESIS

Presented to the Faculty of

The University of Texas at Dallas

Submitted in Partial Fulfillment

of the Requirements

for the Degree of

MASTER OF SCIENCE IN

GEOSCIENCES

THE UNIVERSITY OF TEXAS AT DALLAS

August 2017

ACKNOWLEDGMENTS

I would like to give my advisor, Dr. John Geissman, a most profound thank you for his constant direction and encouragement over the last five years of being my professor and becoming my thesis advisor. You have helped me grow and become a better scientist.

I would also like to thank Dr. Robert Stern and Dr. Michael Ort for support and guidance not only throughout the completion of this thesis, but also throughout my continuing education at The University of Texas at Dallas.

I am grateful to the students in the Paleomagnetism research group and all who assisted me during my time at UT Dallas. Jacob Jackson, Dylan Collins, Brandon Lycka, Tom Fitter, Mike Martin, Kit Harper, Christopher Mace and Andrea Rhode, you all have been a support system for me and it was a pleasure working with all of you.

I also thank the Geological Society of America and the Department of Geosciences at The University of Texas at Dallas for financially supporting me and my research. Without the financial support, completing this project would not have been possible. I also would like to express my gratitude to Dr. Aviva Sussman, Elizabeth Miller, and Scott Muggleton for helping to make my field endeavors possible in Los Alamos.

April 2017

A SYSTEMATIC COMPARISON OF THE ANISOTROPY OF MAGNETIC SUSCEPTIBILITY (AMS) AND ANISOTROPY OF REMANENCE (ARM) FABRICS OF IGNIMBRITES:

EXAMPLES FROM THE QUATERNARY BANDELIER TUFF, JEMEZ MOUNTAINS, NEW MEXICO AND MIOCENE IGNIMBRITES NEAR GOLD POINT, NEVADA

Ranyah Lycka, MS
The University of Texas at Dallas, 2017

Supervising Professor: Dr. John W. Geissman

Anisotropy of magnetic susceptibility (AMS) has been widely used to define petrofabrics in silicic, elevated-temperature pyroclastic deposits (i.e., ignimbrites) and these fabrics have been successfully utilized to infer pyroclastic emplacement, or transport, directions in many cases. Selected exposures of the Quaternary Bandelier Tuff, exposed in the Jemez Mountains, New Mexico, have been studied to systematically compare anisotropy of remanence (mainly anhysteretic remanent magnetization, AARM) with AMS data from the same sites. In addition, as part of a broad study to understand the Neogene history of deformation associated with a displacement transfer system in the western Great Basin, paleomagnetic and magnetic fabric data have been collected from ignimbrites that originated from the Timber Mountain Caldera complex, active from about 14 to 11.5 Ma. Here, AMS and AARM are compared for 21 (9-12

samples per site) sites in the Quaternary Bandelier Tuff, and 15 (9-10 samples per site) sites in Timber Mountain ignimbrites, with each chosen to examine the effects of varying degrees of welding and crystal content on the fabrics obtained. The relationships between AARM and AMS fabrics for the selected sites are not uniform, and include normal, intermediate, reverse, and oblique fabrics. The differences may be controlled by the degree of welding and/or crystal content, which requires further explanation. Ultimately, the fabrics identified in both suites of rocks are compared with anisotropy of isothermal remanent magnetization (AIRM) data, along with other rock magnetic data, to more fully evaluate the domain state control on the fabrics.

TABLE OF CONTENTS

ACKNOWLEDGEMENTS iv

ABSTRACT v

LIST OF FIGURES ix

LIST OF TABLES xii

LIST OF ABREVIATIONS xiii

CHAPTER 1 INTRODUCTION 1

CHAPTER 2 REGIONAL GEOLOGY AND HISTORY 3
2.1 Jemez Volcanic Field, NM 3
2.2 Western Great Basin, Gold Point Area 11
2.3 Pyroclastic Density Currents 15

CHAPTER 3 MAGNETIC SUSCEPTIBILITY AND ANISOTROPY 18
3.1 Anisotropy of Magnetic Susceptibility (AMS) 18
3.2 Anisotropy of Magnetic Remanence 23

CHAPTER 4 PETROGRAPHY 26
4.1 Petrography of the Tshirege Member of the Bandelier Tuff 26

CHAPTER 5 METHODS 29
5.1 AMS 29
5.2 AARM 30
5.3 AIRM 30
5.4 Susceptibility vs Temperature 32
5.5 Hysteresis and FORC Diagrams 32

CHAPTER 6 RESULTS 34
6.1 AMS Fabric Information 34
    6.1.1 Bandelier Tuffs 39
    6.1.2 Tuffs of Gold Point 43
    6.1.3 AMS – Ignimbrite Density Comparison 49
6.2 Rock Magnetic Experiments 51
    6.2.1 IRM Acquisition and Backfield Demagnetization 51
    6.2.2 Magnetic Susceptibility vs. Temperature 54
    6.2.3 Magnetic Hysteresis Curves 64

6.2.4 First Order Reversal Curve (FORC) Diagrams 78
6.3 ARM Fabrics and Comparison of Anisotropy Methods 84
6.3.1 AIRM Fabrics 85
6.3.2 AARM Fabrics 86

CHAPTER 7 DISCUSSION 94
7.1 Comparison of AMS/ARM Fabrics 95

CHAPTER 8 CONCLUSIONS 107

REFERENCES 109

BIOGRAPHICAL SKETCH 117

CURRICULUM VITAE 118

LIST OF FIGURES

Figure 2.1 Regional map of the Rio Grande Rift localized near the Jemez Mountains 3

Figure 2.2 Sampling locations located on the Pajarito Plateau east of the Valles Caldera 6

Figure 2.3 Extent of Quaternary Bandelier Tuff in study area and site localities 7

Figure 2.4 Stratigraphic summary of the Bandelier Tuff pyroclastic deposits 8

Figure 2.5 Simplified map showing the location of the Gold Point/Slate Ridge area 12

Figure 2.6 Summary of Neogene stratigraphy and depositional relations of the Gold Mountain-Slate Ridge Area 13

Figure 2.7 Map of Gold Mountain/Slate Ridge (GMSR) area relative to Timber Mountain (TM), Stonewall Mountain (SM), and sampling locations used in this study 15

Figure 3.1 AMS susceptibility ellipse defining principal susceptibility axes (K_1, K_2, and K_3 tensors) and typical shapes associated with anisotropic ellipsoids 22

Figure 3.2 Normal and inverse magnetic fabrics with respect to the flow direction 25

Figure 4.1 Polished thin sections of representative Bandelier tuff photomicrographs on individual grains 28

Figure 5.1 Fifteen different measurement orientations modified from Tauxe, 1998 31

Figure 5.2 Comparisons of Hysteresis and First-Order Reversal Curves (FORC) 33

Figure 6.1 Flinn-type plot showing mean magnetic foliation plotted against mean magnetic lineation for all 21 sites in the Bandelier Tuff 36

Figure 6.2 Cross Plot of shape factor versus the degree of anisotropy for data from the 21 sites in the Bandelier Tuff 37

Figure 6.3 Flinn-type plot showing magnetic foliation versus magnetic lineation for the 14 sites in the Gold Point ignimbrites 37

Figure 6.4 Cross Plot of shape factor versus the degree of anisotropy for Gold Point ignimbrites 38

Figure 6.5 AMS ellipsoidal data and plotted arrows on map showing sampling localities representing K_1 azimuthal direction for all sites in Bandelier Tuff, with arrow pointing in the direction of plunge of K_1 39

Figure 6.6 AMS ellipsoidal data and plotted arrows on map showing sampling localities representing K_3 azimuthal directions with arrows pointing to the plunge of K_3 for all 21 sites in the Bandelier Tuff 40

Figure 6.7 Map of AMS Results for Gold Point Area Tuffs 43

Figure 6.8 Map of AMS Results for Gold Point Area Tuffs with lower hemisphere projections 44

Figure 6.9 Enlargement showing AMS susceptibility directions zoomed in from the condensed map. 45

Figure 6.10 AMS measurements for the Gold Point area ignimbrite 48

Figure 6.11 Bulk density compared with selected magnetic parameters (Bulk Susceptibility, T value, and percent anisotropy) 50

Figure 6.12 IRM acquisition and backfield demagnetization curves 53

Figure 6.13 Magnetic susceptibility versus temperature curves for Bandelier Tuff sites 61

Figure 6.14 Magnetic susceptibility versus temperature curves for Gold Point area sites 64

Figure 6.15 Day plot comparisons for Bandelier and Gold Point area ignimbrites 67

Figure 6.16 Hysteresis Curves 77

Figure 6.17 FORC Diagrams 83

Figure 6.18 The four relationships between AARM and AMS observed in this study 85

Figure 6.19 Comparison of AMS vs AARM data for Bandelier Tuff sites 93

Figure 7.1 Comparison of AMS, AIRM, and AARM data with black arrows indicating K1 flow directions and pink arrows indicating K3 flow direction 97

Figure 7.2 Comparison of AMS, AIRM, and AARM data for the four selected sites with AMS and AMR results 98

Figure 7.3 AMS P values compared to AARM and AIRM P values for Bandelier Tuff and Gold Point (GP) Tuffs 10

Figure 7.4 Lineation versus Foliation for Bandelier Tuff and Gold Point (GP) Tuffs 10

Figure 7.5 Lineation versus Foliation for Bandelier Tuff for the four selected sites with AMS and AMR results 101

Figure 7.6 Lineation versus Foliation for Gold Point Tuff for selected sites with AMS and AMR results 101

Figure 7.7 Comparison of AMS, AIRM, and AARM data with black arrows indicating K1 flow directions and pink arrows indicating K3 flow direction 105

Figure 7.8 Map showing Gold Point Tuff comparisons of AMS, AIRM, and AARM data of inferred K_1 transport directions 105

Figure 7.9 Map showing Gold Point comparison of AMS, AIRM, and AARM data with K_3 imbrication orientations 106

LIST OF TABLES

Table 3.1 AMS Parameters adopted from Winkler et al. 1997 20

Table 6.1 Summary of AMS Results for Bandelier Tuff (Principal Axes) 41

Table 6.2 Summary of AMS Results for Bandelier Tuff (Parameters) 42

Table 6.3 Summary of AMS Results for Gold Point Tuffs (Principal Axes) 46

Table 6.4 Summary of AMS Results for Gold Tuffs (Parameters) 47

Table 6.5 Magnetic Hysteresis Parameters for Bandelier Tuff 65

Table 6.6 Magnetic Hysteresis Parameters for Gold Point Tuffs 66

Table 6.7 Summary of AARM data for Bandelier Tuff and Gold Point area sites 88

Table 7.1 Comparison of AIRM, AARM and AMS data from the Bandelier Tuff and Gold Point Tuffs 99

LIST OF ABREVIATIONS

QBT	Quaternary Bandelier Tuff
GMSR	Gold Mountain/Slate Ridge
LANL	Los Alamos National Laboratory
SWNVF	Southwest Nevada Volcanic Field
PDC	Pyroclastic Density Current
AMS	Anisotropy of Magnetic Susceptibility
AMR	Anisotropy of Magnetic Remanence
ARM	Anhysteretic Remanent Magnetization
AARM	Anisotropy of Anhysteretic Remanent Magnetization
AIRM	Anisotropy of Isothermal Remanent Magnetization
IRM	Isothermal Remanent Magnetization
SIRM	Saturation of Isothermal Remanent Magnetization
SD	Single Domain
MD	Multi Domain
Km	Bulk Susceptibility
L	Magnetic Lineation
F	Magnetic Foliation
T	Shape Factor
P	Percent Anisotropy
K_1	Maximum Susceptibility Axis
K_2	Intermediate Susceptibility Axis
K_3	Minimum Susceptibility Axis
mT	Millitesla

CHAPTER 1

INTRODUCTION

Pyroclastic deposits, in particular elevated temperature pyroclastic density currents (PDCs) commonly refered to as ignimbrites, have been extensively studied to understand their emplacement processes, degree of welding, transport directions, and deposited fabrics including magnetic fabrics (Sparks et al, 1976; Wilson et al. 1982; Incontro et al. 1983; Knight et al. 1986; Palmer et al. 1996; Palmer and MacDonald 1999; Ort et al. 2003; Petronis and Geissman 2009; Agro et al. 2014). Anisotropy of magnetic susceptibility (AMS) is a relatively fast, quantitative method of investigating magnetic fabrics of rocks and has been used extensively to independently estimate the flow axis and thus source directions of ignimbrites, especially distal, out-flow facies (Ellwood, 1982; Macdonald and Palmer 1990). Anisotropy of remanence studies, which are more time-consuming, are far less commonly used to evaluate ignimbrite fabrics, yet they have the potential to provide more useful information on the grain size variations and shape distribution of the ferri/ferro magnetic population of oxide grains, and thus to a large degree what actually controls an AMS fabric (Hargraves et al. 1991; Jackson, 1991; Stephenson et al 1986; Martin-Hernandez 2004; Potter 2004). To provide an improved understanding of magnetic fabrics in ignimbrites, samples from the Quaternary Bandelier Tuff, exposed in the Jemez Mountains, New Mexico, have been collected to systematically compare anisotropy of remanence (mainly anhysteretic remanent magnetization, AARM) with anisotropy of magnetic susceptibility (AMS) data from the same sites. In addition, magnetic fabric data have been obtained from Miocene ignimbrites in western Nevada as part of a study to understand the Neogene history of deformation related to a displacement transfer system in the western Great

Basin, near the south part of the Walker Lane belt, Esmeralda County, Nevada. The relationship between AMS and anisotropy of remanence fabrics in these rocks offers insight into which approach provides data that are more indicative of actual emplacement related fabrics and a measure of anisotropy controlled by the magnetic oxides and overall petrofabric. AARM data can be advantageous when compared to AMS results, as remanence is typically more sensitive to mineral grains with higher degree of anisotropies (i.e., ferro/ferrimagnetic minerals) (Jackson 1991; Ferre 2002; Muxworthy et al. 2004; Potter 2004; Borradaile et al. 2010). The primary objective of studying the two suites of ignimbrite sheets of different ages and very different geologic settings is to develop a more comprehensive knowledge of how anisotropy of remanence defines the biasing alignment of ferro/ferrimagnetic mineral grains in ignimbrites. AMS, AARM, and anisotropy of isothermal magnetization (IRM) fabrics as well as saturation of IRM (SIRM), backfield demagnetization of SIRM and magnetic susceptibility as a function of temperature (χ vs T) data are compared for selected parts of each tuff sequence that exhibit a broad range of welding textures, crystal content, density and other features. The combination of approaches allows for a more accurate estimate of particle alignment and therefore an understanding of the fabrics and transport direction of the ignimbrites.

CHAPTER 2

REGIONAL GEOLOGY AND HISTORY

2.1 Jemez Volcanic Field, New Mexico

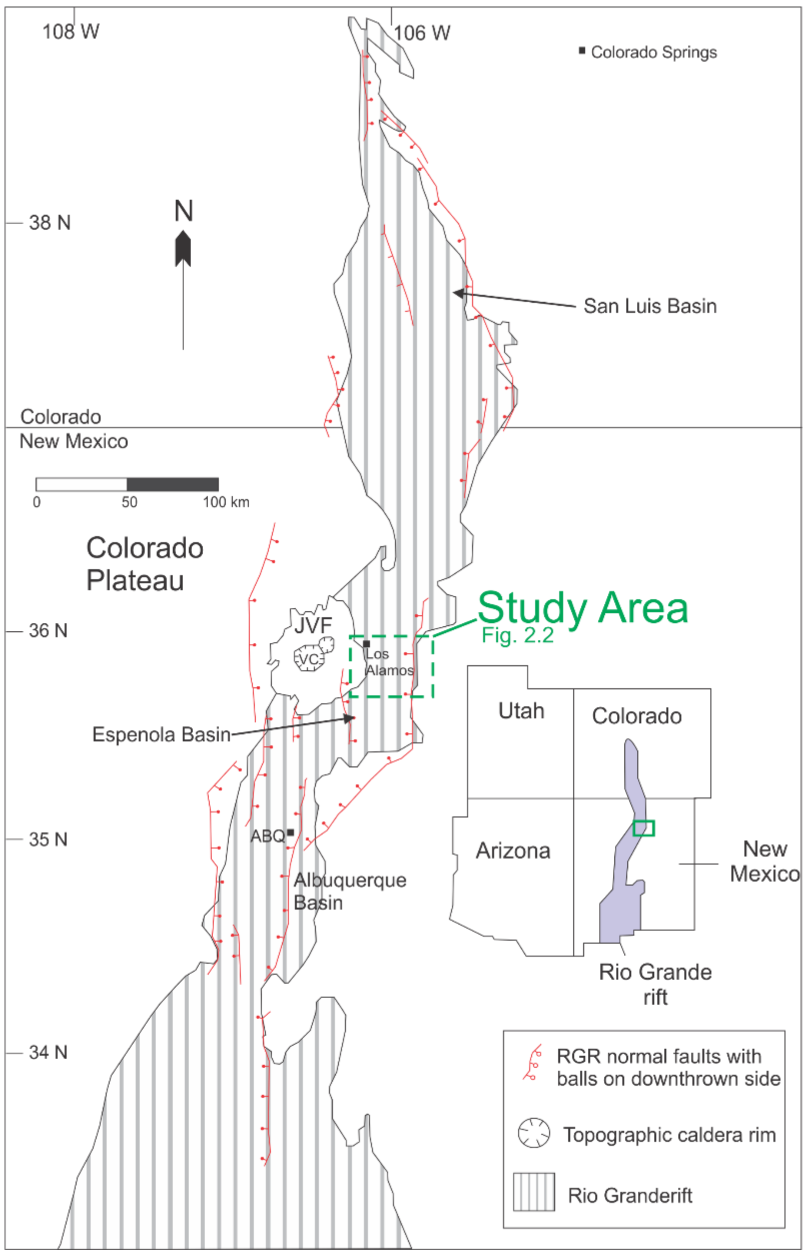

Figure 2.1. Regional map of the Rio Grande Rift localized near the Jemez Mountains.

The Quaternary Bandelier Tuff is a well-known, exceptionally well-exposed ignimbrite sequence consisting of two principal eruptive members, exposed in the Jemez Mountains, New Mexico (Smith and Bailey, 1966; Potter and Oberthal 1987; Turbeville and Self 1988; MacDonald and Palmer 1990; Spell et al. 1990; Broxton and Reneau, 1995; MacDonald and Palmer 1990; Gardner and Goff 1996; Gardner et al. 2007; Phillips et al. 2007; Goff 2014). This study concentrates on exposures in an area near Los Alamos National Laboratories (LANL), located on the Pajarito Plateau east of the Valles Caldera. The Jemez Mountains are situated on the western margin of the Rio Grande rift, west of the Espanola Basin and north of the Albuquerque Basin, and are bounded on the west side by the Colorado Plateau (Figure 2.1). The Rio Grande rift is a lithosphere scale feature that separates the Colorado Plateau from the craton interior. The rift includes four basins that are separated by right-stepping echelon faults that caused rift deformation from the mid-Miocene to the Quaternary (Chapin and Cather, 1996; Harlan and Geissman 2009). The Bandelier Tuff originated from two calderas in the Jemez Mountains, and has been extensively studied for many purposes, including paleomagnetism and magnetic fabrics. AMS data were reported by MacDonald and Palmer (1990) from relatively undisturbed (no observed rotations) outflow facies exposures of the Bandelier Tuff near the Valles Caldera to test the hypothesis that AMS fabrics could be used as a reliable indicator of emplacement transport directions. There has been no previous anisotropy of remanence work reported on the Bandelier Tuff.

The Bandelier Tuff is divided into two separate members associated with the collapse of the two major calderas, as described below. Both members were erupted during the Matuyama reverse polarity chron. The older member is the Otowi Member (~ 1.61 Ma) was erupted from the Toledo caldera, and it is overlain by the Cerro Toledo interval of tephras and volcaniclastic deposits, which are interpreted as a distinct unit from the Bandelier Tuff (Figure 2.4). The Tshirege Member of the Bandelier Tuff (~ 1.25 Ma) was erupted from the well-preserved Valles Caldera and consists of multiple cooling units (Doell, Dalrymple, Smith and Bailey, 1968; Bailey, Smith, and Ross, 1969; Phillips et al., 2007). The Bandelier Tuff thus consists of two temporally distinct ignimbrite deposits, each of which is divided into several sub-cooling units defined by differences in physical properties both vertically and laterally and with distance away from source calderas. Physical variations in the deposits are due to the progressive temperature loss during eruption, transport, and emplacement of the PDC and results in characteristics that differ proximally versus distally from the source (Crowe, 1978; Broxton and Reneau, 1995). The different cooling units of the Tshirege Member are very well exposed on the Pajarito Plateau, which slopes at a very gentle angle to the east-southeast and consists of a series of protruding mesas with deeply cut canyons that incise into the eastern rim of the Valles Caldera (Crowe et al, 1978). A single ignimbrite cooling unit is defined as the deposit of an ash-flow or sequence of ash flows that cooled as a single deposit with an uninterrupted cooling history (Smith, 1960a), such as the Otowi Member. A compound cooling unit, such as the Tshirege Member of the Bandelier Tuff, results from emplacement of successive packages that are attributed to an interrupted cooling history dividing the deposit into several distinct cooling units or intervals (Crowe, 1978; Sussman et al., 2011).

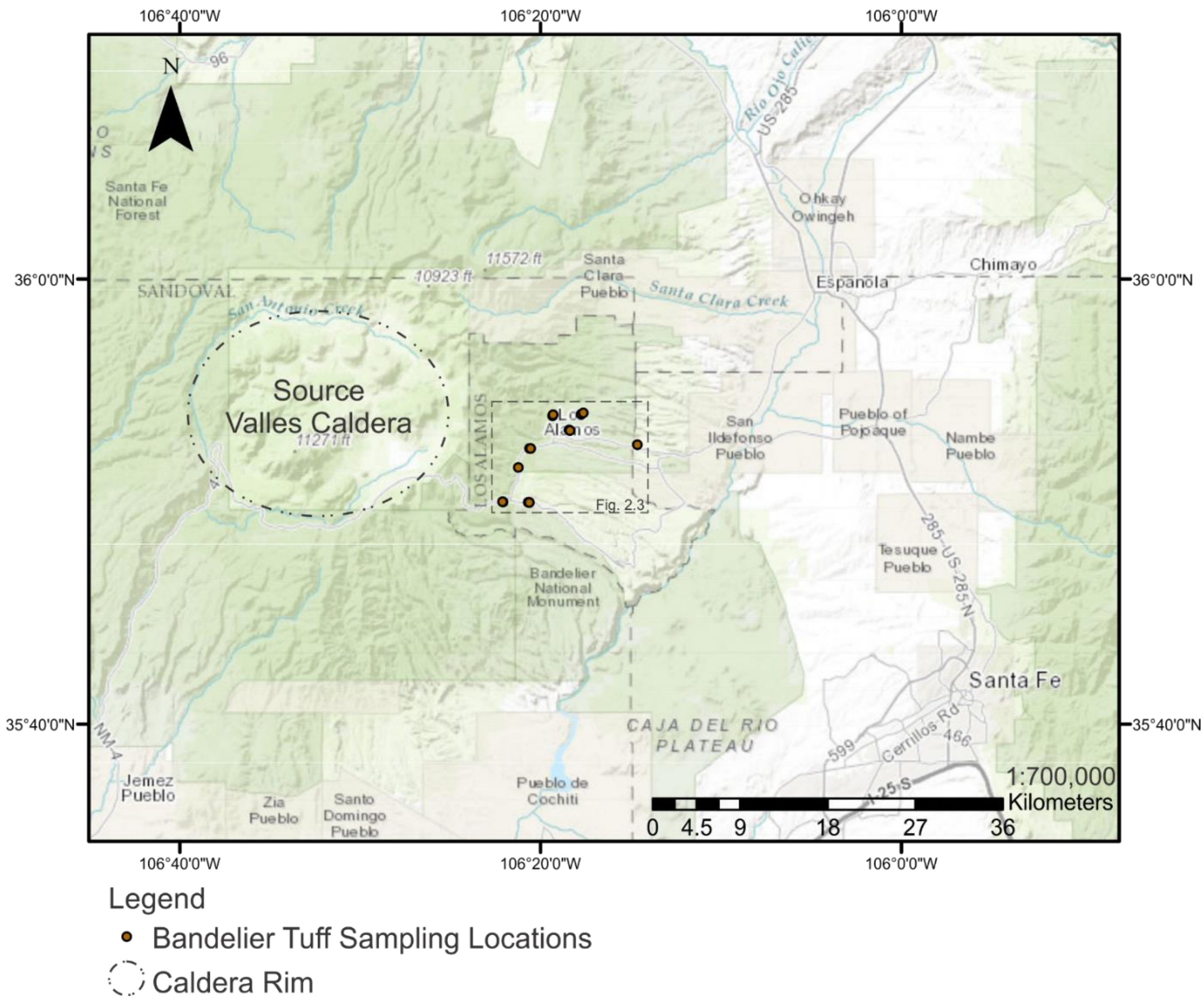

Figure 2.2. Map showing sampling locations on the Pajarito Plateau, east of the Valles Caldera

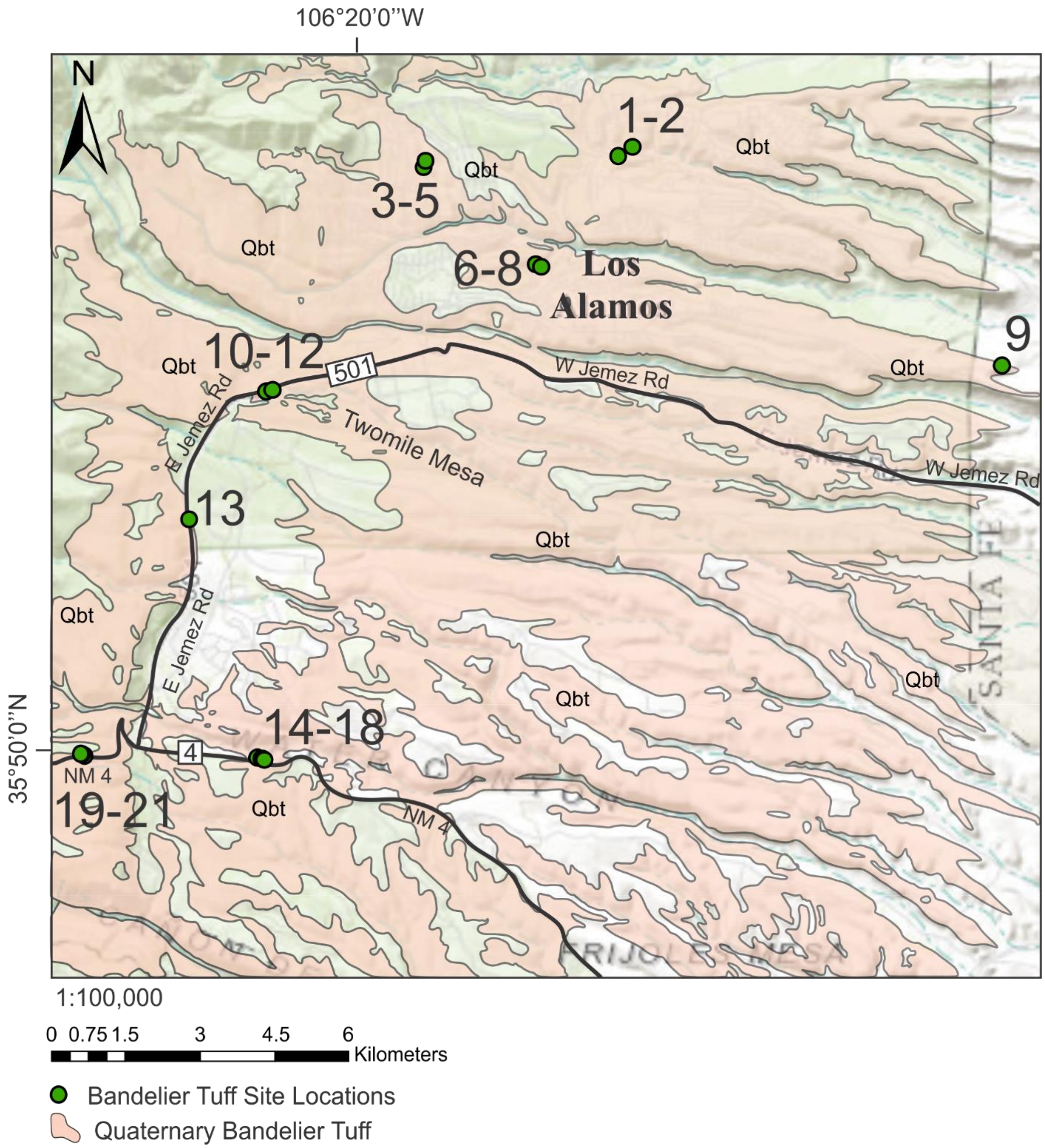

Figure 2.3. Map showing the extent of the Quaternary Bandelier Tuff in study area

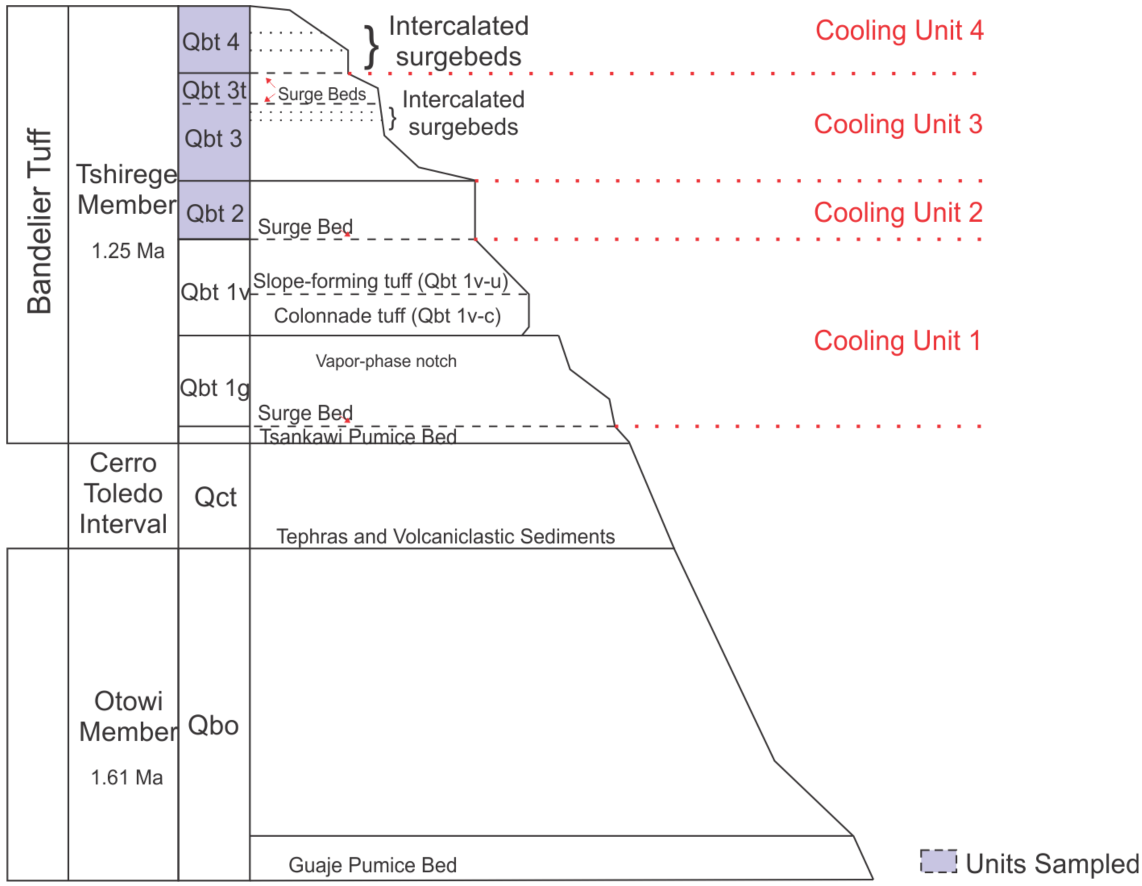

Figure 2.4. Stratigraphic summary of the Bandelier Tuff pyroclastic deposits. Modified from Sussman et al., 2011.

For this project and because of the overall nonwelded to poorly welded nature of the Otowi Member, only the Tshirege Member was sampled (Figure 2.2 and 2.3). The Tshirege Member is a compounded cooling unit succession of four very distinct ignimbrite cooling units (Figure 2.4). The overall stratigraphy of the Tshirege Member has been described by many authors (e.g., Smith and Bailey 1966, Baltz et al. 1963, Crow et al. 1978, Vaniman and Wohletz 1990; 1991, Goff 1995, and others), but with a lack of consistent nomenclature. Here I use the nomenclature of Broxton and Reneau (1995) and the more recent mapping of (Gardner et al.

1999) to be consistent with the most recent literature. The cooling units are defined by surface-weathering patterns, welding features, and crystallization characteristics (Broxton and Reneau, 1995). The Tshirege Member overlies the Cerro Toledo interval with its base being the Tsankawi Pumice Bed, a basal pumice fall that can be 20-100 cm thick. The Tshirege Member eruptive volume is about 250 km^3, and on the Pajarito Plateau, the Tshirege deposits have typical thicknesses of ~300 m, with local thicknesses of the Bandelier Tuff on the Pajarito Plateau up to ~1000 m (Sussman et al., 2011).

"The oldest Tshirege Member cooling unit is subdivided into two subunits, Qbt 1g (Quaternary-Bandelier-Tshirege 1 g = glassy) and Qbt 1v (Quaternary-Bandelier-Tshirege 1 v = vapor-phase crystallized tuff). Qbt 1g is characterized by abundant volcanic glass, lack of welding, and a light gray vitreous, pumice lapilli supported by a matrix of coarse ash, shards pumice fragments, and abundant (12-16%) quartz and sanidine phenocrysts (Broxton and Reneau, 1995). The top of unit 1g becomes more consolidated and forms a cliff-forming bench that marks the gradational transition between Qbt 1g and Qbt 1v. The base of Qbt 1v is a resistant orange to brown tuff that overlies the bench of Qbt 1g. Qbt 1v is further subdivided into two units (Qbt 1v-c, c=Colonnade) and (Qbt 1v-u, u= Upper). The colonnade tuff forms cliffs that are 3-10 meters high and are distinguished by vertical fractures. It consists of chocolate-brown to dark-purple gray pumice relicts with a matrix that is pinkish-white to light-gray and the pumice makes up 30-50% of the rock, whereas the upper forms a distinctive nonwelded grayish-white band of tuff that consist of light gray to medium gray pumice relicts with light gray matrix. Pumice makes up 30-50% of the rock (Broxton and Reneau, 1995).

Cooling unit 2 is a cliff forming, thick ash-flow tuff that is the most strongly welded unit of the Tshirege Member. It is characterized by gray to brown pumices that are smaller and less abundant (2-15%) in comparison to the underlying unit and those are supported by a light pink-tan matrix and lithic fragments are rare (<1%).. Crystals are more abundant than in unit 1 (17-32%) with coarse crystals of tridymite, quartz, and sanidine. A surge bed at the lower part of unit 2 is used to define the base from the top of Qbt 1v-u (Broxton and Reneau, 1995). The unit is mostly prominent in the eastern parts of Los Alamos and the unit disappears towards the western part (Gardner et al. 1999).

The contact between Qbt 2 and the overlying cooling unit Qbt 3 is abrupt and indicates a significant change in the degree of welding of the ignimbrites. The base of unit 3 is characterized by a nonwelded whitish colored tuff in comparison to the underlying strongly welded unit 2 (Broxton and Reneau, 1995). The upper part of Qbt 3 contains gray-brownish pumice relicts, abundant crystals and welding increases up section.

Qbt3t is further divided by Gardner et al. 1999 as a transitional unit between Qbt3 and the lower part of Qbt4. This unit is only mapped in the western parts of the laboratory area and pinches out toward central and eastern parts of the laboratory. Its thickness ranges from 0 to 35 feet in thickness. It is a very densely welded unit with a 20 to 30% crystal population, and is commonly separated by the overlying Qbt4, by a two feet thick, crystal rich surge deposit (Gardner et al. 1999).

Qbt 4 is not as prominent on the Pajarito Mesa, especially in the eastern LANL areas where it is likely missing due to erosion. It is a very distinctive unit as it consists of crystal rich pyroclastic surge beds overlain by pumice poor ignimbrites. The surge beds are prominent at the base of Qbt 4 and can be up to 15 cm thick with characteristic planar and low-angle cross beds (Broxton and Reneau, 1995). Qbt 4 is most easily distinguished from the other three underlying units by the lack of relict pumice (<5%) and lack of crystals (~8%)" (Broxton and Reneau, 1995).

2.2 Western Great Basin, Gold Point Area

The Gold Point area, southwest Nevada, is located in Esmeralda County in the western Great Basin. The area includes the east-west oriented Gold Mountain-Slate Ridge (GMSR) topographic features and is south of Lida Valley (Figure 2.5). The GMSR area includes exposures of several Cenozoic ignimbrite units that have been subsequently deformed as a result of mid-Miocene and younger faulting (Figure 2.6) (Weiss et al., 1993). The ignimbrites examined in this study are being investigated in a broader study, using paleomagnetic methods, to understand the history of deformation associated with the development of a transfer system at the southern end of the Walker Lane Belt in the western Great Basin that was active from the mid-Miocene to the mid-Pliocene. The transfer system is bounded on the west side by the Furnace Creek fault system and on the eastern side by the southern Walker Lane fault system. During the mid-Miocene, major caldera forming eruptions resulted in the southwest Nevada volcanic field (SWNVF) (Sawyer et al. 1994). Much of the area studied is covered by ignimbrites that originated from the Timber Mountain Caldera complex, active from ca. 14 to 11.5 Ma (Figure 2.7) (Sawyer et al. 1994). The Neogene sequence of volcanic rocks in the GMSR area rests in either fault-contact or depositional contact on pre-Cenozoic rocks, mainly

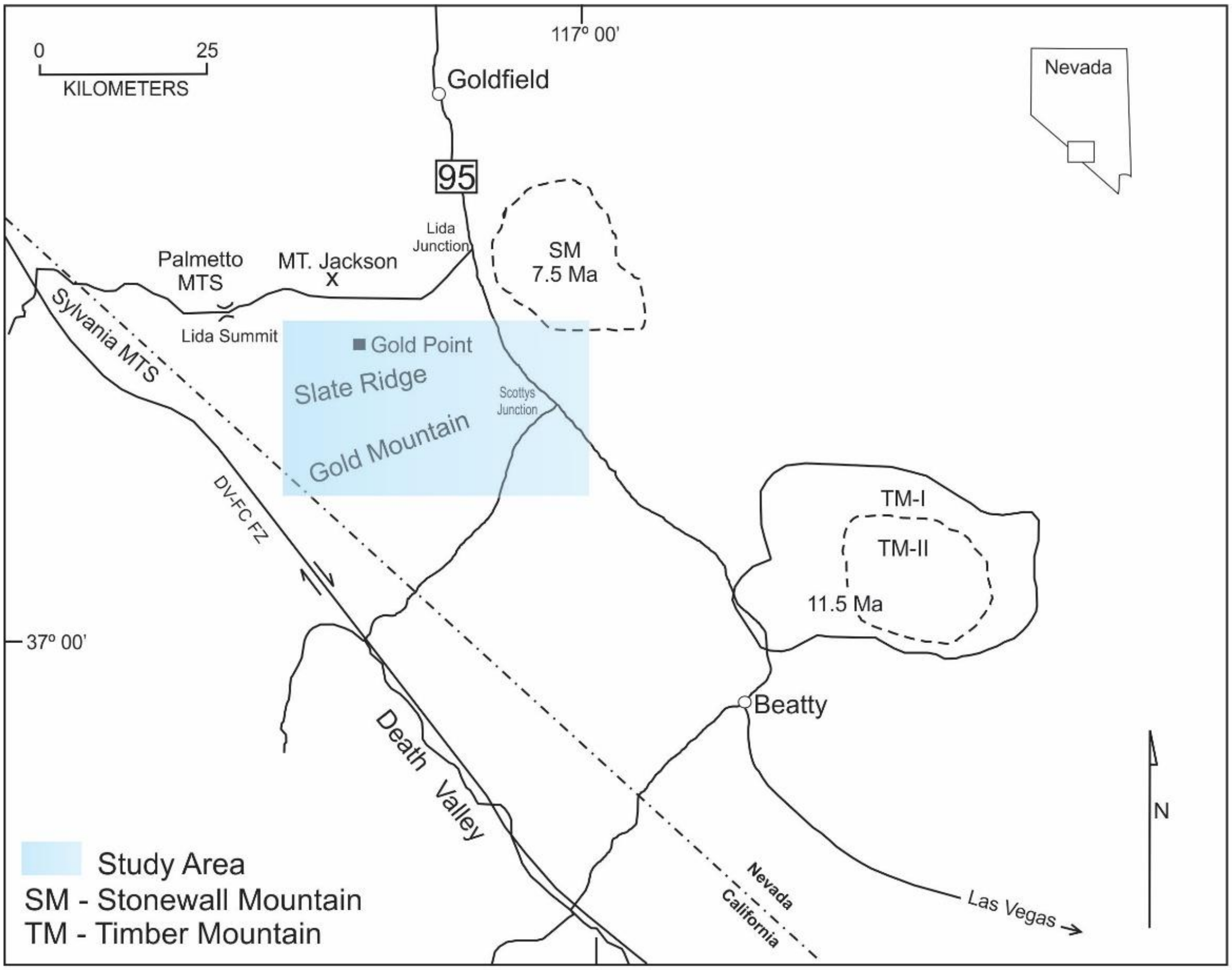

Figure 2.5. Simplified map showing the location of Gold Point/Slate Ridge area relative to neighboring cities.

Cambrian and Precambrian metasedimentary rocks and the Jurassic age Sylvania pluton. The GMSR area, northwest of the SWNVF, exposes numerous east-west trending faults that were active prior to 7.5 Ma (Weiss et al., 1993).

The Neogene sequence of volcanic rocks includes numerous ash-flow tuffs and intercalated conglomerate and fanglomerates deposits (Weiss et al., 1993). The stratigraphically oldest ignimbrite is the Tuff of Mount Dunfee (~16.8 Ma), which is overlain by at least eight additional ash-flow tuff sheets (Figure 2.6). The stratigraphically youngest, and least deformed, ignimbrite is the Stonewall Flat Tuff (~7.6 Ma) (Weiss et al., 1993), which consists of two members. The most well-exposed and voluminous ignimbrites are part of the Timber Mountain Tuff group, which include the Rainier Mesa (~11.6 Ma) of reverse polarity and the Ammonia Tanks members (~11.4 Ma) of normal polarity (Orkild 1965 and Bath 1968).

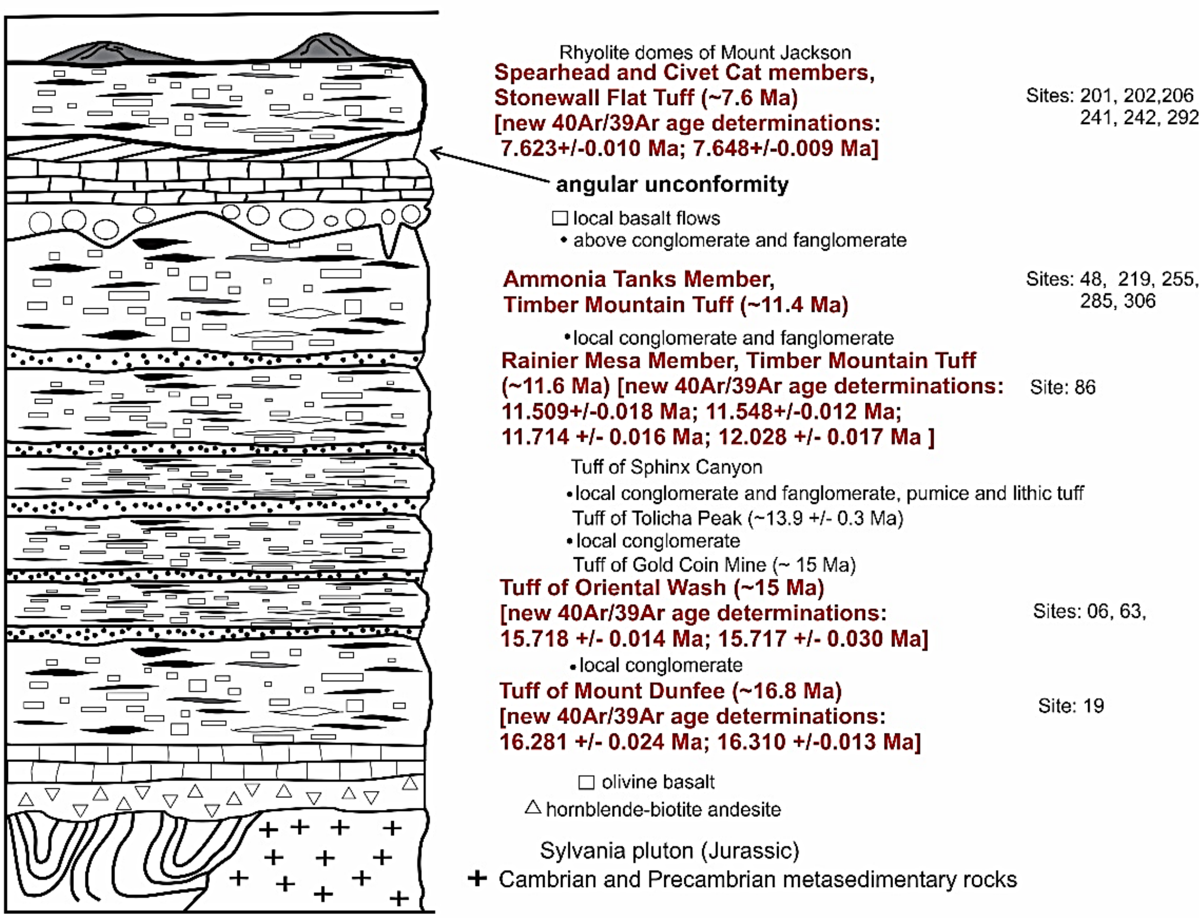

Figure 2.6. Summary of Neogene stratigraphy and depositional relations of the Gold Mountain-Slate Ridge Area (Prepared by J.W. Geissman, 2013, personal communication)

The Tuff of Mount Dunfee is a crystal rich ignimbrite sheet with abundant biotite and is exposed in the northern area of Slate Ridge (Weiss et al., 1993). The Tuff of Mount Dunfee is overlain by the tuff of Oriental Wash, the tuff of Gold Coin Mine, the tuff of Tolicha Peak, and the tuff of Sphinx Canyon, all of which are not well exposed in this general area and their vent sources are poorly known (Weiss et al., 1993). The two principal ignimbrites of the Timber Mountain Tuff, the Rainier Mesa and Ammonia Tanks members are well dated and are sourced from the Timber Mountain Caldera complex (Sawyer et al, 1990 &1994; Worthington, 1992). Both members contain abundant crystals of quartz, sanidine and plagioclase. The Ammonia Tanks Member is distinguished by the presence of sphene and is of normal magnetic polarity, and Rainier Mesa is of reverse polarity (Bath. 1968; Byers et al. 1968; Weiss et al., 1993). Both the Civit Cat and Spearhead members of the Stonewall Flat Tuff was erupted from the Stonewall Mountain volcanic center and is characterized by sanidine crystals that are elongate and tabular, and platy pumice fragments (Nobel et al. 1984; Weiss et al., 1993).

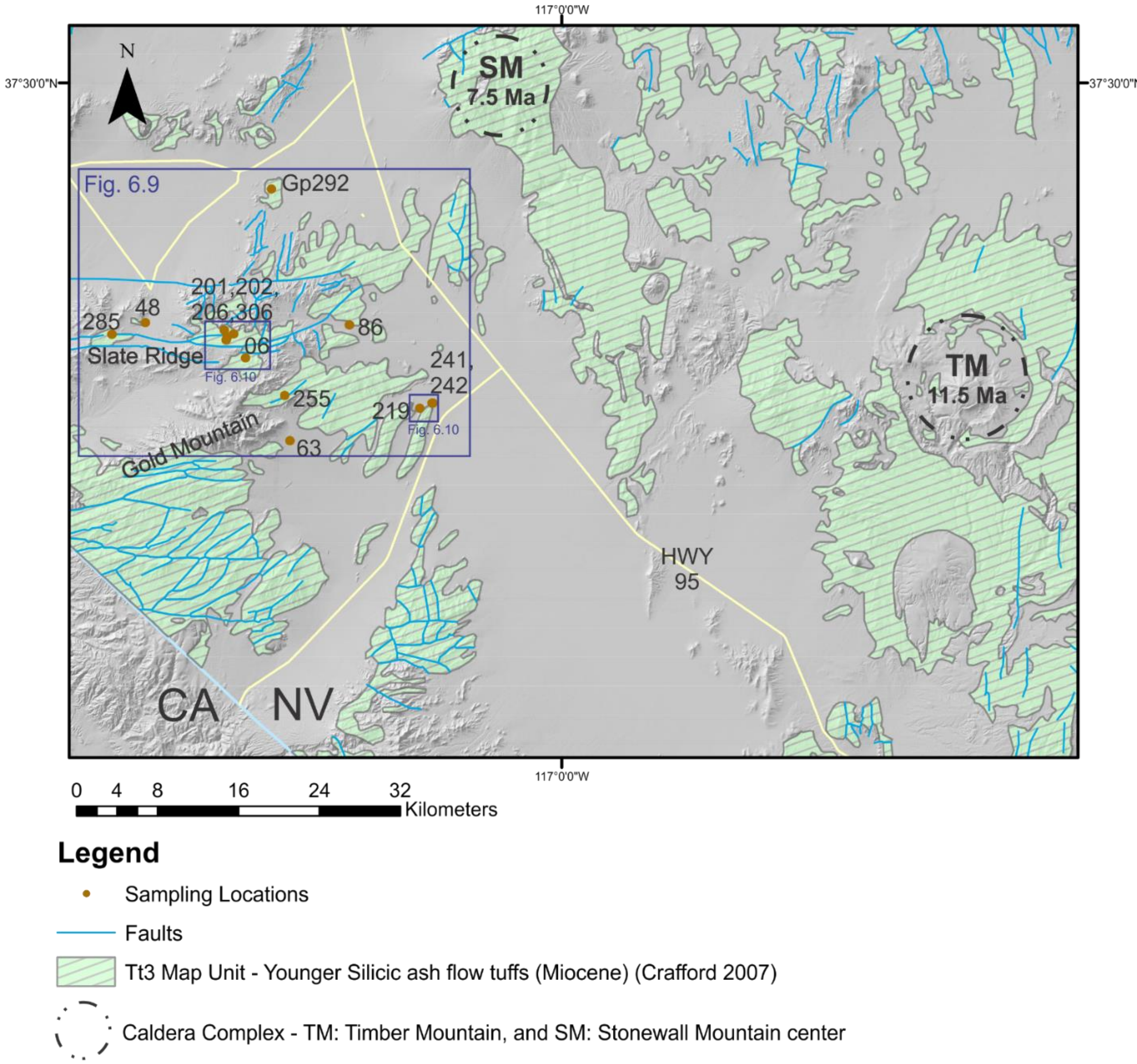

Figure 2.7. Map of Gold Mountain/Slate Ridge (GMSR) area relative to Timber Mountain (TM), Stonewall Mountain (SM), and sampling locations used in this study.

2.3 Pyroclastic Density Currents

Ignimbrites are deposited by ground-hugging pyroclastic density currents (PDCs), dense gravity currents that are mixtures of pyroclastic particles and gas (Sulpizio et al., 2014). The process of PDC emplacement has been well documented by many workers over the last few decades, albeit nomenclature and processes are not always agreed upon (Smith 1960; Sparks 1976, 1979; Wilson and Walker 1982). In the 1970's and 80's, ignimbrites were thought to have originated from an idealized pyroclastic flow that consisted of a inflated fluidized head or cloud, followed by a more dense laminar body or tail and when deposited formed the "standard ignimbrite flow unit" consisting of lithologically different layers (Sparks et al, 1973; Wilson and Walker 1982; Branney and Kokelaar 2002). PCDs have previously been subdivided into pyroclastic flows and surge deposits based on the amount of particle concentration and turbidity of particle transport, but it is now generally accepted that PDCs no longer require such a differentiation due to large variations of particle concentration, varying over space and time, and processes can differ vertically and laterally with regards to PDC transport and deposition (Valentine 1987; Branney and Kokelaar 2002; Burgisser and Bergantz 2002; Ort 2014). Many workers characterize models for recent large-volume PDC's (e.g. those sourced from the Valles Caldera and Toba Caldera) transport and depositional systems with various particle concentrations, volumes and velocities, however these models do not simultaneously share characteristics for both the depositional system and the transport system (flow from the vent) (Ort et al., 2015). Traditionally interpretation of the flow dynamics of depositional systems are made by looking at the distribution of the bedded units and their associated texture and structure features (i.e., orientations of shards or fiamme) (Fisher 1990). However, the most common way to analyze the stratigraphy and flow direction of ignimbrites is determined by either thermal demagnetization or anisotropy of magnetic susceptibility (AMS) (Fisher 1993). AMS is an effective technique to relate the fabrics of ignimbrites to the depositional and transport processes of the PDCs (Baer et al., 1997; Ort et al., 2015).

CHAPTER 3

ANISOTROPY OF MAGNETIC SUSCEPTIBILITY AND MAGNETIC REMANENCE

3.1 Anisotropy of Magnetic Susceptibility

The application and interpretation of anisotropy of magnetic susceptibility (AMS) data have been the focus of numerous investigations since the first observations of AMS in natural samples by Ising (1942), and it has been over sixty years since Graham (1954) fist published a paper on the "Magnetic susceptibility anisotropy measurements of rocks," where AMS was first introduced as a rapid and sensitive petrofabric tool. Prior to AMS being exploited as a tool for petrofabric analysis, orientation distributions of minerals were commonly observed in thin-section inspection and petrofabrics could be interpreted via microscopic means. AMS is a relatively quick and practical way to make petrofabric measurements and detect preferred orientation of minerals in igneous, metamorphic and sedimentary rocks (Hrouda, 1982; Jezek and Hrouda, 2004). Paramagnetic and ferro/ferrimagnetic (s.l.) grains may acquire preferred orientations in rocks (e.g., resulting in a magnetic fabric) through geologic processes such as particle deposition in an aqueous environment, lava or magma flow, and ductile penetrative deformation, therefore making AMS a useful quantitative tool because it is sensitive enough to measure in most rock types (Jezek and Hrouda 2004). Low-field AMS rapidly detects all the contributions from rock-forming minerals (e.g., diamagnetic, paramagnetic, and ferro/ferri-magnetic (s.l.) minerals) that make up the low-field susceptibility of a rock (Jackson and Tauxe 1991; Jackson 1991). AMS is based on the linear relationship between the magnetization and magnetizing field at low fields; that results in a field-independent susceptibility measured in weak fields of average 300 A/m, as measured on Kappabridge susceptibility instruments manufactured by AGICO (Pokorny 2004), which have revolutionized the ease and speed with which measurements are made in the laboratory.

Ignimbrite is defined as the rock or deposit formed from pyroclastic (high temperature) density currents generated during one eruption, where one unit is formed from a single pyroclastic deposit, and ignimbrites may be composed of several pyroclastic deposits (Sparks 1976). Many workers have used AMS as a tool to study volcanic processes (e.g., ignimbrite emplacement), with many studies showing the internally consistent, reproducible character of relatively rapidly obtained data sets (Ellwood 1982, Incontro 1983, Knight 1986, MacDonald and Palmer 1990, Fisher 1993, Cagnoli and Tarling 1997, Le Pennec 1998, Palmer and MacDonald 1999, Ort 2003). The magnetic mineral (i.e., magnetite, maghemite, titanomagnetite) crystals in ignimbrites affect the intensity of the AMS fabric by magnetocrystalline anisotropy (crystallographic direction) or by shape anisotropy (Hargraves et al. 1991).

Table 3.1. AMS Parameters Measured, adopted from Winkler et al. 1997

Parameter	Formula	Reference
Mean Susceptibility	$Km = (K_1 + K_2 + K_3)/3$	Jelinek (1981)
Degree of Anisotropy (P)	$P = (K_1/K_3)$	
Lineation (L)	$L = (K_1/K_2)$	
Foliation (F)	$F = (K_2/K_3)$	
Shape Factor (T)	$T = 2\eta_2 - \eta_1 - \eta_3 / \eta_1 - \eta_3$	
	$T\ (-1 \geq T \geq 1)$	
	$T > 0$ = oblate fabric	
	$T < 0$ = Prolate fabric	
K_1, maximum; K_2, intermediate K_3, minimum susceptibility axes.	$\eta_1 = \ln K_1;\ \eta_2 = \ln K_2;\ \eta_3 = \ln K_3$	η_1, η_3, η_3: the natural logs of the susceptibility axes

Magnetic susceptibility, K, can be defined as M = [K] x H where M is the induced magnetization and H is the magnetic field where M and H are expressed in amperes per meter (A/m). K is dimensionless and expressed as a second rank tensor in SI units. Mass susceptibility is $\chi = K/\rho$ and is expressed in cubic meters per kilogram. AMS data are expressed as triaxial ellipsoids, where the values of the axes are denoted by maximum (K_1), intermediate (K_2), and minimum (K_3) axes respectively, and bulk susceptibility can be calculated by $K = (K_1 + K_2 + K_3)/3$ (Ellwood 1982). The magnetic fabric of a bulk rock is characterized by anisotropy factors that describe the character and magnitude of the AMS, and include the most simple fabrications magnetic lineation, magnetic foliation and anisotropy degree which, are $L = K_1/K_2$, $F = K_2/K_3$, and $P = K_1/K_3$, respectively (Table 3.1) (Jelinek 1981). The shape of the mineral grains also is characterized qualitatively by the shape factor or T, where mineral grain is oblate at +1 or prolate at -1, which generally controls the shape of the AMS susceptibility ellipsoid (Figure 3.1) (Borradaile 2001). In moderately to well-welded ignimbrites, AMS is controlled by the alignment of magnetic minerals, where some workers have reported that the K_1 axis generally is aligned roughly parallel to the direction of flow and lies in the plane that is normal to the direction of major compaction (Ellwood 1982; MacDonald and Palmer 1990; Fisher 1993). This is commonly the case with ignimbrites where these rocks normally exhibit a strong oblate fabric, with the magnetic foliation essentially normal to the flattening direction (Quane and Russell 2005). Other studies have proffered the argument that it is the orientation of the magnetic foliation plane that is more useful as defining the transport direction of PDCs, in that the foliation plane for an outflow facies deposit will be imbricated relative to the paleohorizontal, and that the minimum principal susceptibility axis (K3) will be skew to the vertical and point in the direction of transport (Incoronato et al. 1983; Le Pennec et al. 1998; Geissman et al. 2010).

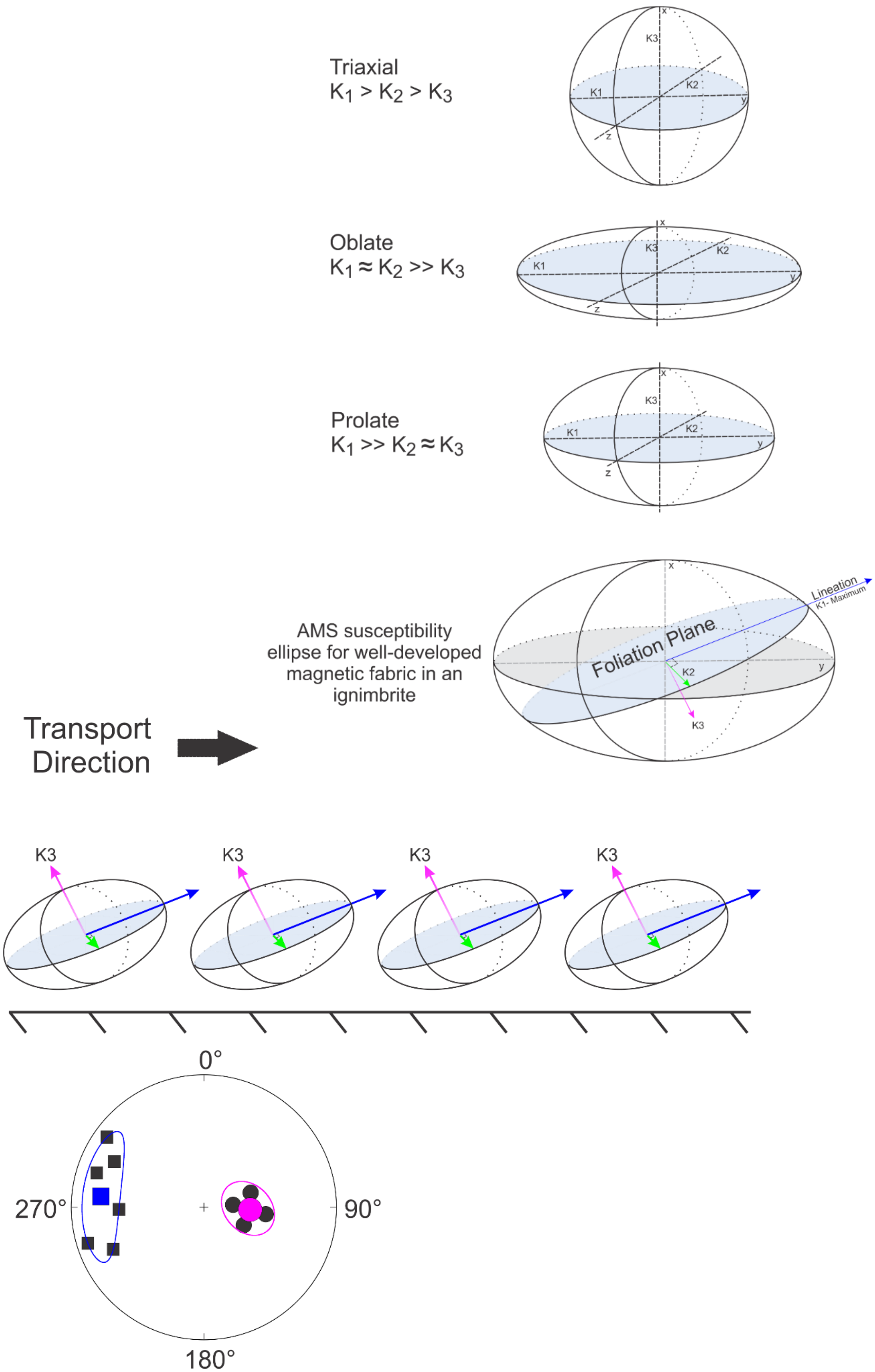
Triaxial
$K_1 > K_2 > K_3$
Oblate
$K_1 \approx K_2 >> K_3$
Prolate
$K_1 >> K_2 \approx K_3$
AMS susceptibility ellipse for well-developed magnetic fabric in an ignimbrite
Foliation Plane
Lineation
K1- Maximum
K1
K2
K3
x
y
z
Transport Direction
0°
90°
180°
270°

Figure 3.1. TOP - AMS susceptibility ellipse defining principal susceptibility axes (K_1, K_2, and K_3 tensors) and typical shapes associated with anisotropic ellipsoids; modified from Winker, et al., 1997; and Wack, 2012.

BOTTOM – Imbrication of a theoretical ignimbrite fabric and associated lower hemisphere stereographic projection of the K1 and K3 axes plotted as black filled squares and circles respectively. Colored shapes represent mean susceptibilities and 95% confidence intervals, modified from (Mason 2011).

3.2 Anisotropy of Magnetic Remanence

The measurement of the anisotropy of magnetic remanence (AMR) differs from that of the AMS, in that only ferro/ferrimagnetic (s.l.) minerals contribute to the magnetic fabric e.g., (Jackson, 1991), and thus the shape distribution of the magnetic phases may have a strong control on the AMR fabric. AMR studies can involve different types of laboratory induced remanent magnetizations, including TRM (thermal), DRM (detrital), ARM (anhysteretic), IRM (isothermal), or GRM (gryo) which are remanent magnetizations that are artificially imparted in the lab (Jackson 1991; Martin-Hernandez et al. 2004). Similar to AMS, AMR is represented by a magnetic ellipsoid with three principal remanence susceptibility axes. Determining a remanence tensor involves magnetizing a specimen repeatedly, in a set of prescribed orientations. In this study, specimens were magnetized in 15 different independent orientations for anisotropy of ARM measurements (AARM). This processes is inherently longer than measurements of AMS (minutes versus 1 hour for AARM) measurements, however AMR methods are becoming increasingly more useful to aid in interpretation of AMS data when interactions between ferro/ferrimagnetic (s.l.) grains occur or when the dominant magnetic phases are highly elongated particles that contribute to the AMS (Ferre 2002; Potter 2004; Borradaile et al. 2010). Normal AMS/ARM fabrics are denoted by K_1 is parallel to the long axis and K_3 is parallel to the short axis, however inverse fabrics in AMS arise as a result of samples of primarily single domain (SD) magnetite grains that have the K_1 parallel to the short axis and K_3 is parallel to the long axis (Ferre 2002). Rochette et al. (1992, 1999), document non-standard relationships in magnetic fabrics using AMS, particularly inverse and intermediate interactions between the paramagnetic and antiferromagnetic minerals, and (single-domain) SD magnetite or maghemite that have the minimum susceptibility axis, K_3, aligned with the preferred long axis. Experiments in the late 1980's demonstrated that the susceptibility anisotropy is largely particle size dependent, specifically when dealing with strong magnetic minerals, such as elongated magnetite particles when large enough i.e., (MD), align with the K_1 axis. Conversely, when smaller as in (SD) particles, the K_1 susceptibility axis of the grain will be perpendicular to the long axis (Stephenson et al. 1986; Potter 1988). The problem arises when there is a mixing of (MD) and uniaxial (SD) or pseudo-multi domain (PSD) magnetite grains that contribute to the AMS because the (SD) magnetite's maximum susceptibility will align with the short axis, causing a single-domain effect where essentially (SD) particles present in the material can rotate away from the K_1 due to weak perpendicular fields. This "single-domain effect," is the very mechanism that introduces the need for AMR studies on magnetite/maghemite-bearing rocks such as ignimbrites, which may experience a component of inverse or intermediate AMS (Figure 3.2) (Jackson 1991; Potter 1988, Borradaile and Jackson 2010). Alternatively with AMR, the ellipsoid should resemble particle shape for both (SD) and (MD) grains (Stephenson et al. 1986; Borradaile and Jackson 2010). Additionally, comparisons of AMR methods to AMS offer additional information regarding domain state and particle size (Potter 2004). In this paper, AMS measurements are compared to two AMR methods of anisotropy, AARM and AIRM.

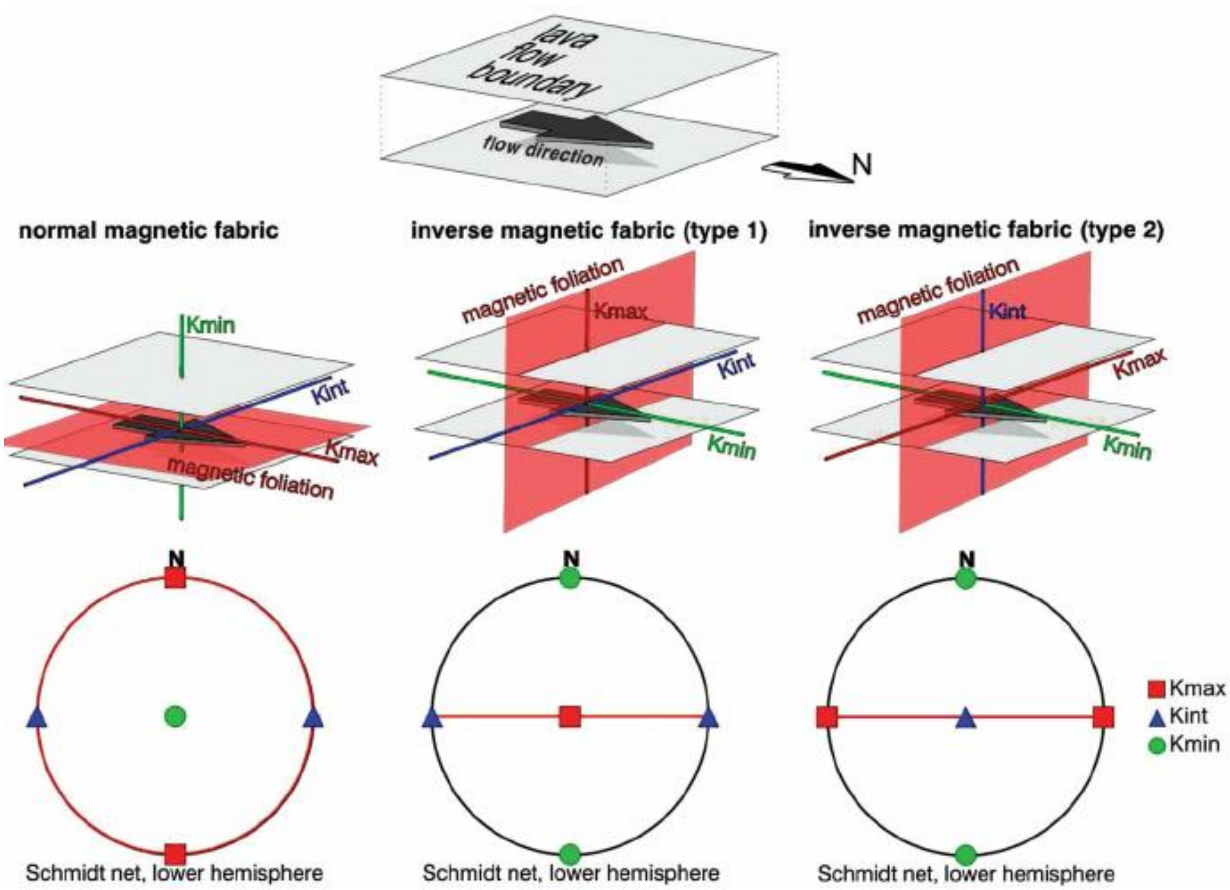

Figure 3.2. Normal and inverse magnetic fabrics with respect to the flow direction

CHAPTER 4

PETROGRAPHY

4.1 Petrography of the Tshirege Member of the Bandelier Tuff

Other authors have published extensive sets of chemical and petrographic information of the Tshirege member of the Bandelier tuff (Warren et al., 2005 and 2007). The Bandelier Tuff contains abundant quartz and sanidine crystals and sparse mafic minerals in a fine-grained, welded ground mass (Gardner 1986). There are significant differences in the petrology of welded tuffs that distinguish the individual cooling units within the Bandelier (Goff et al., 2014). The lower Tshirege Member is only distinguishable from the Otowi Member by a significantly higher lithic content (Warren 2007). The upper Tshirege is described as Qbt4 containing small enclaves of quenched, vesicular, slightly porphyritic andesite magma consisting of plagioclase, orthopyroxene, clinopyroxene, magnetite, ilmenite, apatite, zircon and glass with very rare exceptions of hornblende (Figure 4.1c) (Goff and Warren 2010, Goff et al., 2014). In Qbt4, Qbt5l and Qbt5u there is abundant anorthoclase present that is blocky in form and grows around a core of plagioclase (Goff et al., 2014). In units Qbt3t to Qbt4l nearly all the feldspar is Na-sanidine, with minor anorthoclase or plagioclase and then a big shift from Qbt4u where there are approximately equal amounts of Na-sanidine and anorthoclase and substantial plagioclase (Goff et al., 2014). Polished thin sections were made for a sample from each site from the Bandelier Tuff. The primary Fe-oxide constituent visible on the polished sections are magnetite. The magnetite grains vary in size from very small <50 microns (Figure 4.1c & Figure 4.2g) to very large > 200 microns (Figure 4.1d,f and h), however they represent only about 1% by area (modal percentage) of any polished section.

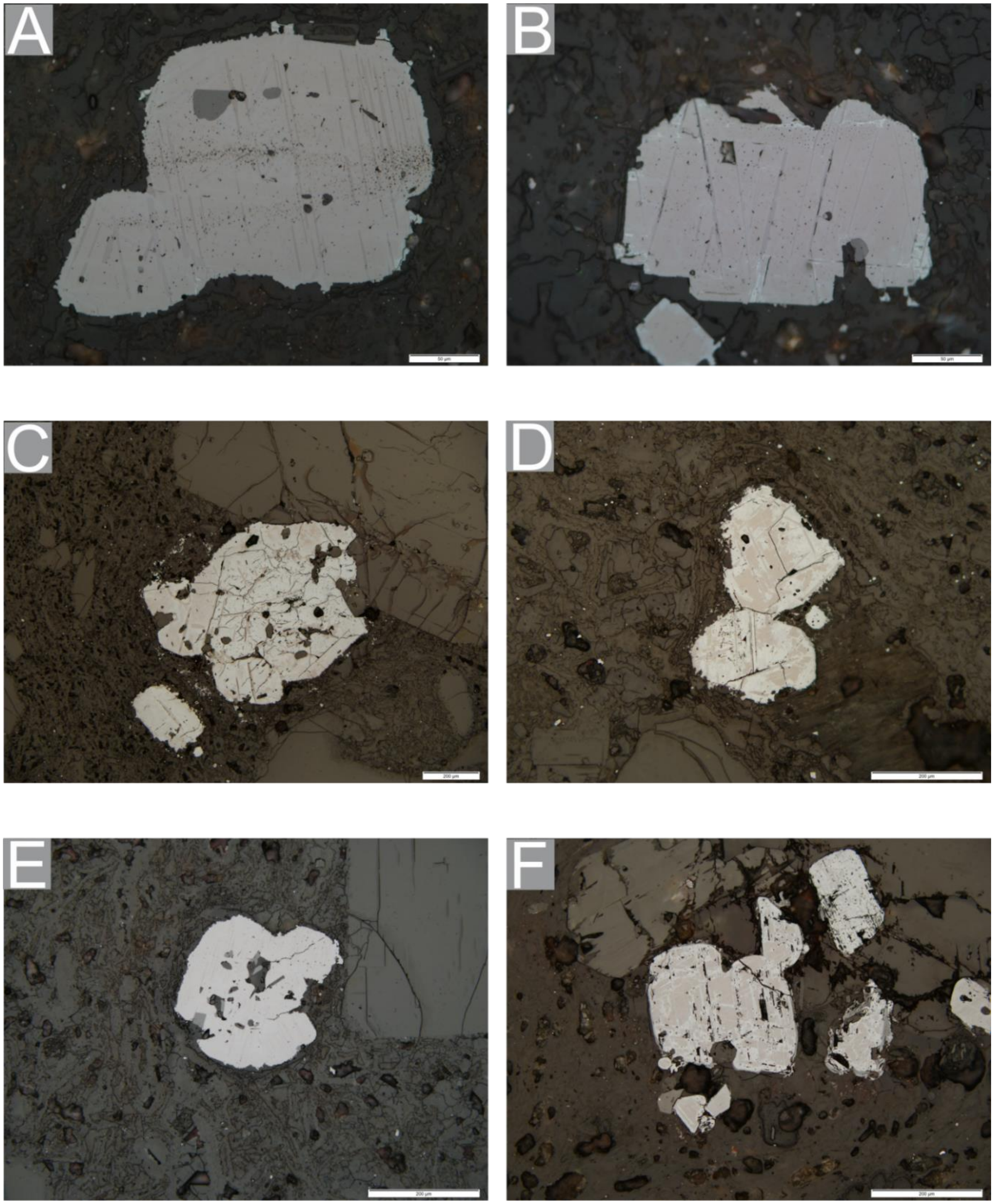

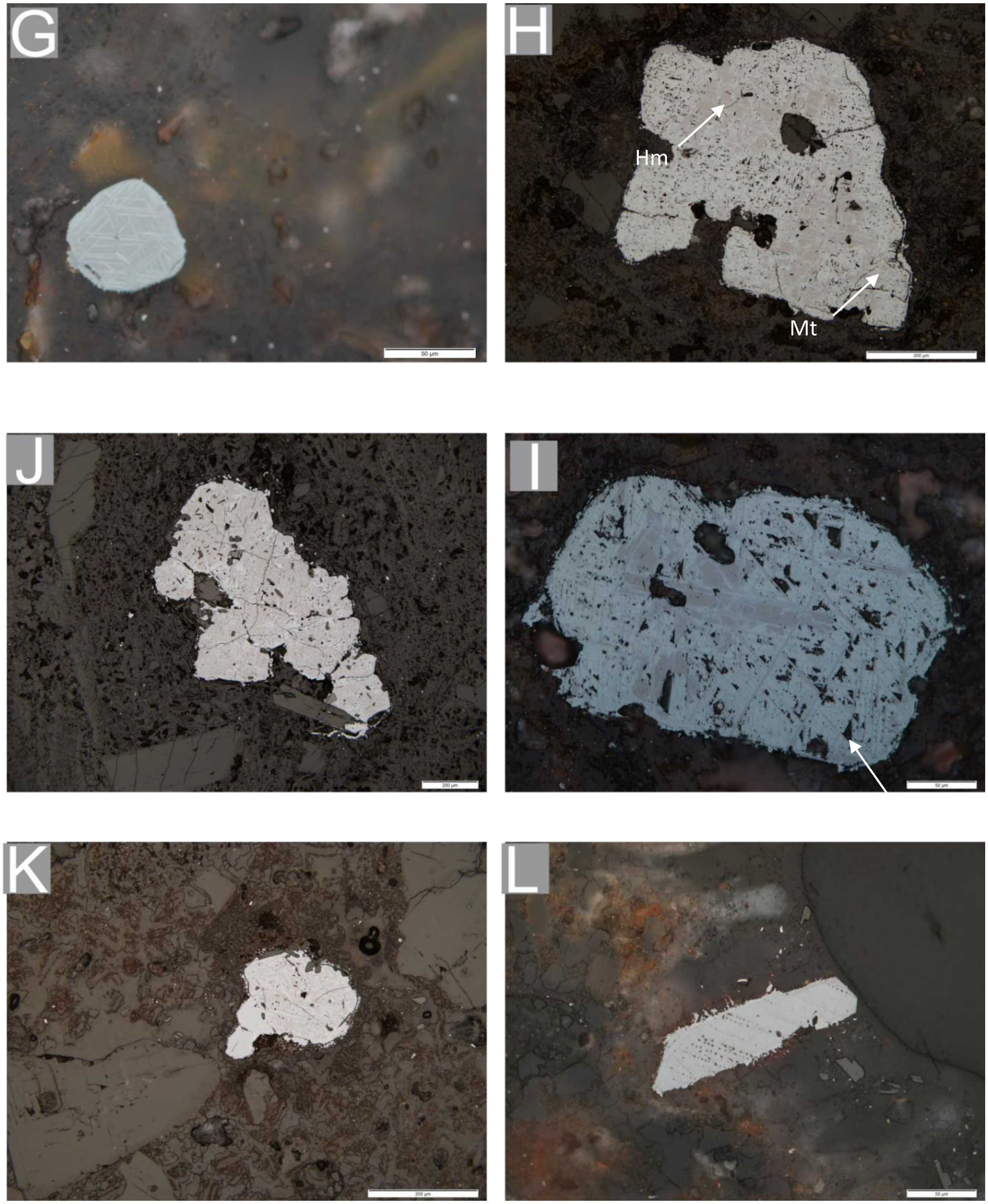

Figure 4.1. Polished thin sections of representative Bandelier tuff photomicrographs on individual grains: Mt: Magnetite; Hm: Hematite; Ilm: Ilmenite

CHAPTER 5

METHODS

Samples from well-exposed, coherent sites in ignimbrites from the Jemez Mountains and west-central Nevada were collected using a portable drill with a diamond tipped non-magnetic core bit. All sites are well characterized in terms of orientation of compaction (eutaxitic) fabrics. At each sampling site in the Jemez Mountains, some 10 to 31 (average of 18) independently oriented core samples were collected from a total of distinct 21 sites established at eight localities during Fall, 2013. In the Gold Point area, sites for this study were selected from a comprehensive collection involving over 275 sites, each of which included same 8 to 20 (average of 12) core samples collected during the summers of 2011 and 2012. Sample orientation employed an integrated Brunton and sun compass orientation device. Samples were cut into ~2.54 x 2.23 cm specimens using a non-magnetic dual-bladed saw at the University of Texas at Dallas. AMS was measured on all specimens from all 21 Bandelier Tuff sites. For the Gold Point area ignimbrites, a total of 16 sites of the sites from the more comprehensive collection were investigated for of AMS, AARM, and AIRM.

5.1 AMS Methods

The AMS of all specimens were measured using either an AGICO Kappabridge KLY-3S susceptibility unit or an AGICO MFK-1A susceptibility unit. The AMS data provide a susceptibility tensor and bulk susceptibility for each specimen analyzed. Anisoft 4.2, an AGICO Inc. product software (AGICO) is the software used to analyze the AMS data. Specimens were all measured in the X, Y and Z positions and then measured for bulk susceptibility while also in the Z position. AMS measurements were made on all specimens prior to AF demagnetization of Natural Remanent magnetization (NRM) or preparation for ARM and IRM experiments.

5.2 AARM Methods

Specimens for anisotropy of anhysteretic remanent magnetization (AARM) measurements were first progressively AF demagnetized using an ASC D-2000 AF demagnetization unit or the 2G Enterprise's AF demagnetizer integrated with the pulse-cooled DC SQUID Superconducting Rock Magnetometer manufactured by 2G Enterprises. ARM was imparted using a DC field of 0.1 mT and a peak alternating field of 100 mT, along 15 independent orientations that result in a susceptibility matrix ($AARM_{max}$>$AARM_{int}$>$AARM_{min}$) ellipsoid that was determined and displayed using AARM software (MatLab software developed by Kit Harper, personal communication, 2013). The ARM was then measured using an AGICO JR-6A Dual Speed Spinner Magnetometer. AMS data from the Bandelier Tuff sites and the Gold Point ignimbrite sites are compared with AARM and AIRM data.

5.3 AIRM Methods

Anisotropy of isothermal remanence magnetization (AIRM) experiments were conducted on seven Gold Point sites (10 specimens per site). Samples used for AIRM experiments were first demagnetized using a stepwise alternating-field (AF) demagnetization with either an ASC D-2000 unit or a 2G Enterprise's demagnetizer pulse-Cooled DC SQUID Superconducting Rock Magnetometer up to peak alternating fields of 100-110 mT. The specimens used were first processed for AARM data and then were subsequently used for AIRM experiments. Gold Point specimens were given an isothermal remanent magnetization (IRM) in a DC field of 125 mT using the ASC IM-10-30 Impulse Magnetizer using the same 15 orientations used for AARM methods and magnetization was measured using an AGICO JR-6A Dual Speed Spinner Magnetometer (Figure 5.1). The peak DC field of 125 mT was chosen based on previous results of IRM acquisition to saturation (SIRM) experiments on these ignimbrites that demonstrated the main magnetic constituent was indeed magnetite or maghemite, consistent with the fields required for saturation (Fitter, 2014).

The same methods were used for AIRM experiments on specimens from sites 5, 11, and 18 in the Bandelier Tuff, however the peak DC field for each specimen was chosen independently based on the 80% saturation yielded from IRM acquisition curves. The Bandelier specimens were given an IRM in a DC field that ranged from 90 to 130 mT.

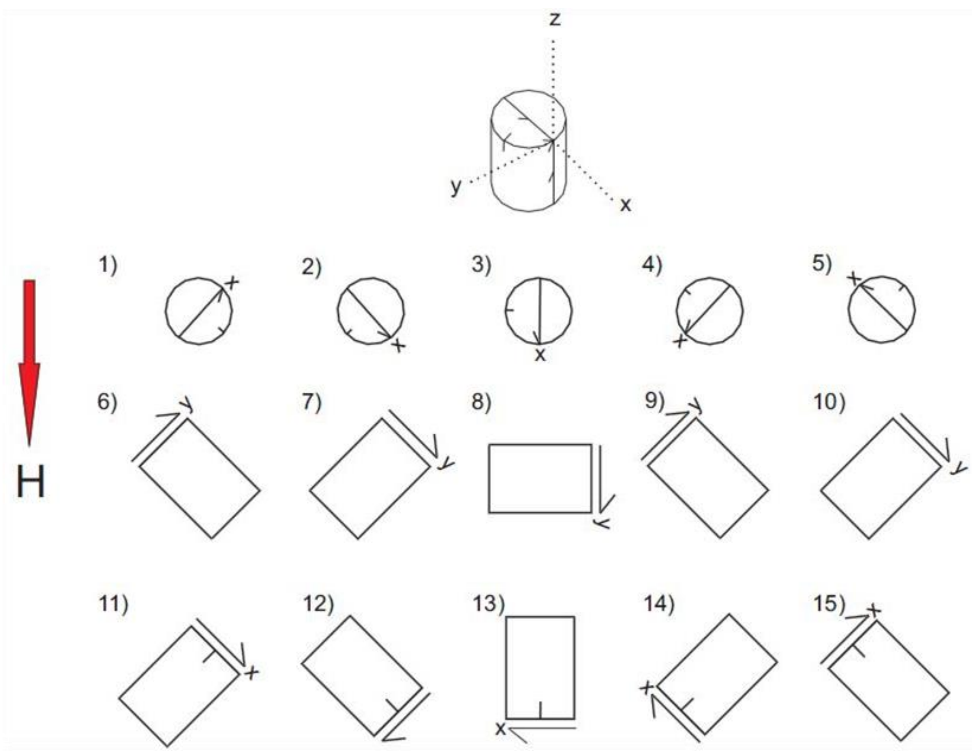

Figure 5.1. The fifteen different measurement orientations used to obtain the AMR Tensor (modified from Tauxe, 1998).

5.4 Susceptibility versus Temperature Measurements

Magnetic susceptibility as a function of temperature was measured on bulk rock samples and magnetic extracts (denoted by MG) from 20 of the 21 Bandelier Tuff sites and from 9 of the 15 Gold Point sites, for identification of the magnetic mineral phases characteristic of each sample. Specimens were first crushed using a porcelain mortar and pestle, and magnetic extracts were separated using a SmCo alloy magnet in a test tube. An AGICO MFK1-A Kappabridge with a CS-4 furnace apparatus assembly, capable of heating to 700° was used for the experiments. Samples were heated from room temperature to between 620 and 660° C, and subsequently cooled back to room temperature. These experiments were conducted in an inert atmosphere (argon). Cureval 8 (M. Chadima, AGICO) was used to display and plot T vs. χ curves

5.5 Hysteresis and FORC Diagram Methods

Room temperature hysteresis curves were obtained for material from each of the 21 Jemez sampling sites using a Princeton Measurements MicroMag 3900 vibrating sample magnetometer (VSM). Small fragments (~3-5 mm) that fit onto the x-axis probe were measured. Hysteresis loops were measured with a maximum applied field set to 500 mT. A total of 59 individual measurements were made with three fragments per site measured, with the exception of sites of 14, 15, and 16.

Twenty-five sets of consecutive FORC distributions where obtained from Bandelier Tuff specimens, using the MicroMag 3900 VSM. Each raw FORC set measured 120 FORCs, the saturating field was set to 500 mT, and an averaging time set to three seconds. The field increment was set to 5.61 mT. Measurements were made on material from the twenty-five specimens of Bandelier Tuff used for hysteresis loops with one fragment per site measured, with the exception of site 5, 11, 18, and 20, with the intent of using these data to relate to the changes in welding and composition among sites. Software FORCinel was used to calculate and display FORC diagrams (Harrison 2008).

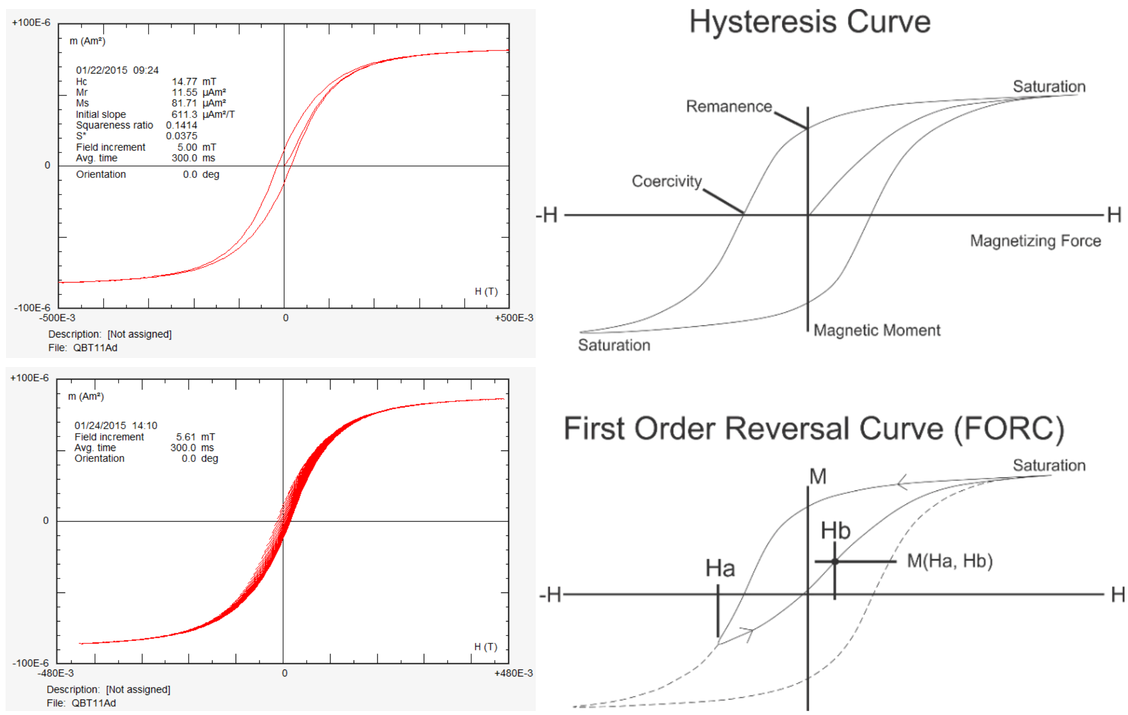

Figure 5.2. Comparisons of hysteresis and first-order reversal curves (FORC). Data on the left were obtained in this study; and figures on the right are adopted from Roberts et al. 2000 and Muxworthy 2007.

CHAPTER 6

RESULTS

6.1 AMS Fabric Information

AMS data were obtained from all 21 sites in the Bandelier Tuff collection (701 specimens) and from the 14 Gold Point sites (477 specimens). In total, data from 16 specimens from the Bandelier Tuff and 5 from the Gold Point collections were discarded from further analysis because they that are clearly inconsistent from overall populations characteristic of each site.

Most sites in the Bandelier Tuff yield very well defined principal susceptibility axes, with the exception of sites 1, 2 and 9, which exhibited a higher, yet still interpretable, degree of scatter. The average mean bulk susceptibility for the total of all Bandelier Tuff sites is 5.46 x 10^{-3} SI volume, with a standard deviation of 2.84 x 10^{-3} (Table 6.1). The degree of anisotropy (P) ranges from 1.011 to 1.031. A Flinn-type plot of L versus F (Figure 6.1) shows the strong dominance by foliation, as expected for moderately to well-welded ignimbrites. The shape factor (T) average values are all greater than zero, and range from 0.318 to 0.745, indicating that the material at all sites is dominated by an oblate fabric (Figure 6.2). The average magnetic lineation (L) value is 1.006 (standard deviation 0.029) and average magnetic foliation (F) value is 1.016 (standard deviation 0.068). The orientation of K_1 susceptibility axes for most of the sites (16 of 21 or 76%) is WNW-WSW with plunges that are consistently to the west, which is consistent with an inferred ENE to ESE transport direction from the source Valles Caldera. Sites 1, 2, 6, 8 and 13 provide data that are exceptions, in that K_1 plunges to the east and southeast.

An alternative approach to inspecting the data involved the imbrication orientation of foliation, i.e., the dispersion and orientation of the K_3 susceptibility axes (Incoronato et al. 1983, MacDonald and Palmer 1990). For all the AMS data collected from the Bandelier Tuff, there is a tight grouping of the steeply inclined K_3 susceptibility axes. For most sites (18 of 21, 86%), the K_3 axes plunge to the ENE-ESE. The exceptions are sites 1, 2, and 13. When comparing the difference between the trend of K_1 and the inferred flow direction based on plunge direction of K_3 axes, 6 of the 21 (sites 2, 5, 6, 8, 10, and 17) sites had orientations that differed by greater than 60 degrees. Only one site (Qbt 2) displayed nearly orthogonal (85.5° apart) K1 and K3 flow directions.

Eleven sites in ignimbrites from the Gold Point area yield data showing well-defined moderate to steeply dipping K_3 axes (>50) with the magnetic foliation plane either dipping between 20 and 30° or nearly sub-horizontal, (< 20°) (Table 6.3 and 6.4). Three of the ignimbrite sites from Gold Point yield data with moderate to nearly horizontal K_3 axes, and the magnetic foliation plane that is moderately dipping (40-60°) (Figure 6.8). All AMS data from the Gold point sites were given proper structural corrections that estimated local tilt based on orientations measured at each outcrop. The average site mean bulk susceptibility is 4.43×10^{-3} SI volume and values range from 1.41×10^{-4} to 9.16×10^{-3}. The degree of anisotropy (P) ranges from 1.010 to 1.052, with a mean of 1.026 (standard deviation 0.012). The Flinn plot for the data from the Gold Point sites (Figure 6.3) defines an oblate fabric and shows that magnetic foliation dominates over lineation. The shape factor (T) is always positive and ranges in values from 0.440 to 0.945, also indicating an oblate fabric (Figure 6.4). Six sites originate from the Timber Mountain Caldera Complex, located E-SE of the sampling area so a transport direction to the W-NW would be expected, however of the six TM sites only two yield inferred flow directions to the west and north. Three of the sites (GP86, GP219, and GP285) show an inferred flow direction to the east and one of the sites (GP255) shows an inferred transport direction to the southwest (Figure 6.7 and 6.9). By comparing the difference K_1 flow sense to the K3 flow direction there were four sites that had a difference of greater than 60° and one site (GP 63) that has nearly orthogonal sense of direction for the K1 and K3 axes (78.9°) (Figure 6.8).

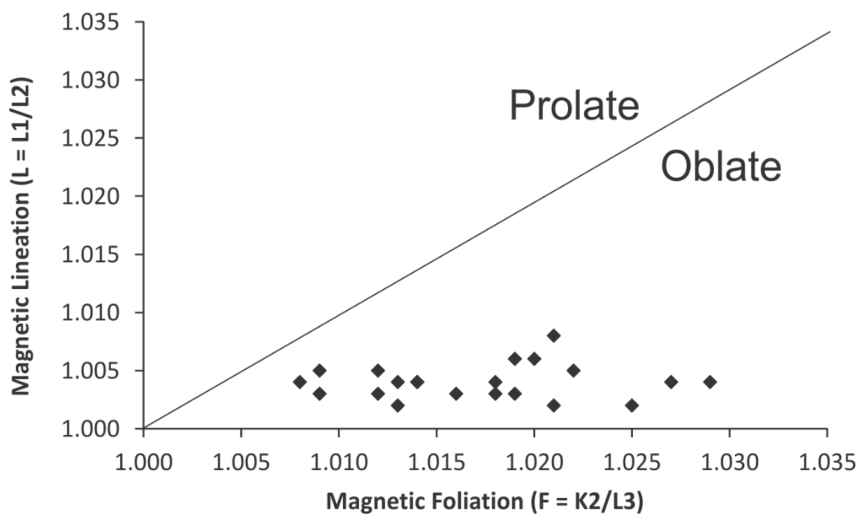

Figure 6.1. Flinn-type plot showing mean magnetic foliation plotted against mean magnetic lineation for all 21 sites in the Bandelier Tuff

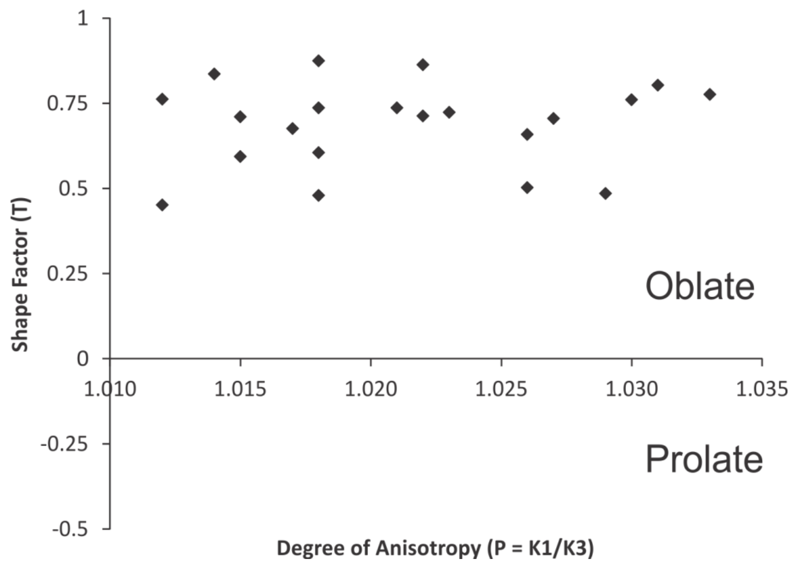

Figure 6.2. Cross Plot of shape factor versus the degree of anisotropy for data from the 21 sites in the Bandelier Tuff.

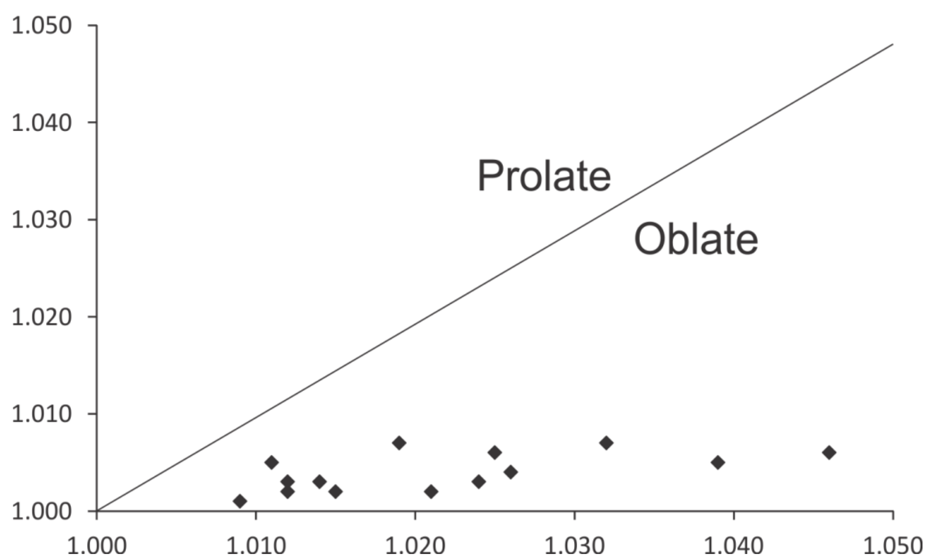

Figure 6.3. Flinn-type plot showing magnetic foliation versus magnetic lineation for the 14 sites in the Gold Point ignimbrites

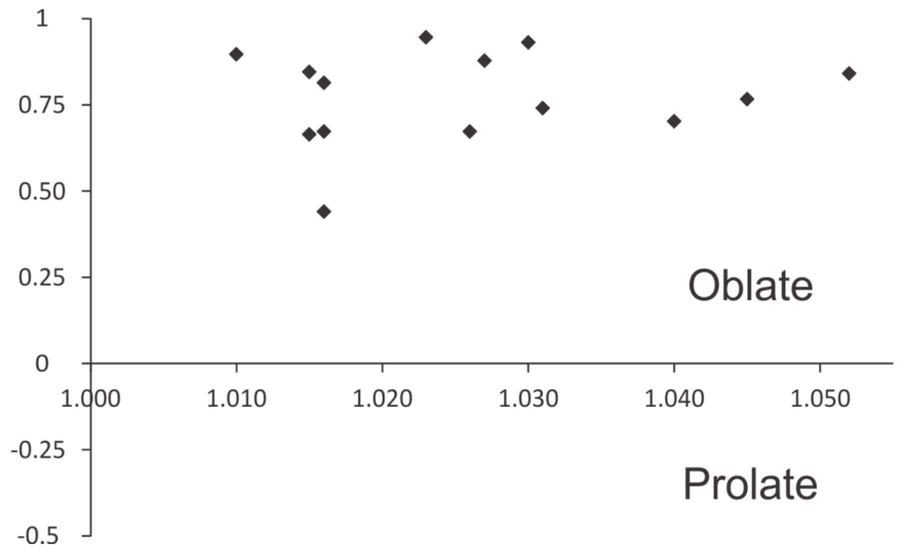

Figure 6.4. Cross Plot of shape factor versus the degree of anisotropy for Gold Point ignimbrites

6.1.1 Bandelier Tuff

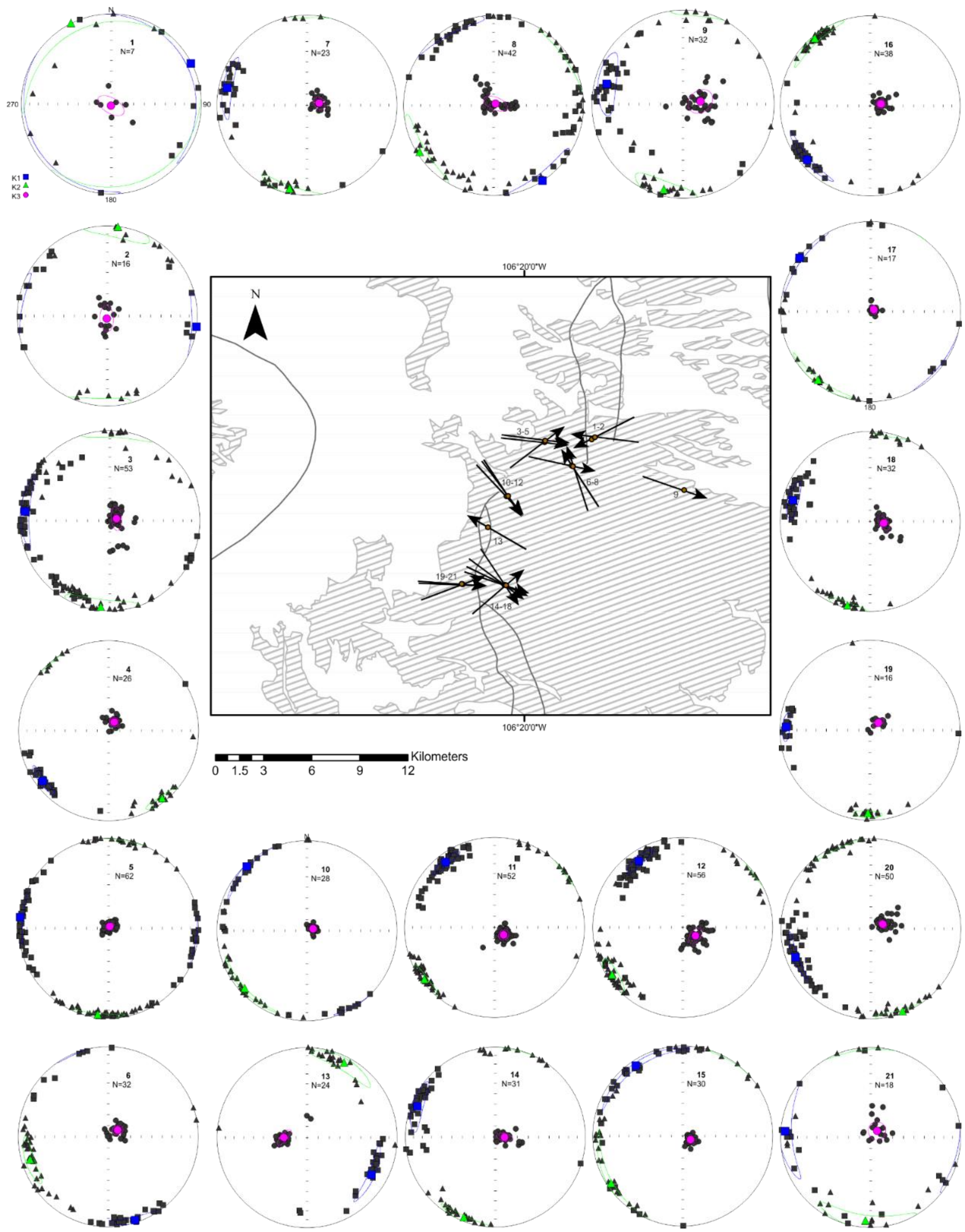

Figure 6.5. AMS ellipsoidal data and plotted arrows on map showing sampling localities representing K_1 azimuthal direction for all sites in Bandelier Tuff, with arrow pointing in the direction of plunge of K_1.

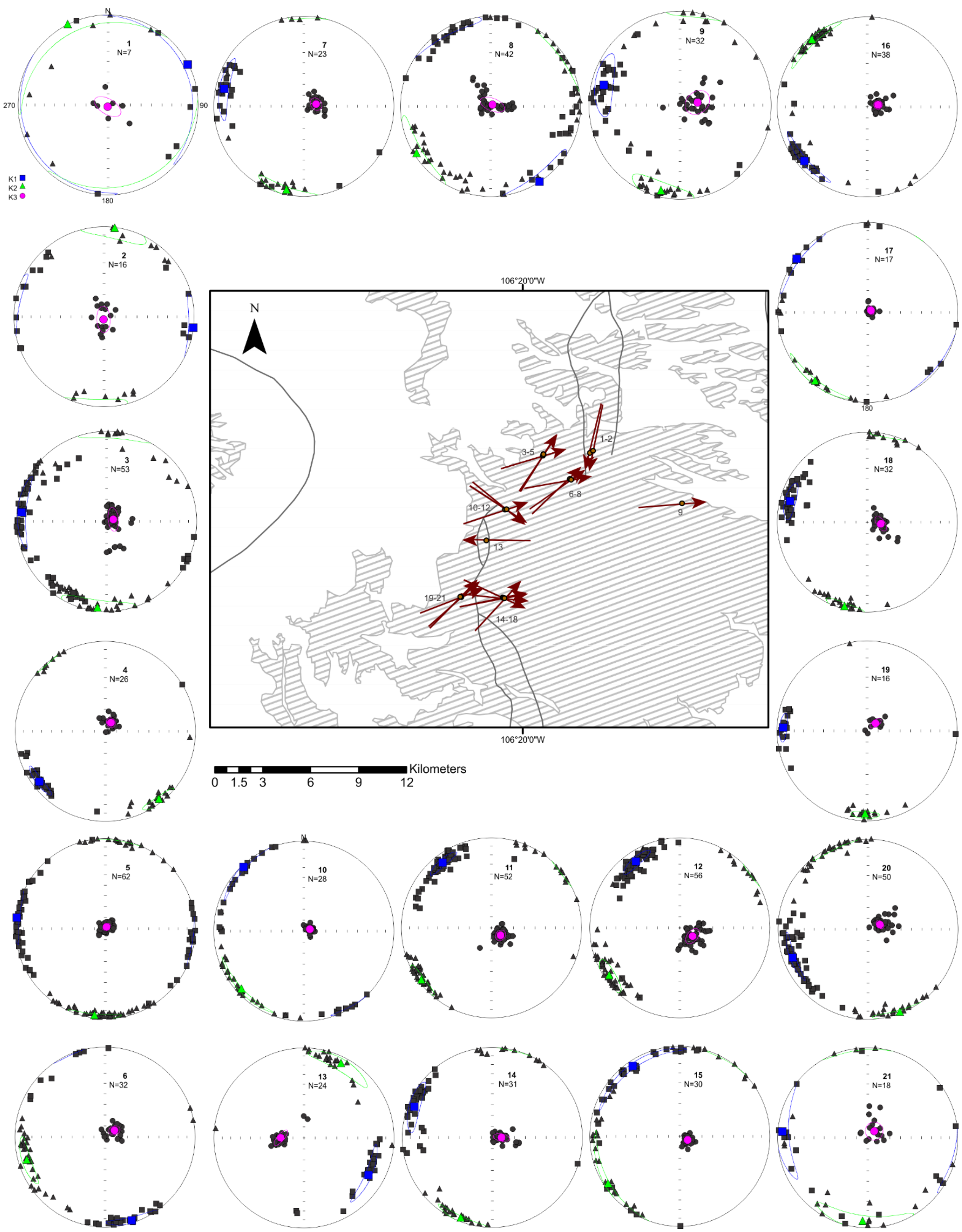

Figure 6.6. AMS ellipsoidal data and plotted arrows on map showing sampling localities representing K_3 azimuthal directions with arrows pointing to the plunge of K_3 for all 21 sites in the Bandelier Tuff.

Table 6.1. Summary of AMS Results for Bandelier Tuffs

Site	n/N	K1	K2	K3	K1 Dec (°)	K1 Inc (°)	K1 Dec E (°)	K1 Inc E (°)	K2 Dec (°)	K2 Inc (°)	K2 Dec E (°)	K2 Inc E (°)	K3 Dec (°)	K3 Inc (°)	K3 Dec E (°)	K3 Inc E (°)
QBT01	7	1.004	1.003	0.993	63.0	1.0	63.2	5.5	333.0	1.2	69.2	10.2	193.7	88.4	13.3	6.8
QBT02	16	1.005	1.002	0.994	97.0	0.2	22.9	5.7	6.9	2.4	22.9	10.7	191.5	87.6	11.9	6.0
QBT03	53	1.010	1.007	0.983	276.2	5.8	24.9	5.1	185.9	2.4	24.9	10.5	73.3	83.7	10.8	4.7
QBT04	26	1.012	1.004	0.984	232.7	8.7	12.3	3.8	142.2	3.2	12.3	4.6	32.3	80.7	4.6	3.9
QBT05	62/65	1.011	1.008	0.981	277.1	0.9	65.1	2.3	187.1	1.8	65.7	3.0	34.1	88.0	52.0	1.5
QBT06	32	1.007	1.003	0.990	162.2	3.1	17.4	3.9	252.7	9.9	17.4	5.2	54.8	79.6	5.3	4.0
QBT07	23	1.006	1.004	0.990	282.3	10.3	22.3	5.5	191.6	4.2	22.3	5.0	79.9	78.9	6.0	4.7
QBT08	42	1.006	1.003	0.991	147.0	0.4	27.4	8.5	237.0	2.3	27.0	7.9	46.1	87.6	11.7	5.7
QBT09	32/36	1.011	1.004	0.985	284.4	14.5	22.4	10.0	192.8	5.9	22.2	10.8	81.1	74.2	11.8	9.3
QBT10	28	1.008	1.005	0.987	316.8	2.4	25.9	2.4	226.6	5.2	25.8	2.1	71.6	84.3	3.2	2.1
QBT11	52/54	1.006	1.004	0.991	322.4	10.1	11.0	4.7	231.9	3.0	11.4	5.1	125.5	79.4	6.0	4.7
QBT12	56	1.008	1.005	0.987	326.5	12.6	12.8	4.6	235.3	5.2	12.6	7.5	123.2	76.3	7.7	4.8
QBT13	24	1.008	1.005	0.988	120.0	18.5	23.6	3.6	26.7	9.6	24.0	7.0	270.6	69.0	8.8	3.0
QBT14	31/35	1.012	1.008	0.980	291.5	7.7	18.2	6.6	201.1	2.9	18.0	3.5	90.6	81.7	7.4	3.3
QBT15	30	1.006	1.005	0.989	326.3	6.6	38.4	3.1	235.8	4.0	38.4	3.0	114.9	82.2	3.3	2.9
QBT16	38	1.010	1.005	0.985	229.4	8.6	23.1	3.5	320.1	4.9	23.1	3.7	79.2	80.1	4.0	3.7
QBT17	17/18	1.008	1.006	0.986	307.1	1.1	25.0	3.8	217.0	3.2	25.0	3.2	56.3	86.6	4.3	2.6
QBT18	32/34	1.006	1.003	0.991	285.3	12.2	13.4	6.3	194.9	1.8	13.4	5.6	96.8	77.6	7.6	3.6
QBT19	16	1.007	1.004	0.989	272.2	7.4	9.9	4.4	181.3	7.0	9.6	4.2	48.5	79.8	5.8	2.9
QBT20	50	1.010	1.006	0.984	249.3	11.5	18.2	3.0	159.3	0.1	18.2	4.0	68.7	78.5	4.3	2.8
QBT21	18	1.004	1.003	0.993	274.1	5.4	34.7	7.4	183.5	6.3	34.6	8.1	44.6	81.7	8.2	7.9

n/N: Ratio of the number of accepted specimens/Total specimens measured for each site.
K_1, K_2, K_3: Normalized values of maximum, intermediate and minimum susceptibility axes
K_1 Dec, K_2 Dec, K_3 Dec: Declination of principal susceptibility axes
K_1 Inc, K_2 Inc, K_3 Inc: Inclination of principal susceptibility axes
E: 95% confidence limits of susceptibility axes

Table 6.2. Summary of AMS Susceptibility Parameters

Site	Unit	Easting	Northing	Km	L	F	P	Pj	T	U	ρ (g/c^3)	σ	F = K2/K3	L = K1/K2	P =K1/K3
QBT01	Qbt4	0383082	3973299	4.14E-03	1.005	1.009	1.014	1.012	0.836	0.835	1.333	0.02	1.010	1.001	1.011
QBT02	Qbt4	0383249	3973405	2.48E-03	1.004	1.008	1.012	1.012	0.451	0.449	1.511	0.06	1.008	1.003	1.011
QBT03	Qbt3t	0380698	3973189	8.00E-03	1.002	1.025	1.03	1.03	0.76	0.757	1.865	0.06	1.024	1.003	1.027
QBT04	Qbt3	0380726	3973267	7.54E-03	1.008	1.021	1.029	1.029	0.485	0.48	1.466	0.06	1.020	1.008	1.028
QBT05	Qbt3t	0380728	3973268	9.45E-03	1.004	1.027	1.031	1.034	0.803	0.683	1.822	0.04	1.028	1.003	1.031
QBT06	Qbt3	0382054	3971994	7.83E-03	1.005	1.012	1.018	1.018	0.479	0.475	1.910	0.02	1.013	1.004	1.017
QBT07	Qbt3t	0382054	3971994	4.15E-03	1.004	1.014	1.018	1.018	0.736	0.734	1.716	0.04	1.014	1.002	1.016
QBT08	Qbt3t	0382117	3971956	7.31E-03	1.004	1.013	1.017	1.016	0.675	0.673	1.866	0.03	1.012	1.003	1.015
QBT09	Qbt2	0387729	3970692	4.65E-04	1.006	1.019	1.026	1.027	0.502	0.498	1.438	0.06	1.019	1.007	1.026
QBT10	Qbt3t	0378739	3970494	7.68E-03	1.004	1.018	1.023	1.023	0.723	0.721	2.110	0.02	1.018	1.003	1.021
QBT11	Qbt3t	0378816	3970505	4.83E-03	1.002	1.013	1.015	1.016	0.71	0.708	1.713	0.16	1.013	1.002	1.015
QBT12	Qbt3t	0378816	3970505	5.72E-03	1.003	1.019	1.022	1.023	0.712	0.71	1.662	0.06	1.018	1.003	1.021
QBT13	Qbt3t	0377776	3968947	9.16E-03	1.003	1.018	1.021	1.022	0.736	0.734	2.195	0.02	1.017	1.003	1.020
QBT14	Qbt3	0378562	3966047	6.73E-03	1.004	1.029	1.033	1.036	0.776	0.773	1.651	0.14	1.029	1.004	1.033
QBT15	Qbt3	0378620	3966028	2.86E-03	1.003	1.016	1.018	1.02	0.874	0.873	1.675	0.02	1.016	1.001	1.017
QBT16	Qbt3	0378626	3966029	2.02E-03	1.006	1.02	1.026	1.027	0.658	0.665	1.882	0.02	1.020	1.005	1.025
QBT17	Qbt3	0378651	3966015	4.71E-03	1.002	1.021	1.022	1.025	0.863	0.862	1.419	0.04	1.020	1.002	1.022
QBT18	Qbt3	0378651	3966015	3.23E-03	1.003	1.012	1.015	1.016	0.593	0.591	1.558	0.02	1.012	1.003	1.015
QBT19	Qbt3	0376459	3966093	7.48E-03	1.004	1.014	1.018	1.019	0.605	0.602	2.273	0.02	1.015	1.003	1.018
QBT20	Qbt3t	0376429	3966113	7.79E-03	1.005	1.022	1.027	1.028	0.705	0.701	1.777	0.26	1.022	1.004	1.026
QBT21	Qbt3t	0376413	396120	1.43E-03	1.003	1.009	1.012	1.012	0.762	0.761	1.196	0.08	1.010	1.001	1.011

Abbreviations for AMS Parameters

Km: Average bulk susceptibility; L: magnetic lineation; F: magnetic foliation; P: degree of anisotropy; Pj: percent anisotropy; T: shape factor that reflects the shape of the susceptibility ellipsoid; U: difference shape factor

6.1.2 Tuffs of Gold Point

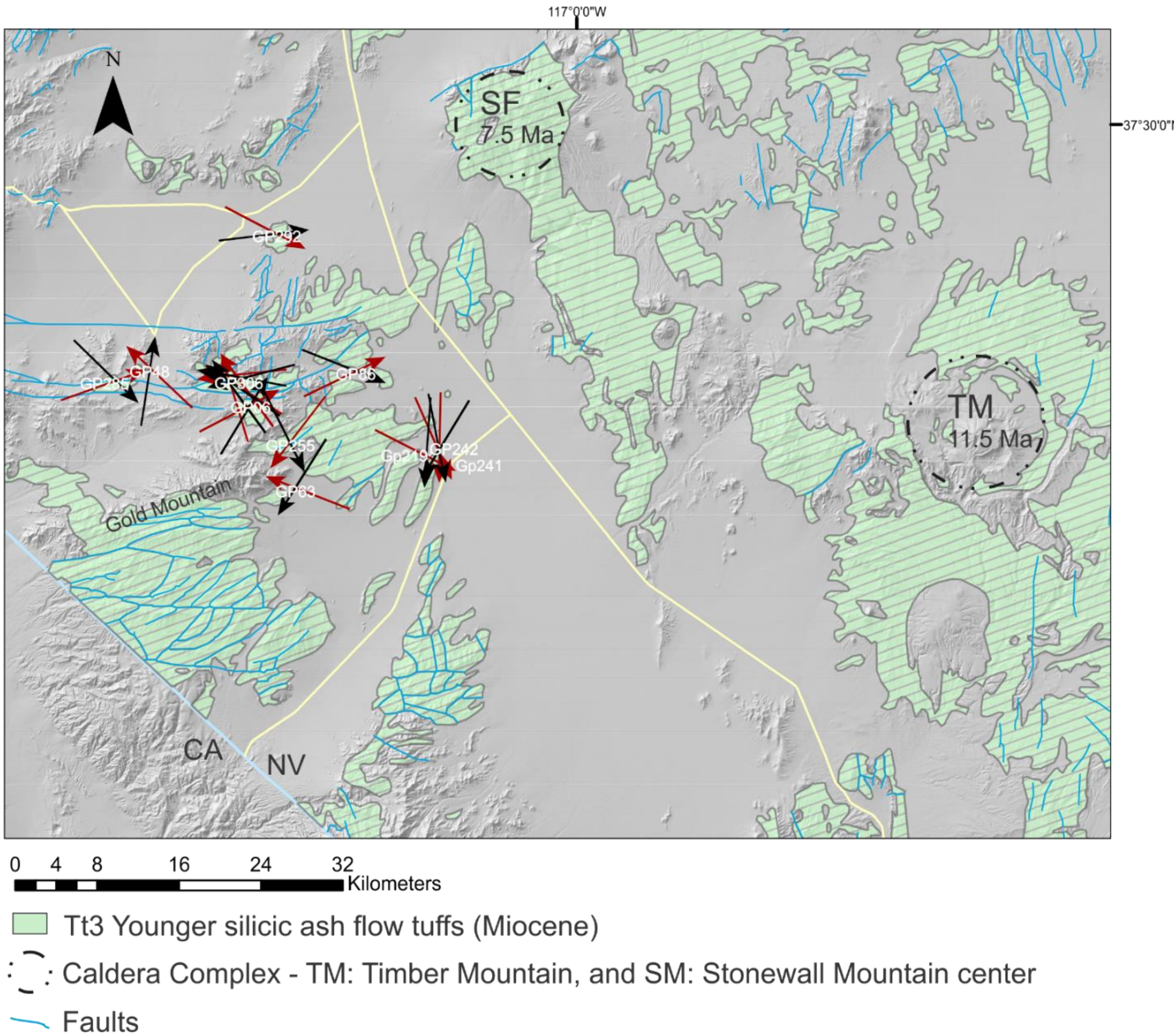

Figure 6.7. AMS results for Gold Point Area ignimbrites, black arrows represent inferred K_1 transport direction (plunge direction) and red arrows represent K_3 inferred transport direction; Map unit Tt3 from Stewart and Carlson, 1978 and Crafford, 2007.

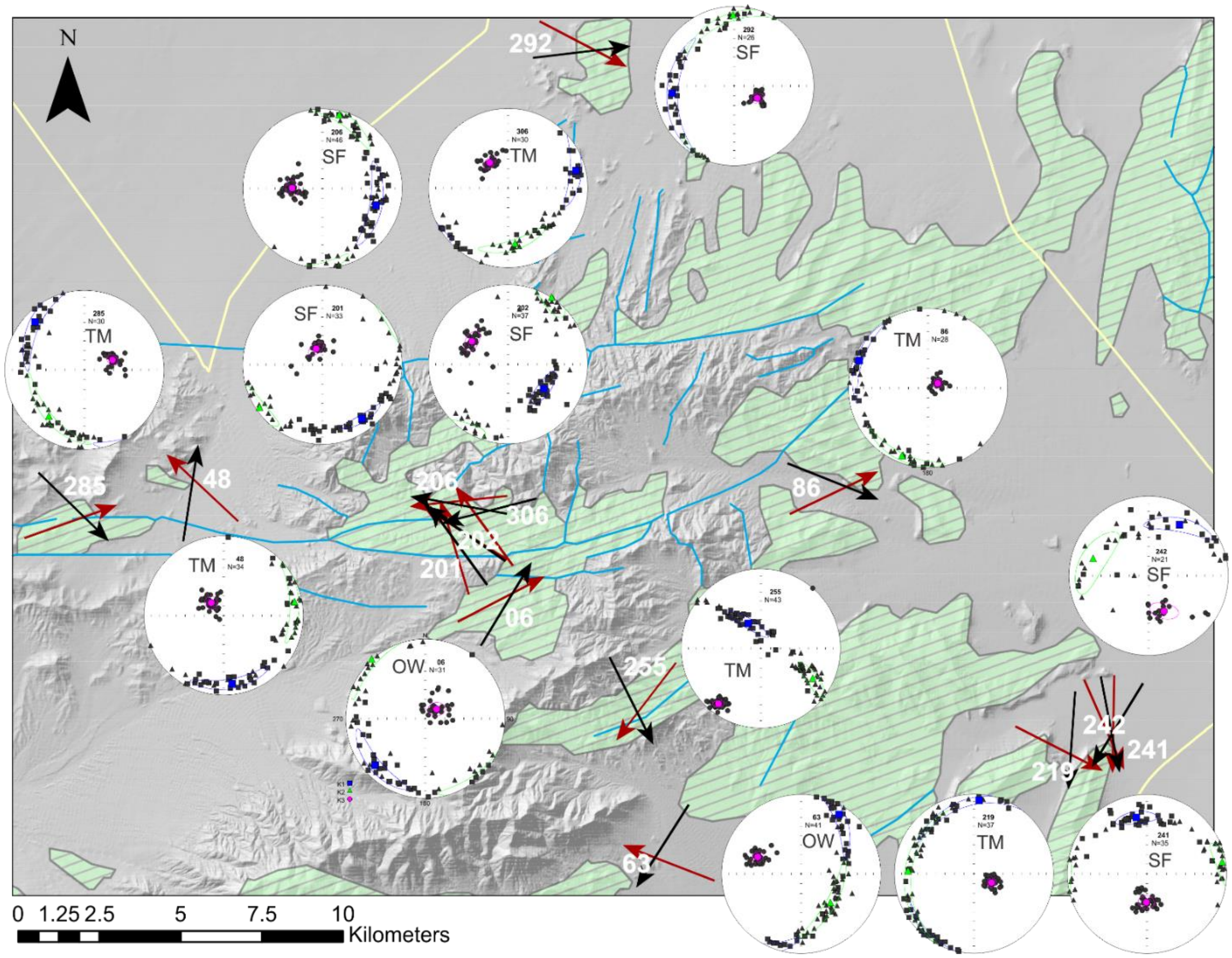

Figure 6.8. Enlarged map showing AMS results for Gold Point area ignimbrites; SF – Tuff of Stonewall Flat, TM – Timber Mountain Tuff, OW – Tuff of Oriental Wash; Red Arrow indicating inferred K_3 flow direction and black arrow direction of plunge of K_1.

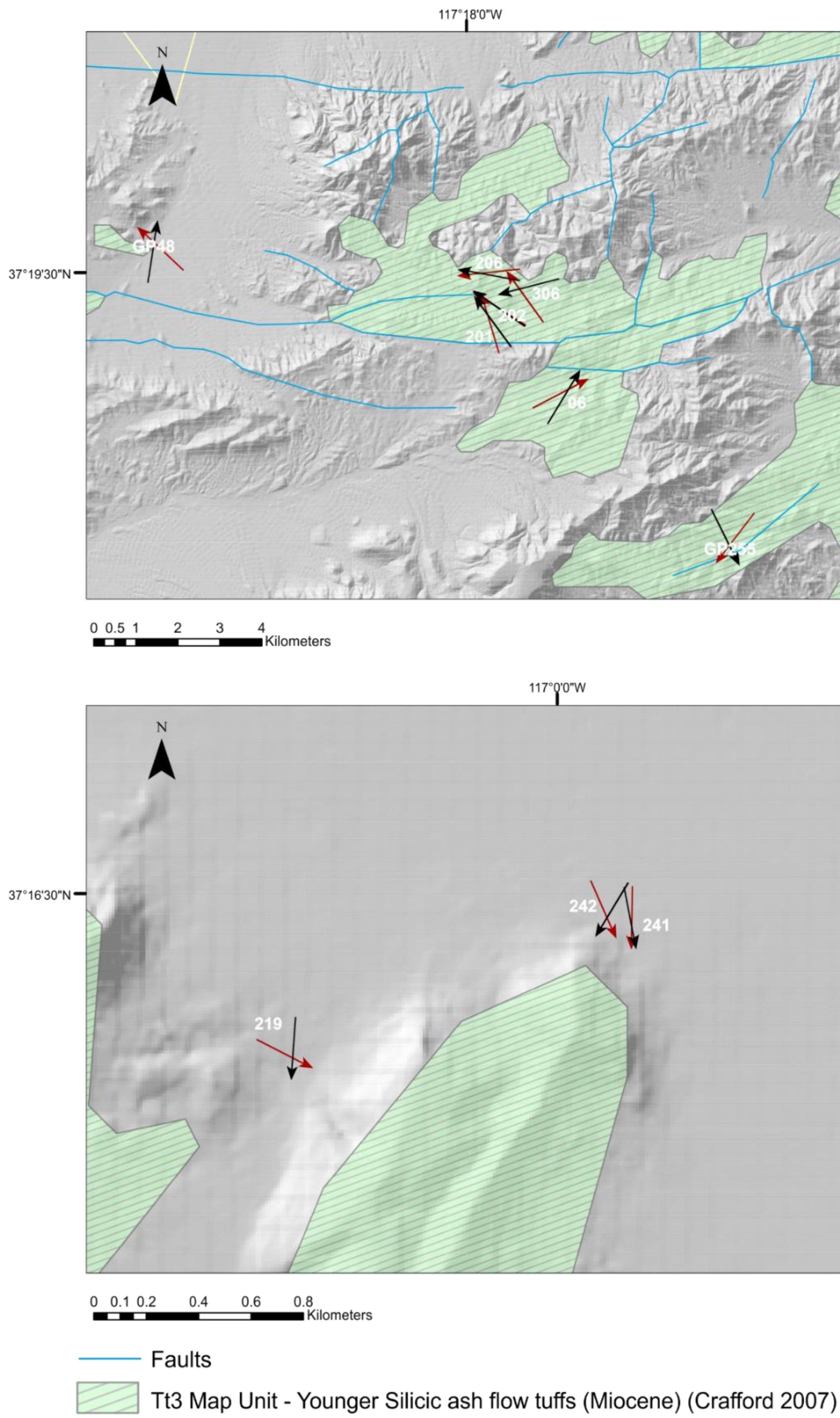

Figure 6.9. Enlargement showing AMS susceptibility directions zoomed in from the condensed map

Table 6.3. AMS Results for Gold Point Tuffs

Site	Unit	n/N	K1	K2	K3	K1 Dec (°)	K1 Inc (°)	K1 Dec E (°)	K1 Inc E (°)	K2 Dec (°)	K2 Inc (°)	K2 Dec E (°)	K2 Inc E (°)	K3 Dec (°)	K3 Inc (°)	K3 Dec E (°)	K3 Inc E (°)
GP06	OW	31	1.009	1.005	0.986	227.2	15.1	33.2	7.8	317.4	0.6	33.2	7.0	49.6	74.9	8.7	6.9
GP48	TM	34/35	1.006	1.004	0.990	172.9	14.7	33.7	6.2	80.1	10.6	33.6	5.9	315.6	71.8	7.2	6.0
GP63	OW	41	1.005	1.004	0.991	32.4	12.5	44.7	6.1	135.8	46.3	44.7	5.3	291.3	41.0	6.4	5.0
GP86	TM	28	1.009	1.007	0.984	291.7	7.5	33.8	4.4	200.7	8.0	33.8	4.9	64.3	78.9	4.9	4.5
GP201	SF	33/36	1.006	1.003	0.991	143.8	17.0	19.2	4.7	235.1	4.2	19.2	8.6	338.7	72.4	8.9	4.9
GP202	SF	37	1.006	1.002	0.992	124.6	44.8	19.0	7.1	33.5	1.1	19.0	10.4	302.4	45.2	10.5	7.2
GP206	SF	46/47	1.006	1.004	0.990	107.3	30.3	39.6	7.2	12.9	7.3	39.6	7.0	270.8	58.6	7.6	6.7
GP219	TM	37	1.009	1.008	0.982	4	8.2	63.9	4.6	271.3	18.2	63.9	4.2	117.1	69.9	4.9	4.2
GP241	SF	35	1.014	1.008	0.978	349.2	28.6	18.6	7.0	82.0	5.1	18.6	7.8	181.1	60.8	8.1	6.7
GP242	SF	21	1.014	1.010	0.976	31.2	25.9	33.0	7.7	286.0	28.3	33.1	14.5	156.4	49.9	14.9	7.9
GP255	TM	43	1.011	1.007	0.982	333.5	61.1	24.5	4.8	121.0	24.9	24.5	5.3	217.5	13.6	6.5	3.0
GP285	TM	30	1.003	1.003	0.994	314.2	14.7	44.5	6.5	216.8	26.4	44.5	4.5	70.4	59.3	6.5	4.8
GP292	SF	26	1.007	1.007	0.986	263.3	22.5	52.7	6.6	359.0	13.6	52.7	4.7	117.7	63.3	6.9	4.9
GP306	TM	30	1.017	1.013	0.970	75.6	13.0	33.2	7.0	172.9	29.1	33.2	5.8	324.2	57.6	8.0	4.5

Table 6.4. AMS Susceptibility Parameters for Gold Point Tuffs

Site	Unit	n/N	K1	K2	K3	K1 Dec (°)	K1 Inc (°)	K1 Dec E (°)	K1 Inc E (°)	K2 Dec (°)	K2 Inc (°)	K2 Dec E (°)	K2 Inc E (°)	K3 Dec (°)	K3 Inc (°)	K3 Dec E (°)	K3 Inc E (°)
GP06	OW	31	1.009	1.005	0.986	227.2	15.1	33.2	7.8	317.4	0.6	33.2	7.0	49.6	74.9	8.7	6.9
GP48	TM	34/35	1.006	1.004	0.990	172.9	14.7	33.7	6.2	80.1	10.6	33.6	5.9	315.6	71.8	7.2	6.0
GP63	OW	41	1.005	1.004	0.991	32.4	12.5	44.7	6.1	135.8	46.3	44.7	5.3	291.3	41.0	6.4	5.0
GP86	TM	28	1.009	1.007	0.984	291.7	7.5	33.8	4.4	200.7	8.0	33.8	4.9	64.3	78.9	4.9	4.5
GP201	SF	33/36	1.006	1.003	0.991	143.8	17.0	19.2	4.7	235.1	4.2	19.2	8.6	338.7	72.4	8.9	4.9
GP202	SF	37	1.006	1.002	0.992	124.6	44.8	19.0	7.1	33.5	1.1	19.0	10.4	302.4	45.2	10.5	7.2
GP206	SF	46/47	1.006	1.004	0.990	107.3	30.3	39.6	7.2	12.9	7.3	39.6	7.0	270.8	58.6	7.6	6.7
GP219	TM	37	1.009	1.008	0.982	4	8.2	63.9	4.6	271.3	18.2	63.9	4.2	117.1	69.9	4.9	4.2
GP241	SF	35	1.014	1.008	0.978	349.2	28.6	18.6	7.0	82.0	5.1	18.6	7.8	181.1	60.8	8.1	6.7
GP242	SF	21	1.014	1.010	0.976	31.2	25.9	33.0	7.7	286.0	28.3	33.1	14.5	156.4	49.9	14.9	7.9
GP255	TM	43	1.011	1.007	0.982	333.5	61.1	24.5	4.8	121.0	24.9	24.5	5.3	217.5	13.6	6.5	3.0
GP285	TM	30	1.003	1.003	0.994	314.2	14.7	44.5	6.5	216.8	26.4	44.5	4.5	70.4	59.3	6.5	4.8
GP292	SF	26	1.007	1.007	0.986	263.3	22.5	52.7	6.6	359.0	13.6	52.7	4.7	117.7	63.3	6.9	4.9
GP306	TM	30	1.017	1.013	0.970	75.6	13.0	33.2	7.0	172.9	29.1	33.2	5.8	324.2	57.6	8.0	4.5

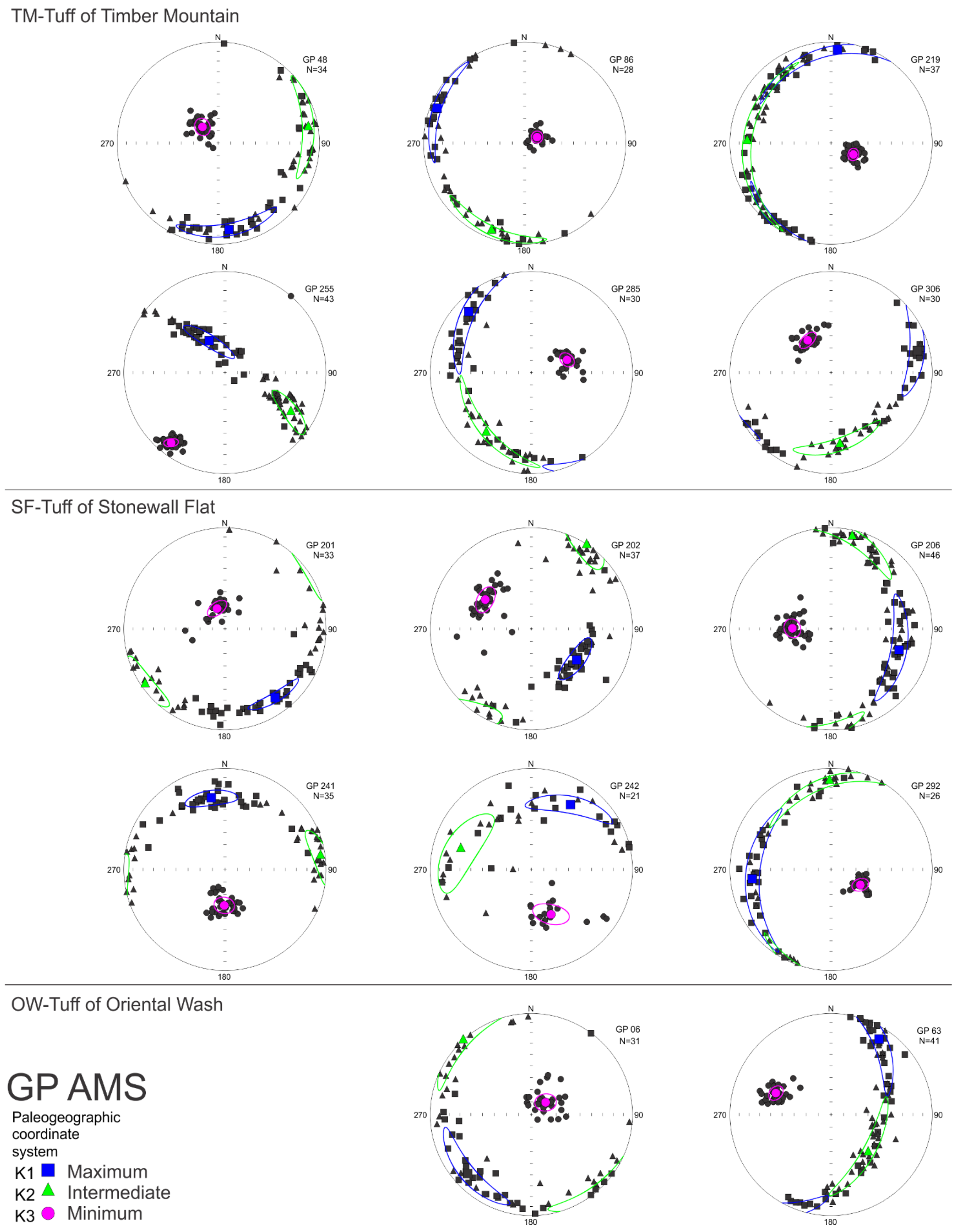

Figure 6.10. AMS measurements for the Gold Point area ignimbrites, TM - Tuff of Timber Mountain, SF – Tuff of Stonewall Flat, OW – Tuff of Oriental Wash. Lower hemisphere, equal area projection with individual specimens black squares (K_1), triangles (K_2) and circles (K_3). Site means (large colored symbols), and 95% confidence ellipses.

6.1.3 AMS – Ignimbrite Density Comparison

To investigate variations in the degree of welding among sites from the Gold Point and Bandelier collections, average density values, as a proxy for intensity of welding, were determined for each site. Measurements of bulk volume (cm^3) and mass (g) for typically nine to ten specimens per sampling site were made. Both collections exhibit varying textures and welding characteristics at the between-site level, and, for at least some sites, at the within-site level. The average bulk density values are compared to the bulk susceptibility (Km), the AMS shape value T (prolate to oblate), and the corrected degree of anisotropy (Pj) (Figure 6.11). In Figures 6.11 (A,C,E), all the analyzed Gold Point sites are compared with Bandelier sites and there is little in the way of correlation between density and any of these parameters, with the exception of a slight increase in mean susceptibility with increasing density. The plots are further sub-divided by separating out the different ignimbrites sampled for the Gold Point collection while keeping all of the Bandelier sites grouped (OW- Tuffs of Oriental Wash, TM-Timber Mountain Tuffs, SF- Stonewall Flat Tuffs, and BAND- Bandelier Tuffs) (Figure 6.11 (B,D,F)). There is no obvious correlation between density and any of the three parameters, again with the exception of a slight increase in mean susceptibility with increasing density.

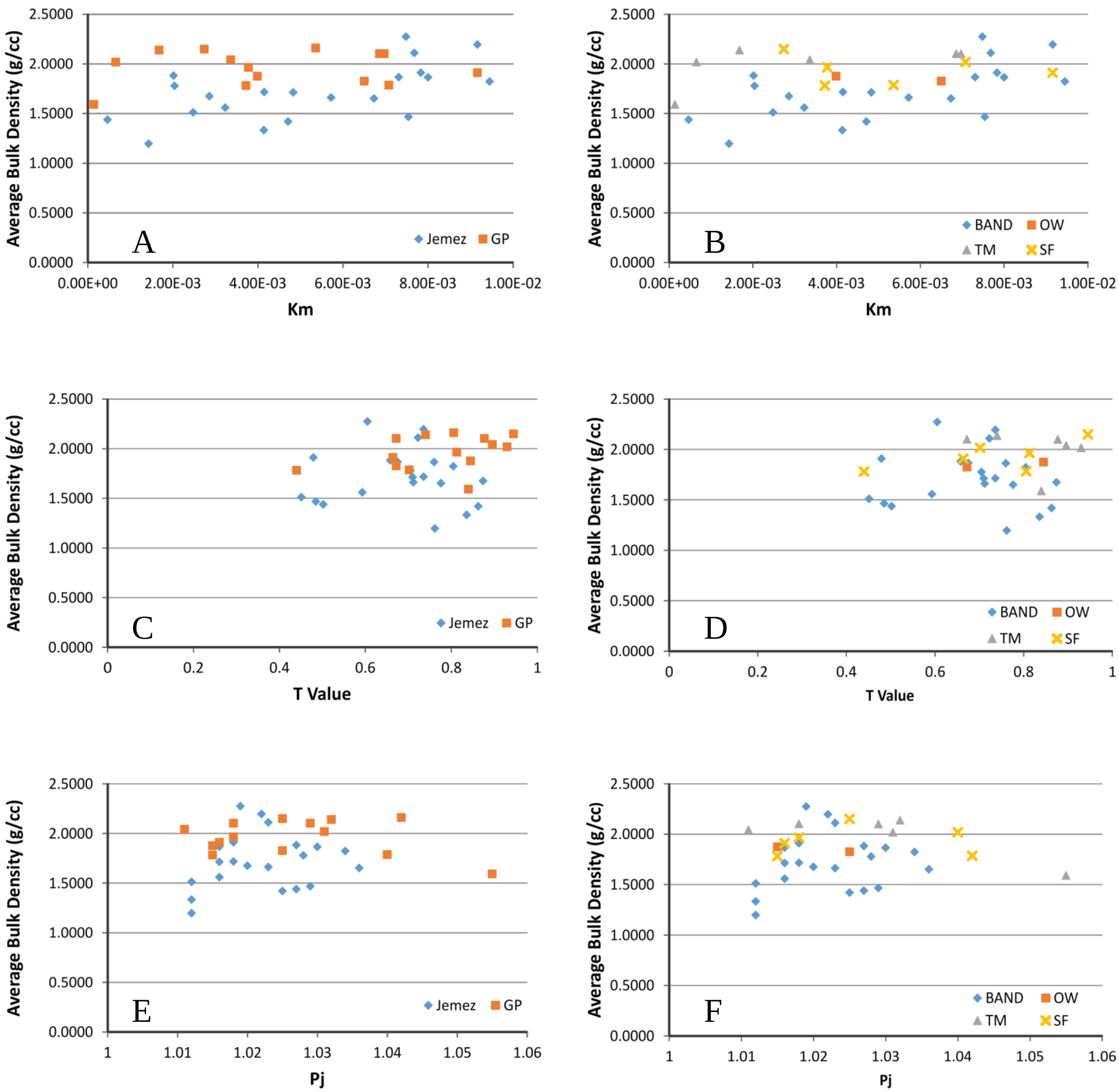

Figure 6.11. Bulk density compared with selected magnetic parameters (Bulk Susceptibility, T value, and percent anisotropy)

6.2 Rock Magnetic Experiments

6.2.1 IRM Acquisition and Backfield Demagnetization

Curves showing the acquisition of isothermal remanent magnetization (IRM) to saturation (SIRM) show essentially complete saturation by 300 mT for all sites in the Bandelier Tuff, with the exception of site 9, which indicates a saturation closer to 350 mT. Specimens from the 18 selected representative sites reveal 80% saturation between 90 and 130 mT (Figure 6.12). Backfield demagnetization data yield coercivity or remanence (H_{cr}) values ranging between 40 and 55 mT for the entire collection of Bandelier Tuff sites, demonstrating that the main magnetic constituent of these ignimbrites is a low coercivity phase, likely a mixture of magnetite and maghemite.

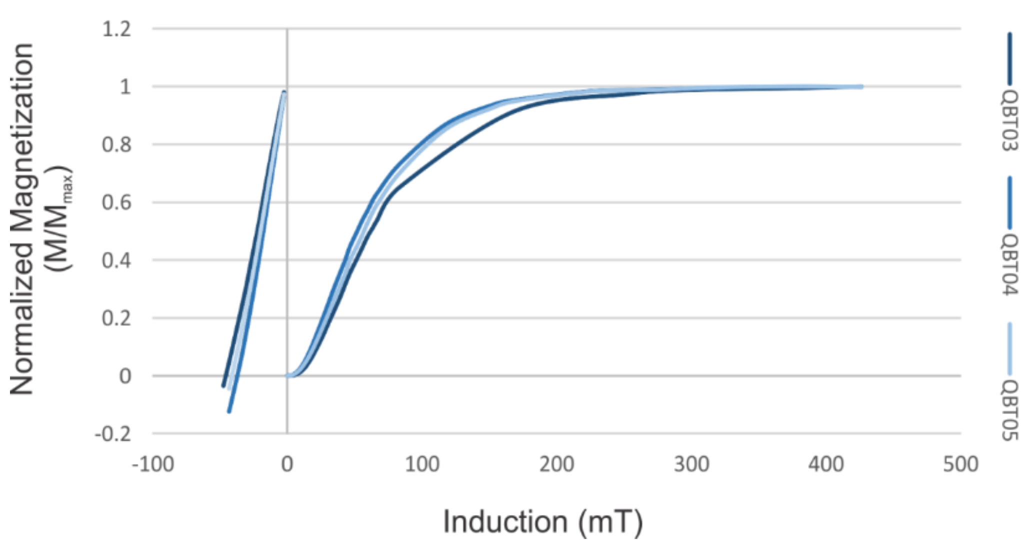

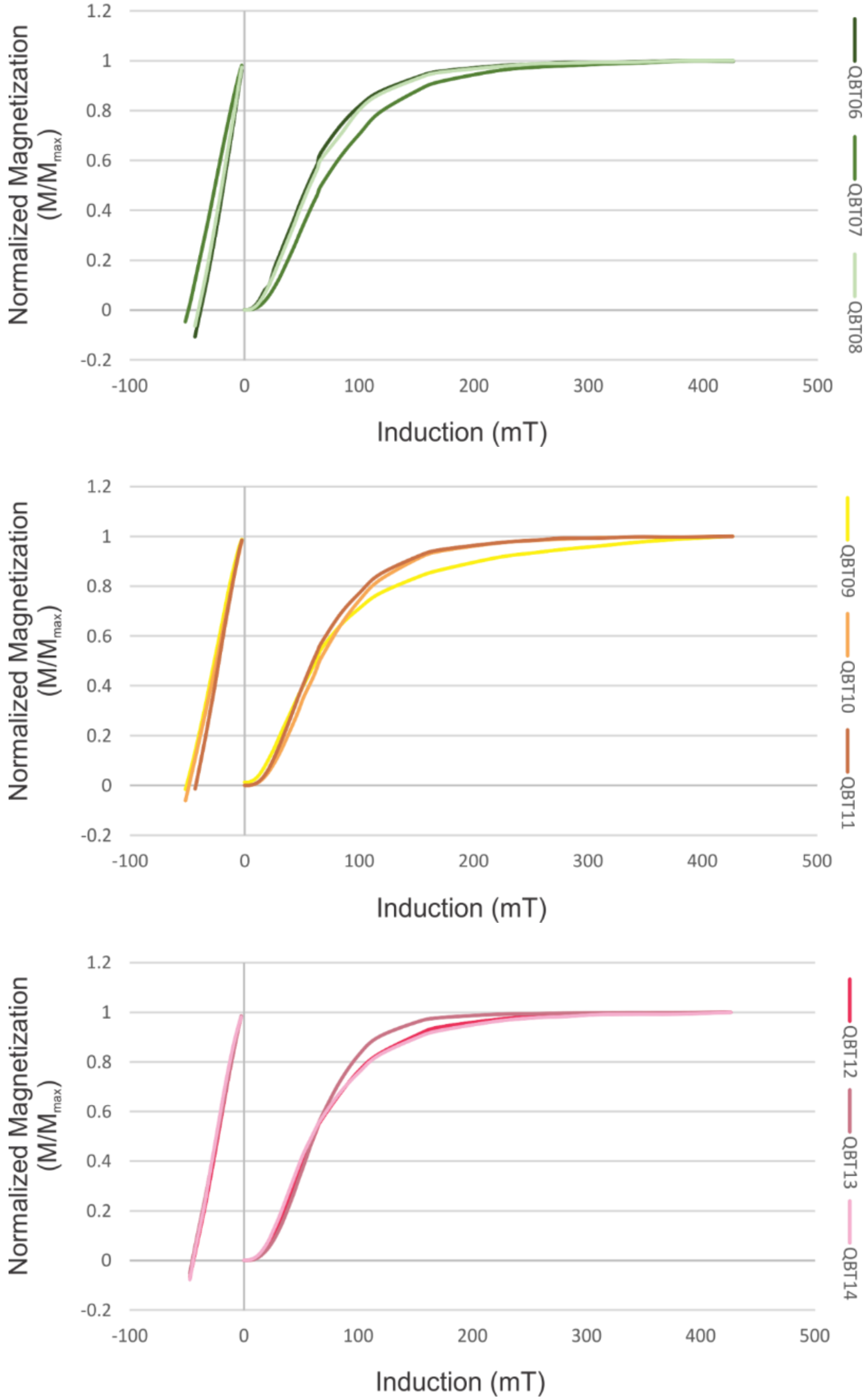
Normalized Magnetization (M/M$_{max}$)
Induction (mT)
QBT06
QBT07
QBT08
Normalized Magnetization (M/M$_{max}$)
Induction (mT)
QBT09
QBT10
QBT11
Normalized Magnetization (M/M$_{max}$)
Induction (mT)
QBT12
QBT13
QBT14

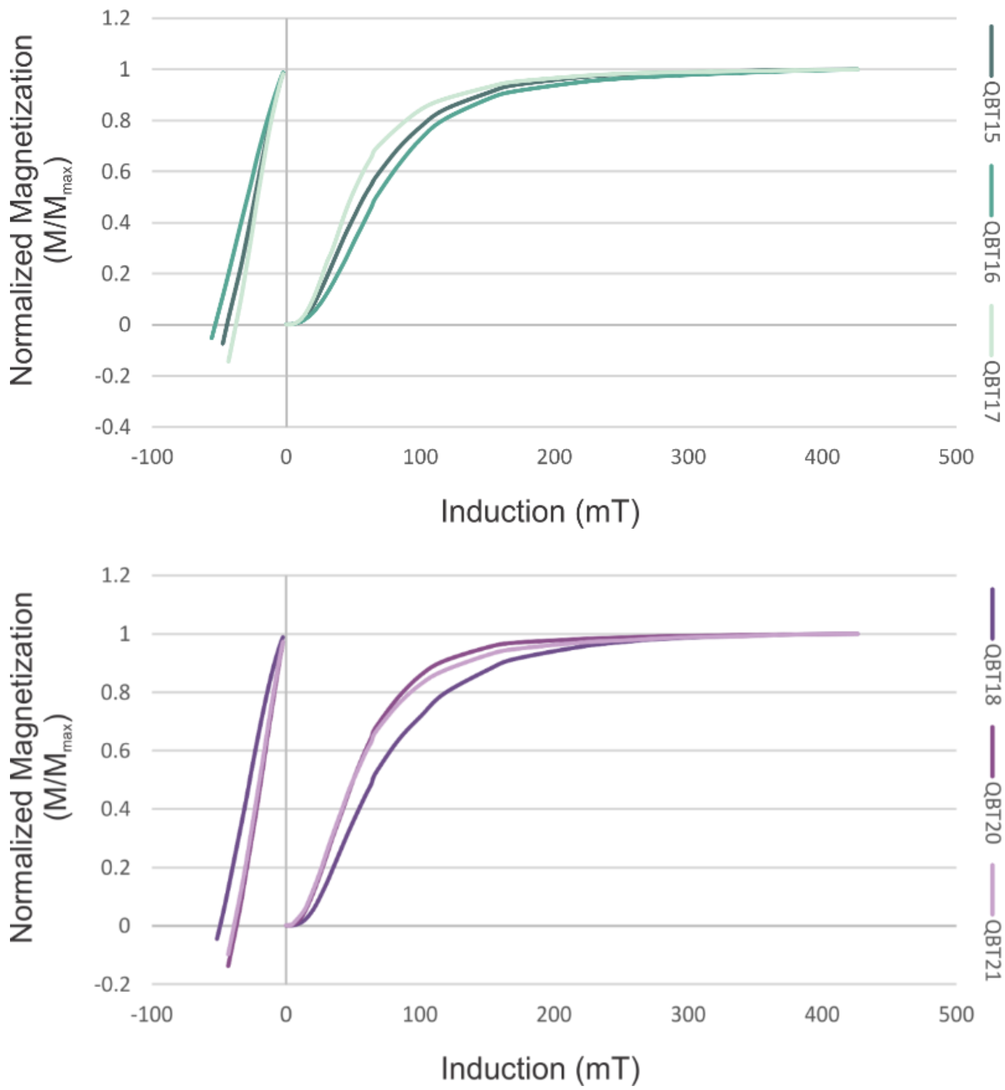

Figure 6.12. IRM acquisition and backfield demagnetization curves

6.2.2 Magnetic Susceptibility vs. Temperature determinations

Material from 20 sites in the Bandelier Tuff was measured, with 19 bulk samples from 17 sites, and 18 magnetic separates (labeled MG) measured on 17 sites. Most specimens show characteristic thermomagnetic response for essentially pure magnetite, demonstrating that it is the principal magnetic phase. All of the magnetic separates show behavior indicating that magnetite is the dominant carrier, with the transition from a ferrimagnetic to paramagnetic state near the Curie temperature of 580 - 585°C. All 20 magnetic separates show a sharp decrease in the slope of the susceptibility curve at or near 580°C. Bulk samples from sites 2, 9, and 21 yield irreversible curves, with an increase in susceptibility upon cooling, suggesting some mineralogic changes. The bulk samples from sites 14 and 17 show curves indicating a phase with a Curie temperature between 620 and 630° C, implying maghemite as an important contributor. Magnetic extracts from these sites, however, yield thermomagnetic curves that are more consistent with nearly pure magnetite (Figure 6.13).

Of the Tuffs from Gold Point, six of the sites are in the Stonewall Flat Tuff (GP 201, 202, 206, 241, 242, and 292), and three are in the Timber Mountain Tuffs (GP 219, 255, and 285). Bulk extracts were measured on all 9 of the selected sites and magnetic extracts (MG) were measured for GP206, GP219, GP242, and GP285. The Stonewall Flat Tuff samples show considerable variation in thermomagnetic behavior. Site GP201 and GP241 show a rapid decrease in susceptibility at 580°C indicating magnetite as the dominant magnetic carrier. Sites GP202, 206 and 292 have a slight decrease in the susceptibility curve before it increases again between 350 and 450°C indicating maghemite present. Sites GP202, 206, and 242 also have a slight increase in susceptibility of the heating curve indicating the possibility of formation of new minerals being created and then a drop off of the curve between 610 - 620°C showing that in these sites maghemite is the dominant carrier. GP292's heating curve is much lower susceptibility than the cooling curve and has a slight decrease in susceptibility between 360-410°C and then a sharp increase in susceptibility before dropping off around 610°C which is likely a contribution of both magnetite and maghemite being present. Many of the curves are slight to moderate shaped "peaks" however; a sharp Hopkinson Peak is seen right as the susceptibility has a steep drop off around 540°C.

With the three Timber Mountain samples, those for site GP219 and GP 255 both have much higher susceptibility cooling curves than heating curves and a rapid decrease in the susceptibility curves at 580°C indicating that magnetite is the dominant mineral phase. GP285 heats to 600°C and then rapidly decreases in susceptibility at 620°C, which represents maghemite as the dominant carrier (Figure 6.14).

6.2.2a Bandelier Tuff Examples

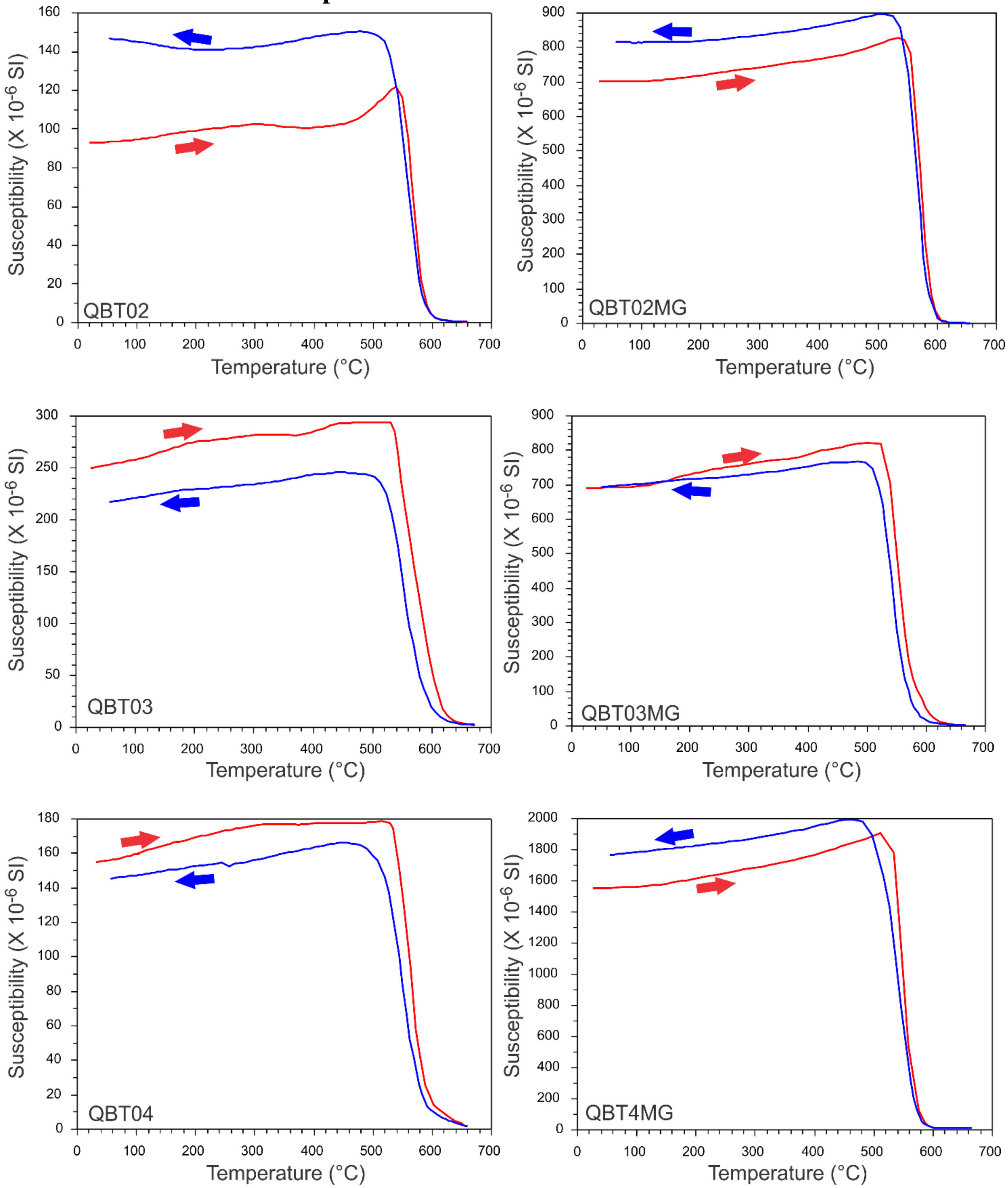

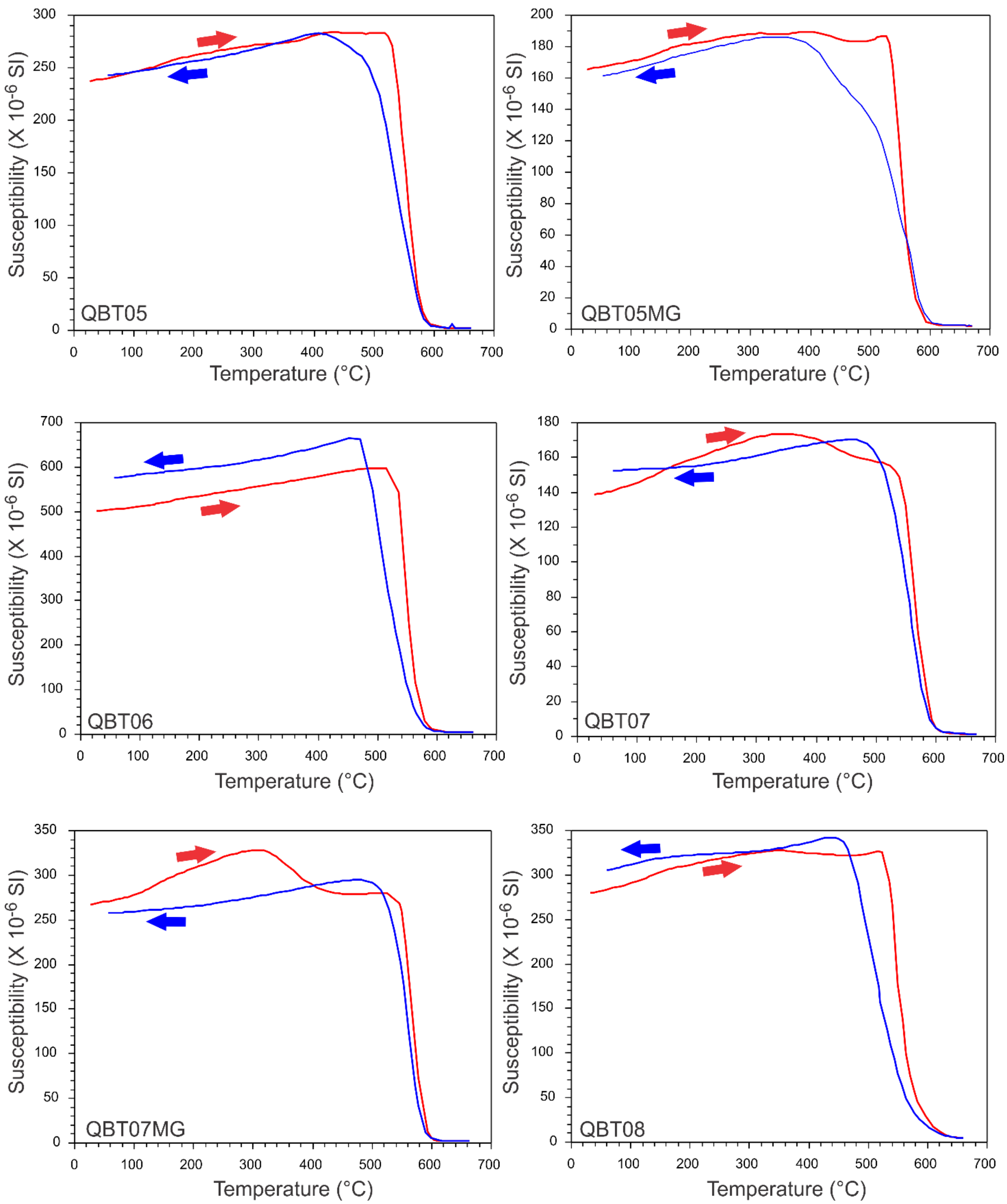
QBT05
QBT05MG
QBT06
QBT07
QBT07MG
QBT08
Susceptibility (X 10^{-6} SI)
Temperature (°C)

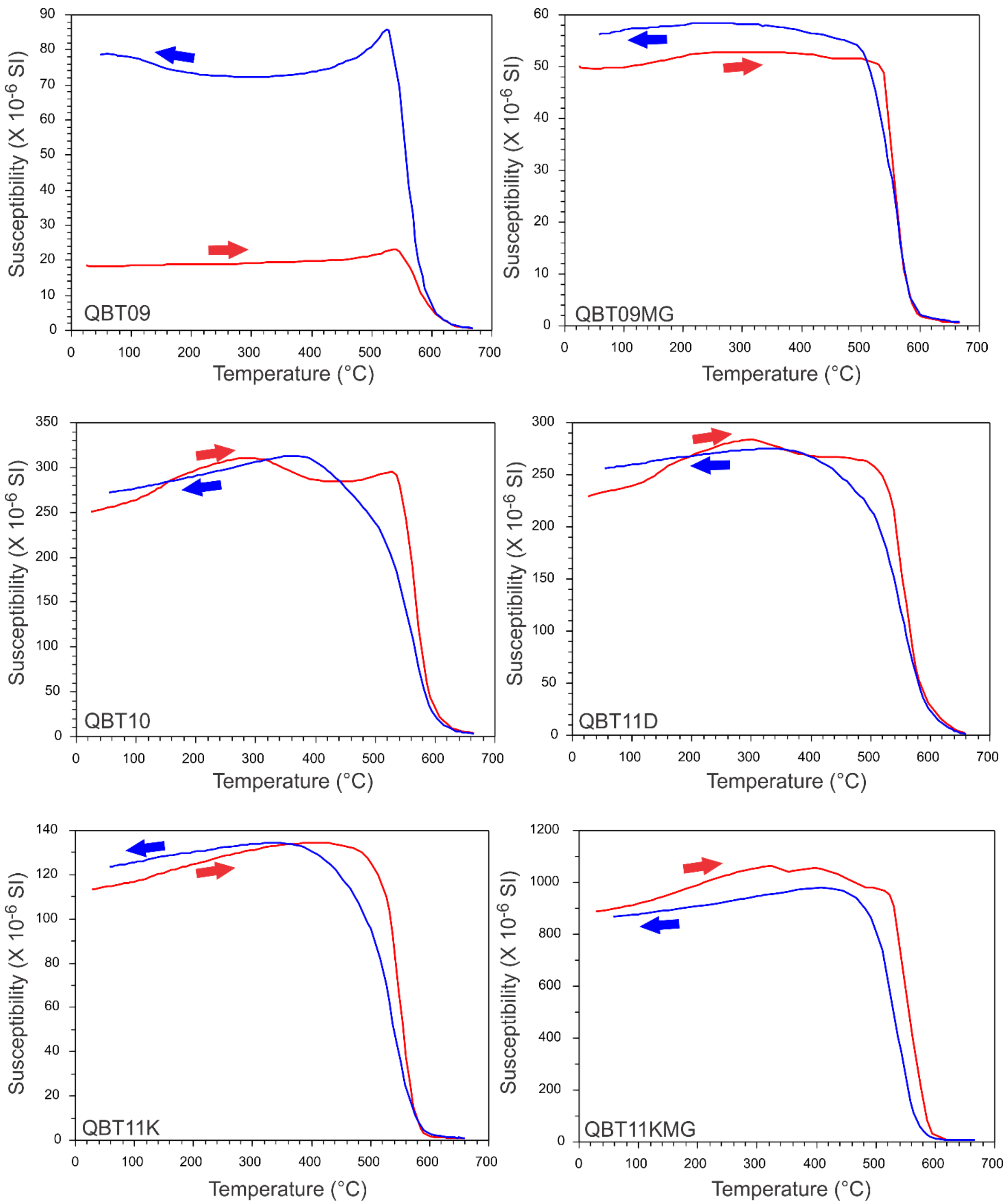
QBT09
QBT09MG
QBT10
QBT11D
QBT11K
QBT11KMG
Susceptibility (X 10-6 SI)
Temperature (°C)

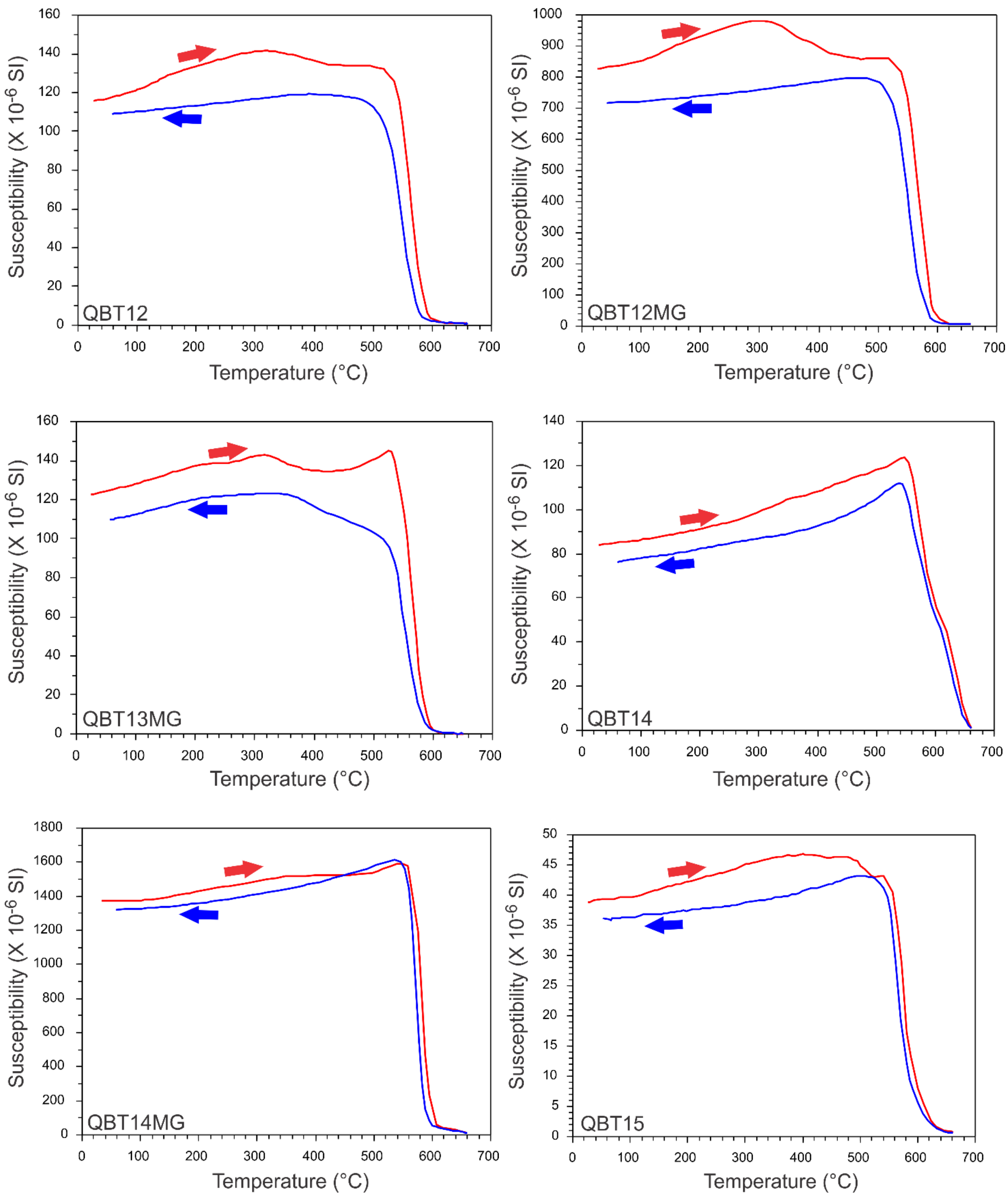
QBT12
QBT12MG
QBT13MG
QBT14
QBT14MG
QBT15
Susceptibility (X 10^{-6} SI)
Temperature (°C)
0
100
200
300
400
500
600
700

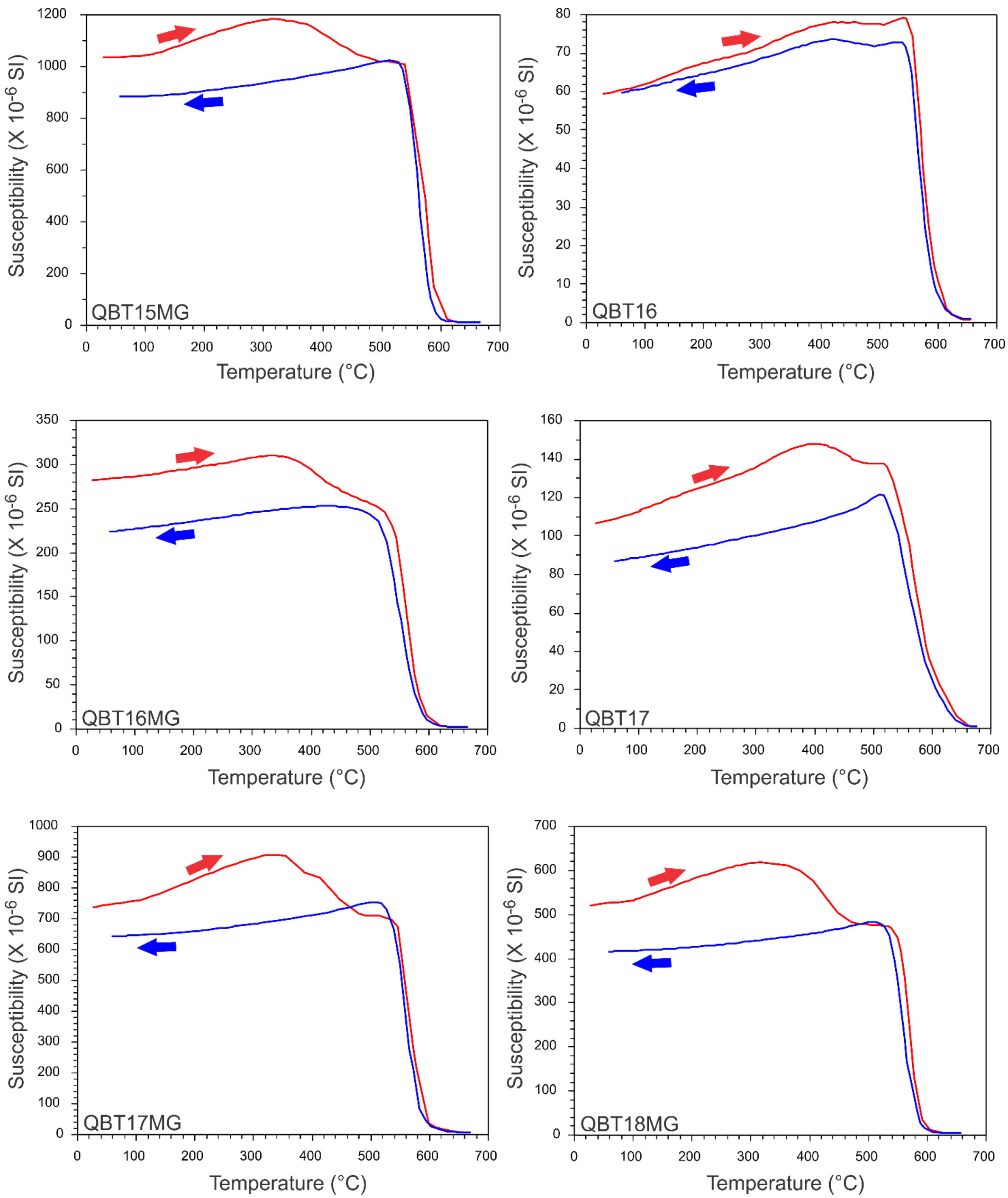
QBT15MG
QBT16
QBT16MG
QBT17
QBT17MG
QBT18MG
Susceptibility (X 10^{-6} SI)
Temperature (°C)

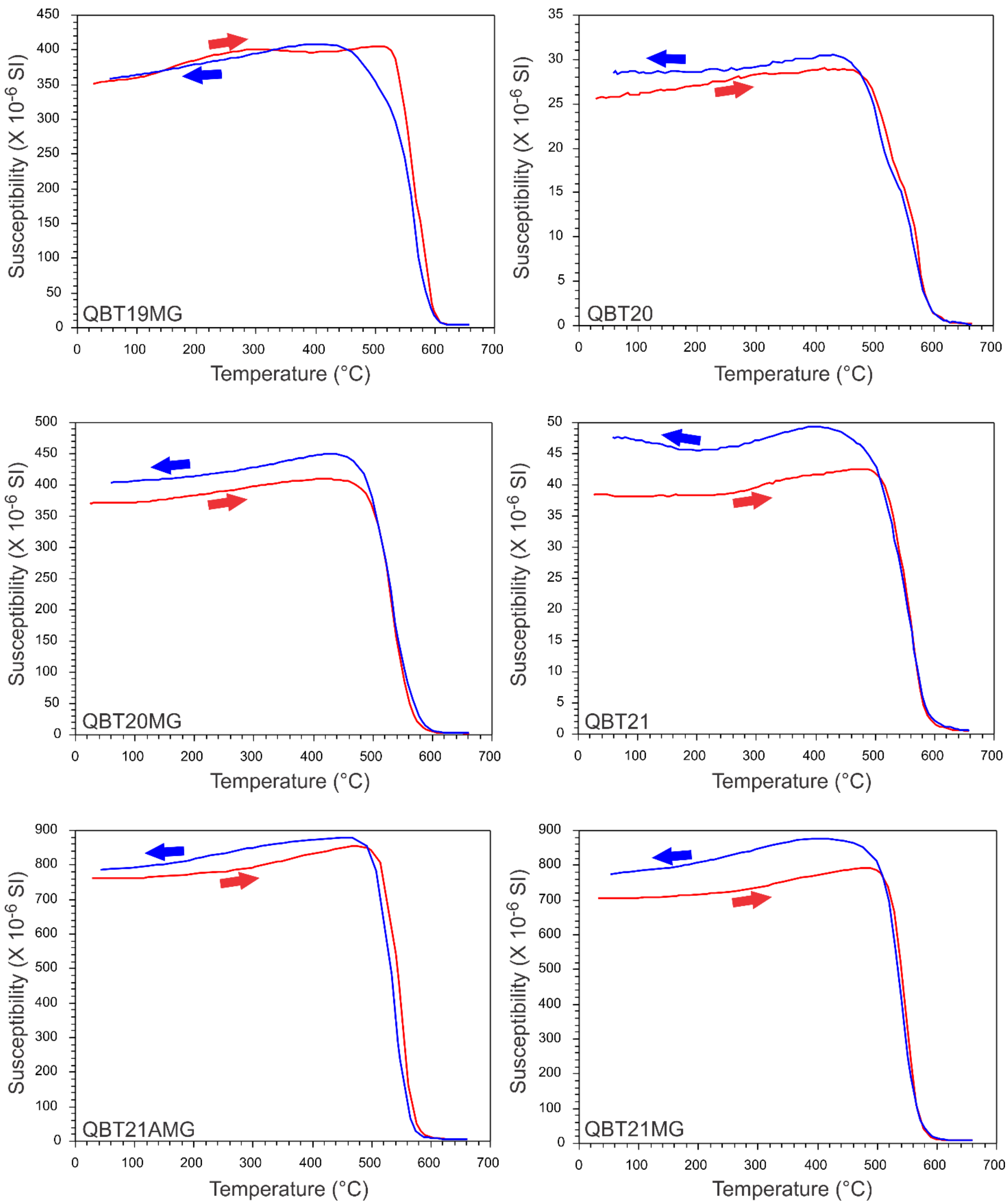

Figure 6.13. Magnetic susceptibility versus temperature curves for samples from Bandelier Tuff sites. All runs performed in an inert atmosphere.

6.2.2b Gold Point Examples

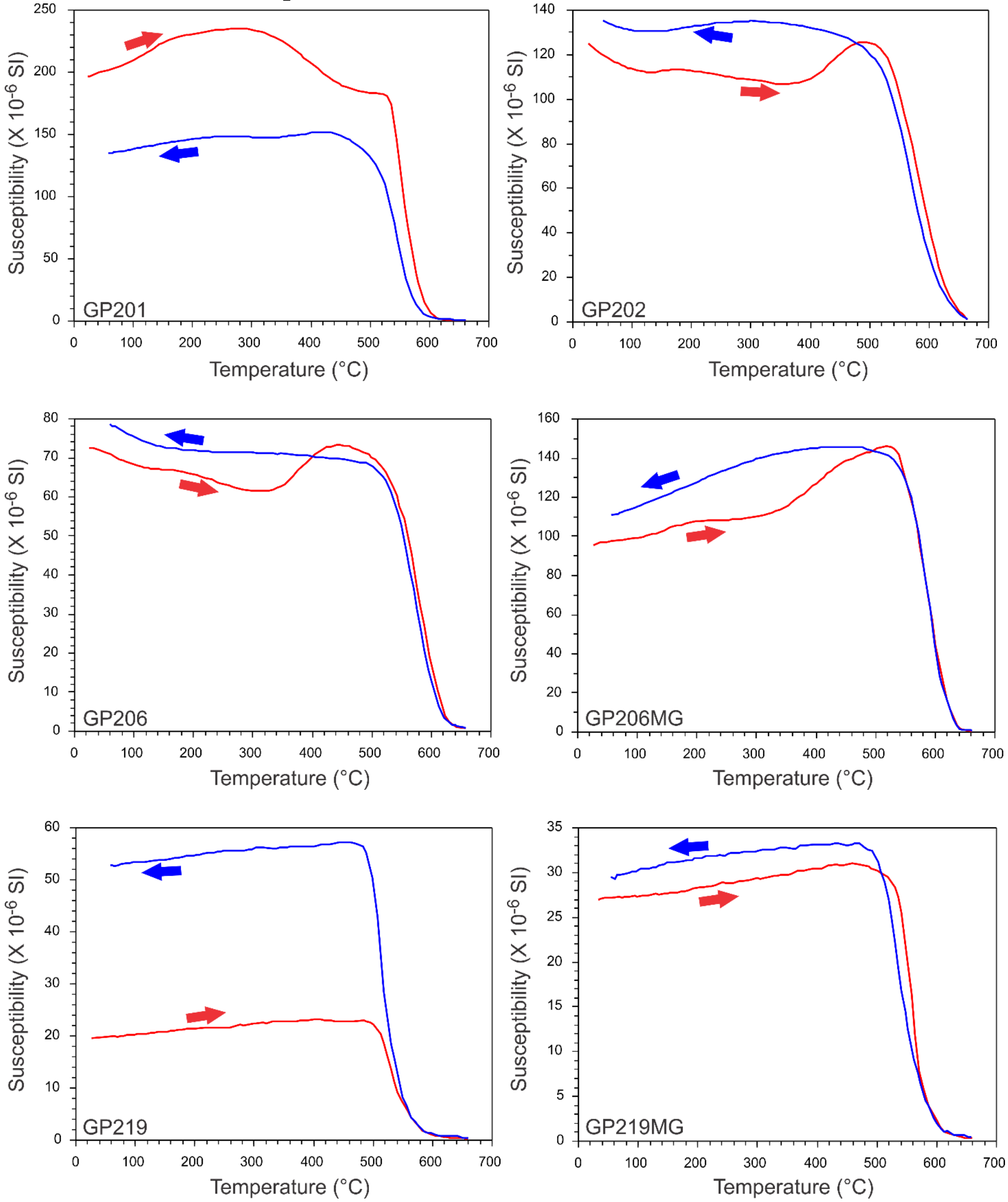

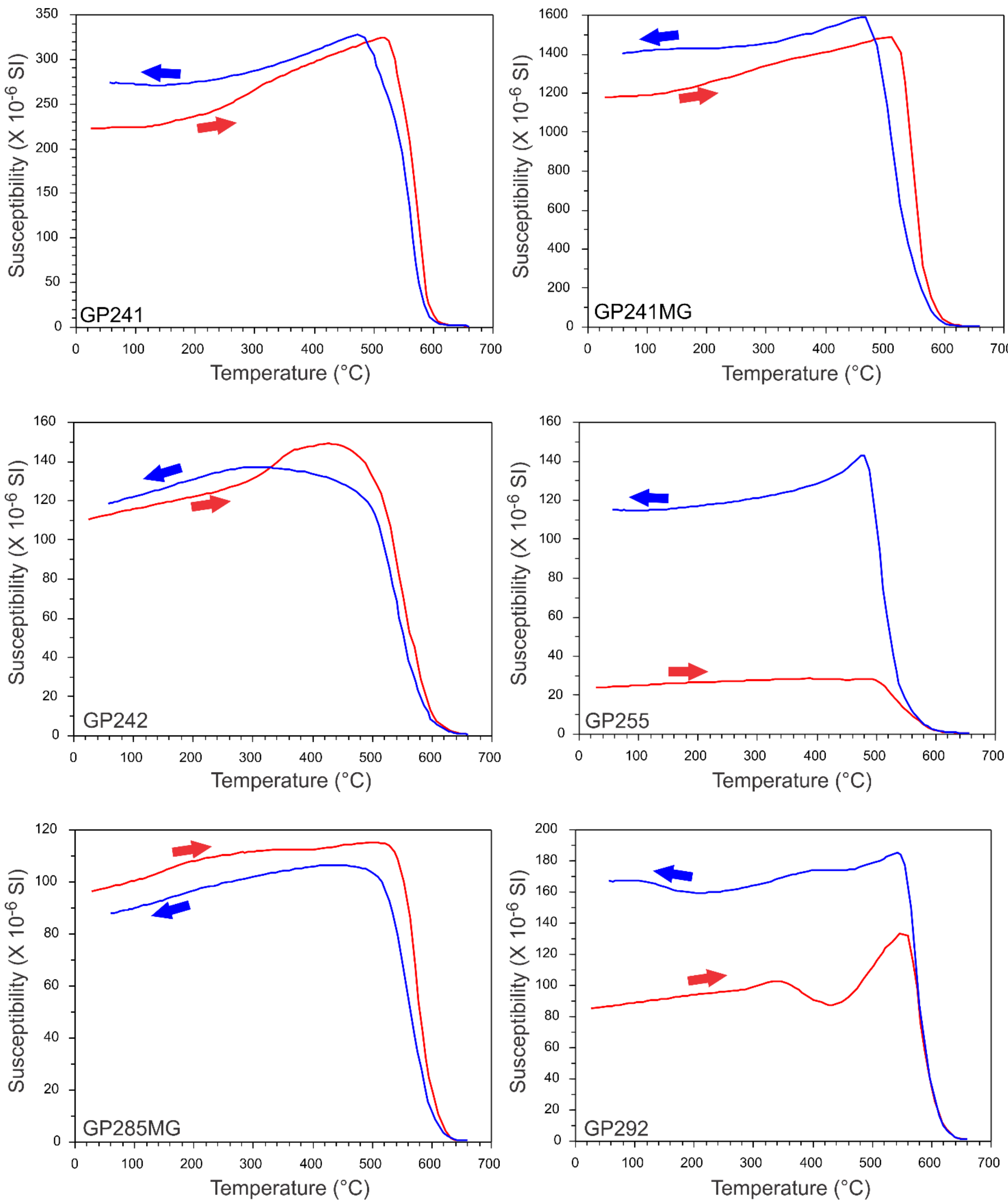

Figure 6.14. Magnetic susceptibility versus temperature curves for samples from Gold Point area sites

6.2.3 Magnetic Hysteresis Curves

Hysteresis measurements provide an essential tool for rock magnetic research by characterizing the magnetic mineralogy and grain size relations for an assemblage of particles based on the loops shapes. Hysteresis parameters include saturation magnetization M_s, saturation remanent magnetization M_r, coercivity H_c and remanent coercivity H_{cr} (Figure 5.2) (Jackson and Solheid, 2010). The ratios H_{cr}/H_c and M_r/M_s are used as one approach to evaluating bulk hysteresis magnetic properties to identify the domain state i.e., particle size (Day et al., 1977; Muxworthy and Roberts 2007). These ratios exhibit relative variations in domain state, which indicates magnetic grain size for samples dominated by titanomagnetite and magnetite (Roberts et al. 2000). Data analyzed from the Bandelier Tuff samples and the Gold Point Samples indicate a predominantly pseudo-single domain (PSD) state as shown on Day Plots (Figure 6.15). Average M_r/M_s and H_{cr}/H_c ratios for the Bandelier tuff are 0.15 and 2.72 respectively, consistent with the magnetic hysteresis properties of pure PSD magnetite (Table 6.5). Average M_r/M_s and H_{cr}/H_c ratios for the Gold Point Tuffs are 0.14 and 2.56 respectively (Table 6.6), also consistent with the magnetic hysteresis properties of pure PSD magnetite (Figure 6.16) (Roberts et al., 1995).

Table 6.5. Magnetic Hysteresis Parameters for Bandelier Tuff

Site	Specimen	Hc (mT)	Mr (μAm^2)	Ms ($\mu Am^2/T$)	Hcr (mT)	Mr/Ms	Hcr/Hc
QBT01	Ob	18.85	7.676	40.13	41.85	0.19	2.22
QBT01.2	Ob	18.88	7.479	36.97	42.94	0.20	2.27
QBT01.3	Ob	19.74	10.25	50.41	44.64	0.20	2.26
QBT02	Ka	18.63	4.911	31.77	47.53	0.15	2.55
QBT02.2	Ka	17.42	11.81	88.78	44.65	0.13	2.56
QBT02.3	Ka	17.72	7.399	47.73	46.16	0.16	2.60
Qbt03	Pb	15.24	4.656	29.45	43.16	0.16	2.83
QBT03.2	Pb	14.7	6.959	48.93	43.94	0.14	2.99
QBT03.3	Pb	15.34	15.12	95.9	43.88	0.16	2.86
QBT04	Jb	13.28	8.863	70.45	39.28	0.13	2.96
QBT04.2	Jb	12.29	8.625	73.01	36.2	0.12	2.95
QBT04.3	Jb	10.99	12.57	118.1	32.82	0.11	2.99
QBT05	Bb	13.18	7.065	52.74	37.4	0.13	2.84
QBT05.2	Bb	12.24	6.039	52.54	37.05	0.11	3.03
QBT05	Lc	10.92	12.43	116.8	33.41	0.11	3.06
QBT06	Lb	12.61	6.811	68.64	43.74	0.10	3.47
QBT06.2	Lb	9.867	5.013	60.1	36.7	0.08	3.72
QBT06.3	Lb	10.52	7.769	93	40.02	0.08	3.80
QBT07	Sb	18.06	6.536	39.77	46.08	0.16	2.55
QBT07.2	Sb	17.44	6.74	42.99	45.09	0.16	2.59
QBT07.3	Sb	19.79	8.003	47.49	51.47	0.17	2.60
QBT08	Ac	12.12	9.545	91.59	39.77	0.10	3.28
QBT08.2	Ac	12.12	6.741	65.51	39.78	0.10	3.28
QBT08.3	Ac	12.44	8.28	77.18	39.97	0.11	3.21
QBT09	Sc	14.97	1.332	7.923	45.71	0.17	3.05
QBT09.2	Sc	15.36	0.7569	4.375	45.34	0.17	2.95
QBT09.3	Sc	15.53	1.993	11.47	45.79	0.17	2.95
QBT10	Fa	18.53	24.4	160.2	44.01	0.15	2.38
QBT10.2	Fa	19.15	25.48	157.7	45.57	0.16	2.38
QBT10.3	Fa	20.09	14.34	92.01	49.07	0.16	2.44
QBT11	Ad	14.77	11.55	81.71	40.07	0.14	2.71
QBT11	Ra	19.56	5.57	34.27	46.6	0.16	2.38
QBT11	Ub	18.99	9.287	54.77	44.18	0.17	2.33
QBT12	Hc	18.31	11.65	68.75	41.92	0.17	2.29
QBT12	Aa	16.88	13.04	94.59	43.06	0.14	2.55
QBT12.2	Aa	15.99	10.25	76.35	40.85	0.13	2.55
QBT13	Hc	17.83	15.35	93.12	42.55	0.16	2.39
QBT13.2	Hc	17.71	14.98	95.64	44.03	0.16	2.49
QBT13.3	Hc	17.98	10.01	63.79	44.65	0.16	2.48
QBT14	Fb	18.74	13.9	69.86	40.63	0.20	2.17
QBT15	Ic	17.78	4.406	25.28	43.15	0.17	2.43
QBT16	Fd	19.54	5.837	31.09	48.94	0.19	2.50
QBT16.2	Fd	19.08	5.004	26.97	48.91	0.19	2.56
QBT17	Jd	15.49	8.272	48.1	36.37	0.17	2.35
QBT17.2	Jd	15.58	5.565	32.11	36.39	0.17	2.34
QBT17	Ob	15.36	13.53	96.03	40.4	0.14	2.63
QBT18	Bb	18.48	5.248	30.01	43.63	0.17	2.36

QBT18	Pb	23.94	6.085	23.74	47.16	0.26	1.97
QBT18.2	Pb	21.62	5.911	26.43	44.82	0.22	2.07
Qbt18.3	Pb	21.62	9.484	43.88	45.71	0.22	2.11
QBT19	Jb	17.55	9.196	68.31	51.67	0.13	2.94
QBT19.2	Jb	16.8	8.954	67.89	49.24	0.13	2.93
QBT19.3	Jb	16.31	8.627	65.55	47.24	0.13	2.90
QBT20	Fc	14.58	1.188	9.023	43.27	0.13	2.97
QBT20	Id	12.45	1.212	10.29	38.56	0.12	3.10
QBT20	Nb	10.56	2.086	24.17	37.3	0.09	3.53
QBT21	Ib	14.53	1.263	7.387	41.54	0.17	2.86
QBT21.2	Ib	12.91	2.245	16.83	39.05	0.13	3.02
QBT21.3	Ib	13.06	0.9793	7.05	38.89	0.14	2.98
Averages						0.15	2.72

Table 6.6. Magnetic Hysteresis Parameters for Gold Point Tuffs

Site	Specimen	Hc (mT)	Mr (μAm^2)	Ms (μAm^2)	Hcr (mT)	Mr/Ms	Hcr/Hc
GP06	Kb	8.22	0.82	8.04	21.05	0.10	2.56
GP48	Hc	15.01	0.69	3.71	37.1	0.18	2.47
GP63	Aa	9.55	1.41	10.46	29.09	0.14	3.05
GP86	Ea	9.89	0.66	5.80	21.22	0.11	2.15
GP201	Fd	14.23	4.48	28.79	36.97	0.16	2.60
GP202	Ja	16.42	1.37	6.05	33.86	0.23	2.06
GP206	A	9.80	0.75	4.89	31.84	0.15	3.25
GP219	Nc	7.14	0.13	1.56	14.88	0.09	2.08
GP241	Pc	6.05	1.27	12.42	19.01	0.10	3.14
GP242	Eb	8.61	2.16	21.43	24.26	0.10	2.82
GP255	Ka	8.88	0.27	2.72	28.71	0.10	3.23
GP285	-	-	-	-	-	-	-
GP292	Ka	10.60	1.51	8.61	23.08	0.18	2.18
GP306	Db	12.30	0.06	0.27	20.7	0.23	1.68
Averages						0.14	2.56

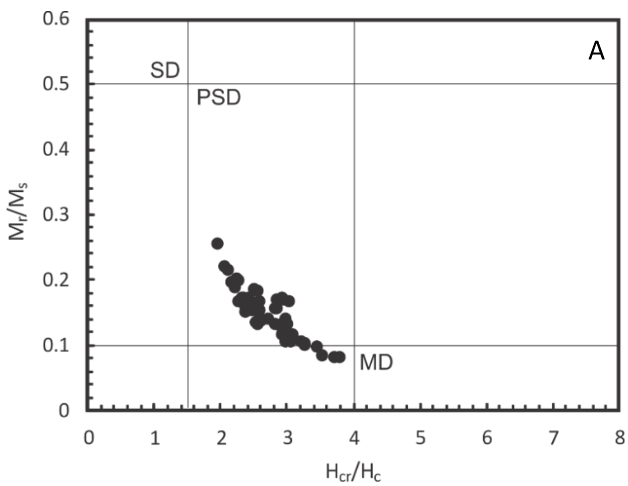

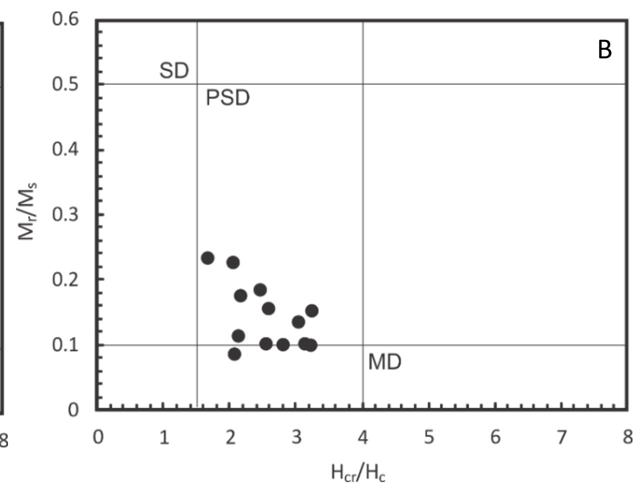

Figure 6.15. Graph A displays Day Plot Data representative of the Bandelier Sites; Graph B is displaying the sites representative of the Gold Point Data

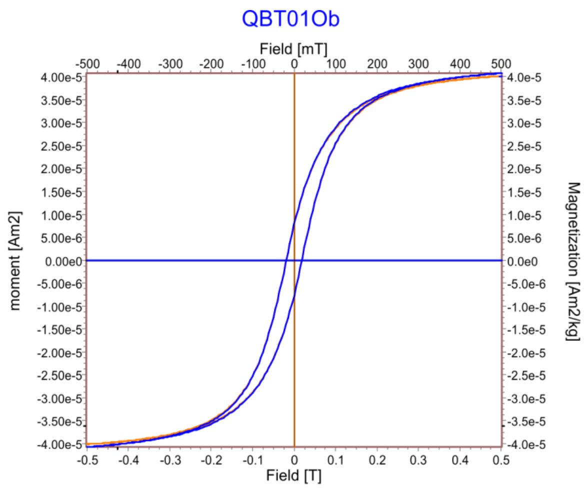
QBT01Ob
Field [mT]
moment [Am2]
Magnetization [Am2/kg]
Field [T]

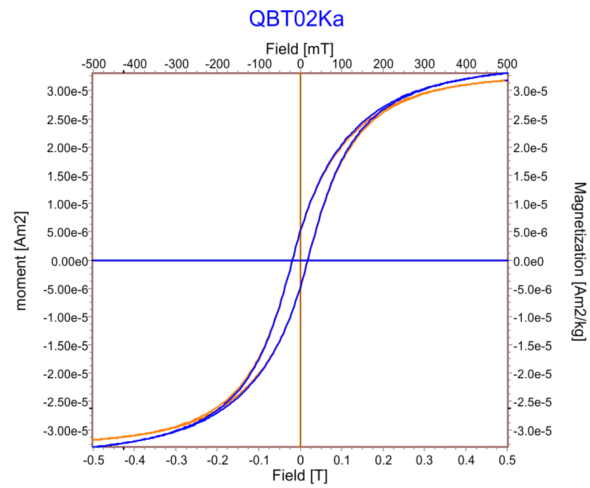
QBT02Ka
Field [mT]
moment [Am2]
Magnetization [Am2/kg]
Field [T]

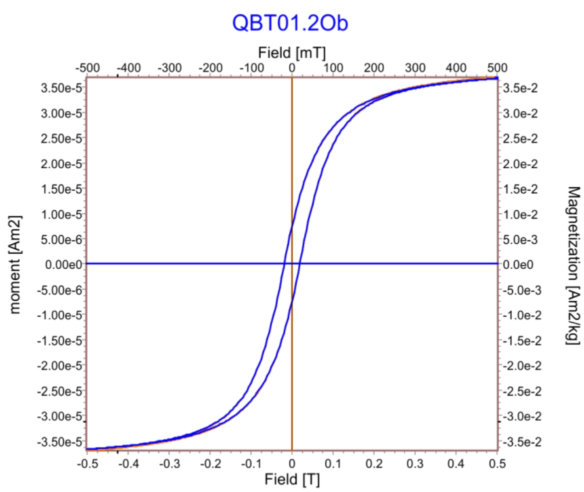
QBT01.2Ob
Field [mT]
moment [Am2]
Magnetization [Am2/kg]
Field [T]

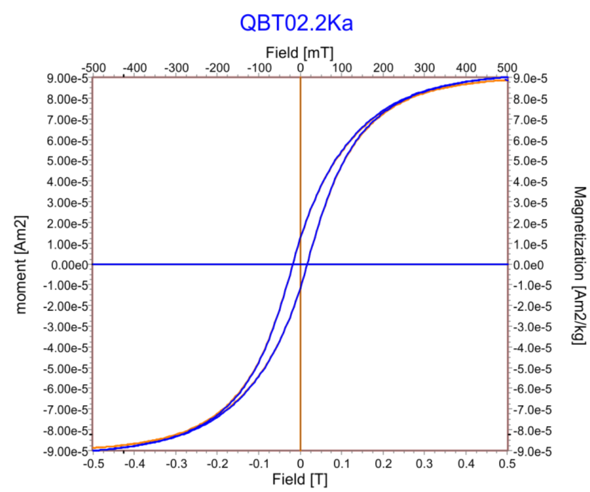
QBT02.2Ka
Field [mT]
moment [Am2]
Magnetization [Am2/kg]
Field [T]

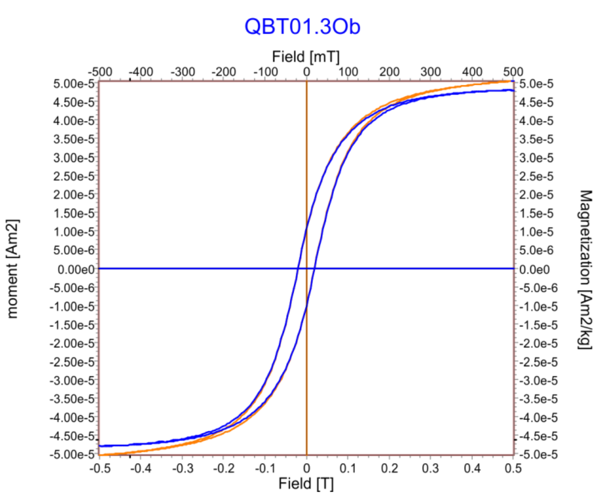
QBT01.3Ob
Field [mT]
moment [Am2]
Magnetization [Am2/kg]
Field [T]

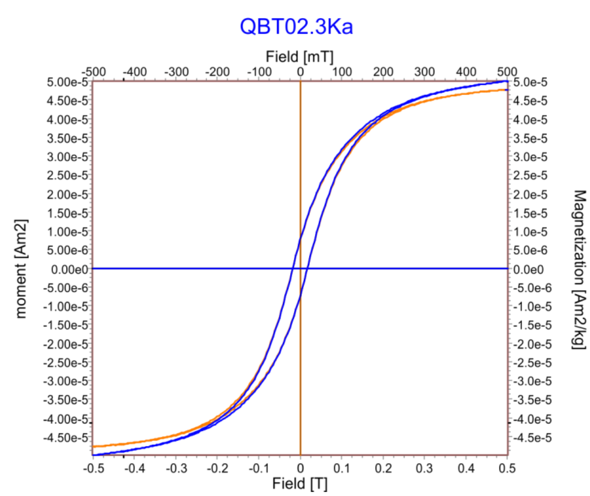
QBT02.3Ka
Field [mT]
moment [Am2]
Magnetization [Am2/kg]
Field [T]

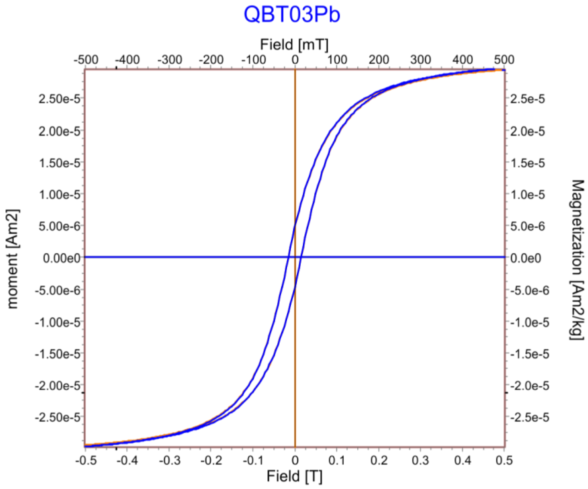
QBT03Pb
Field [mT]
moment [Am2]
Magnetization [Am2/kg]
Field [T]

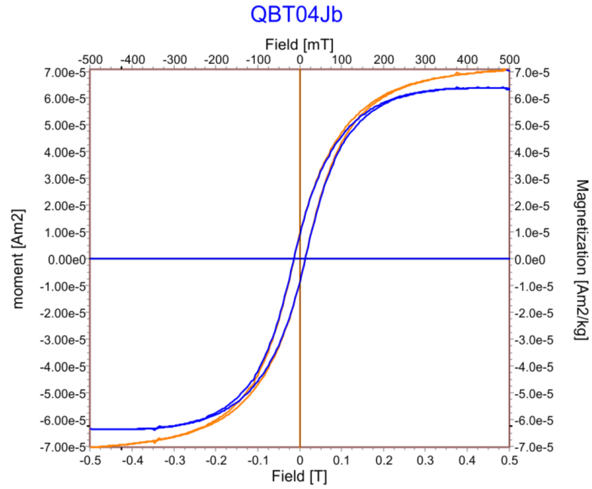
QBT04Jb
Field [mT]
moment [Am2]
Magnetization [Am2/kg]
Field [T]

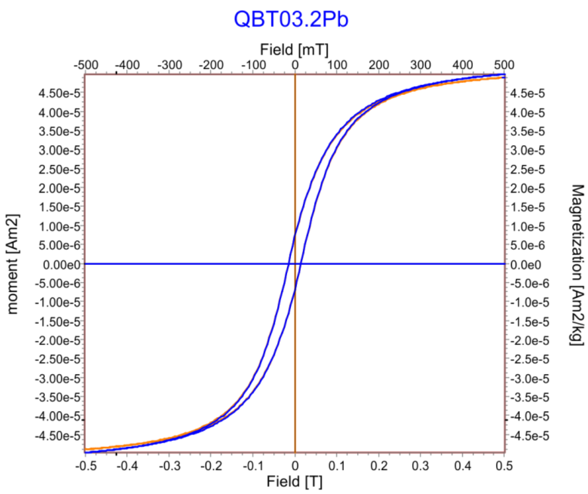
QBT03.2Pb
Field [mT]
moment [Am2]
Magnetization [Am2/kg]
Field [T]

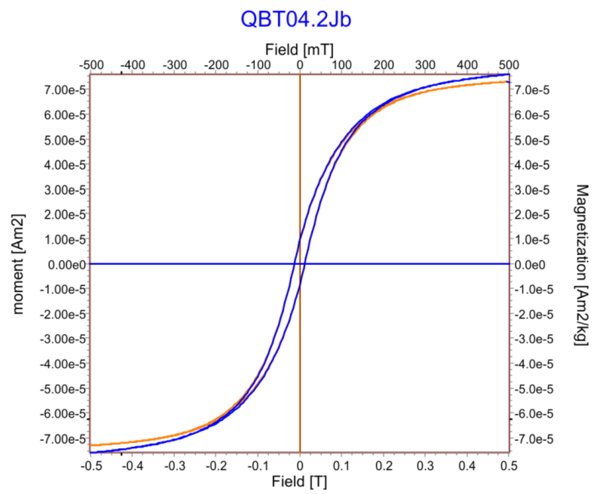
QBT04.2Jb
Field [mT]
moment [Am2]
Magnetization [Am2/kg]
Field [T]

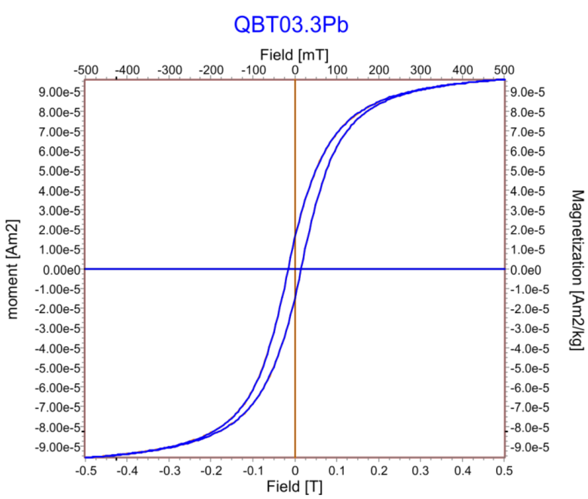
QBT03.3Pb
Field [mT]
moment [Am2]
Magnetization [Am2/kg]
Field [T]

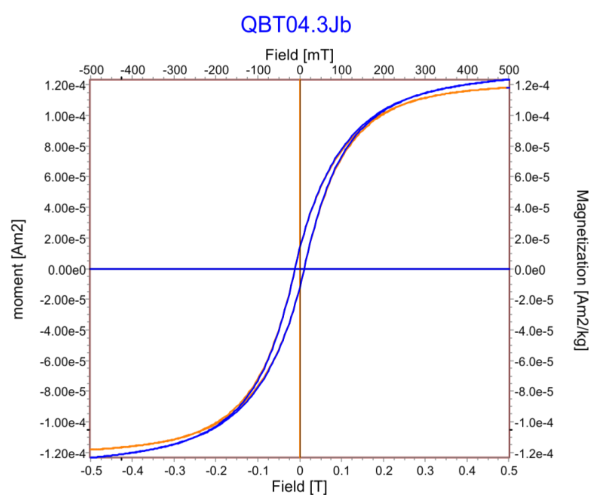
QBT04.3Jb
Field [mT]
moment [Am2]
Magnetization [Am2/kg]
Field [T]

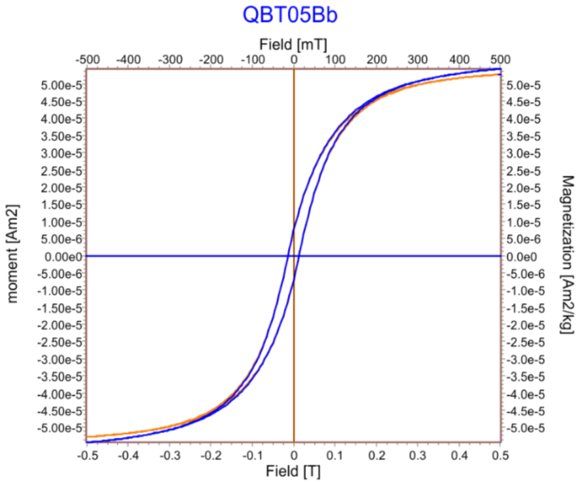
QBT05Bb
Field [mT]
moment [Am2]
Magnetization [Am2/kg]
Field [T]

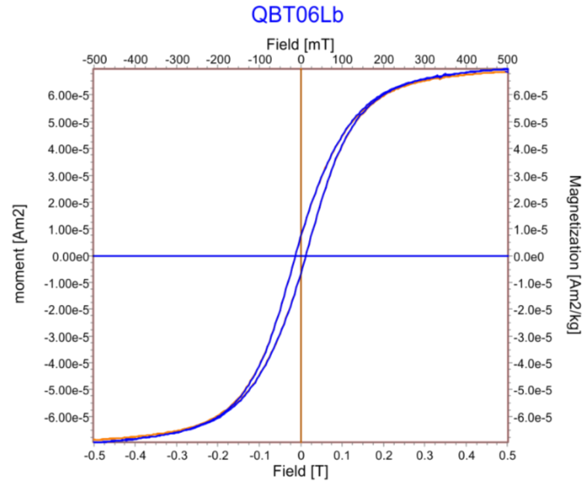
QBT06Lb
Field [mT]
moment [Am2]
Magnetization [Am2/kg]
Field [T]

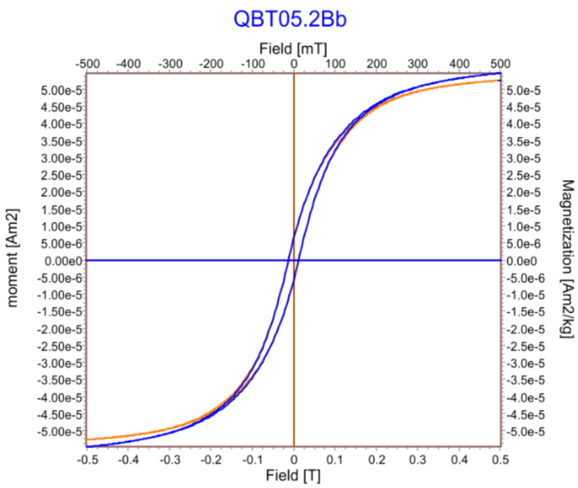
QBT05.2Bb
Field [mT]
moment [Am2]
Magnetization [Am2/kg]
Field [T]

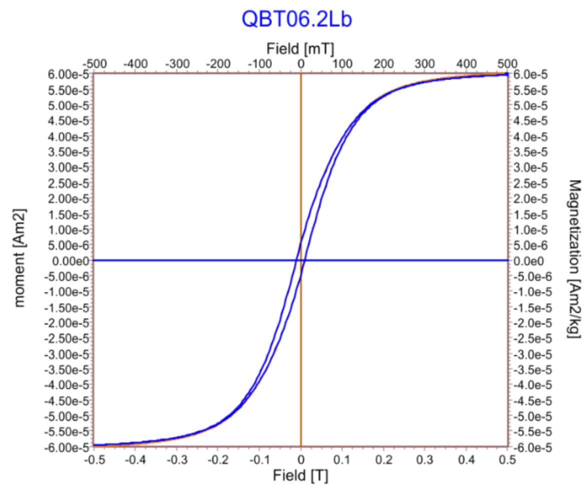
QBT06.2Lb
Field [mT]
moment [Am2]
Magnetization [Am2/kg]
Field [T]

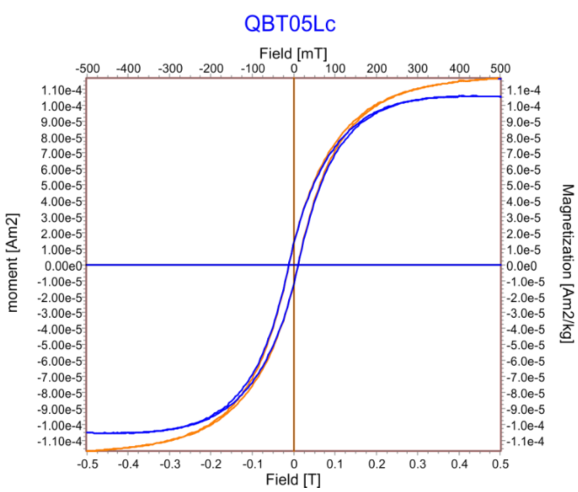
QBT05Lc
Field [mT]
moment [Am2]
Magnetization [Am2/kg]
Field [T]

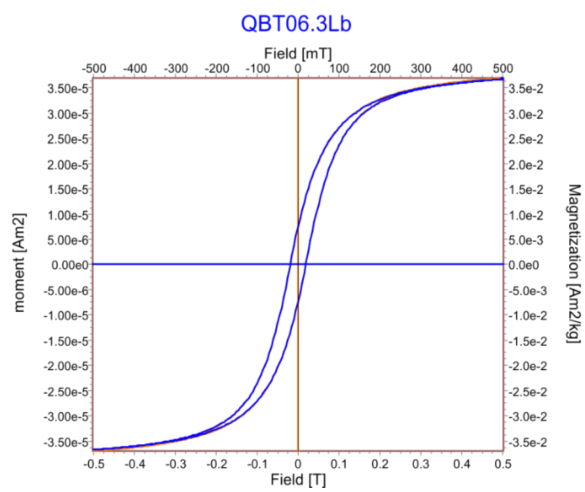
QBT06.3Lb
Field [mT]
moment [Am2]
Magnetization [Am2/kg]
Field [T]

QBT07Sb

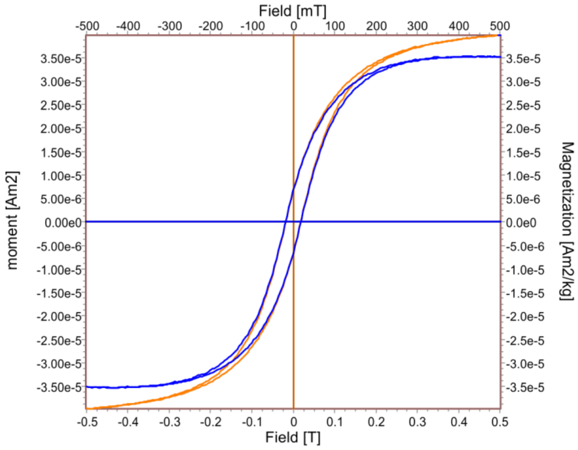

QBT08Ac

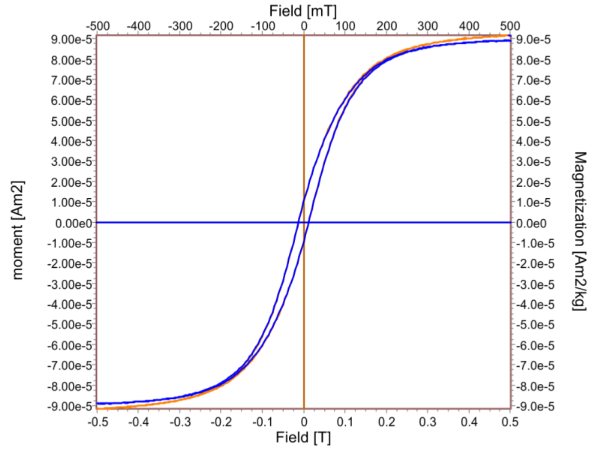

QBT07.2Sb

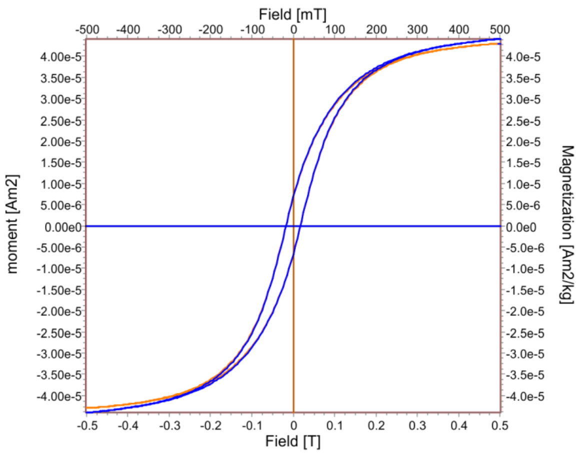

QBT08.2Ac

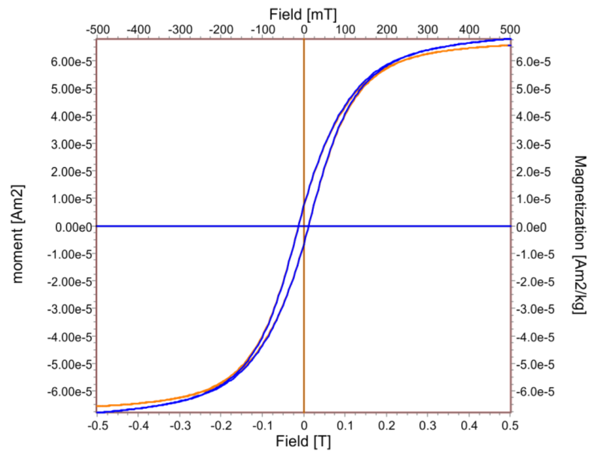

QBT07.3Sb

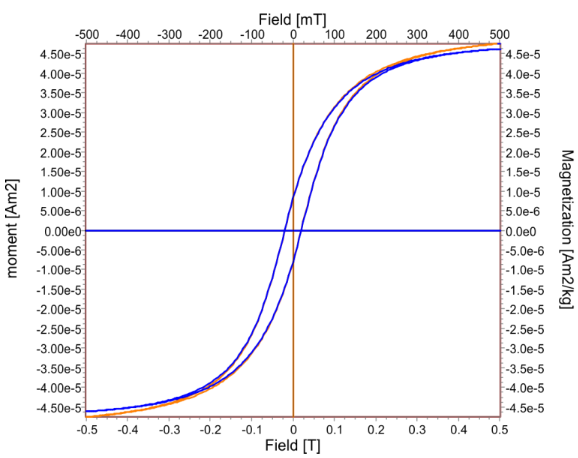

QBT08.3Ac

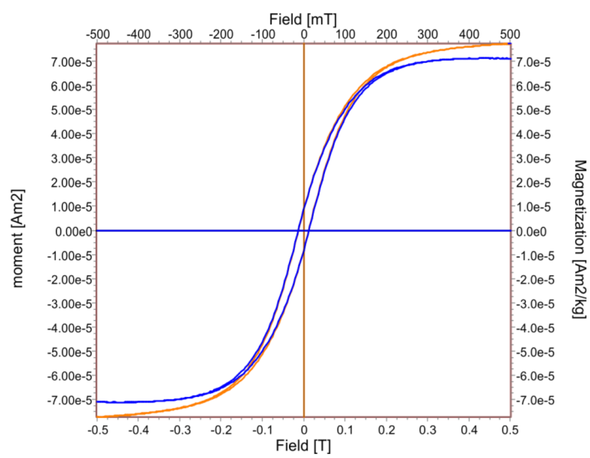

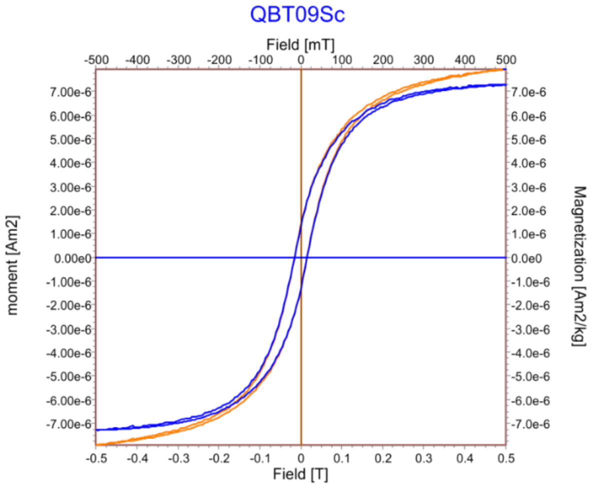
QBT09Sc
Field [mT]
moment [Am2]
Magnetization [Am2/kg]
Field [T]

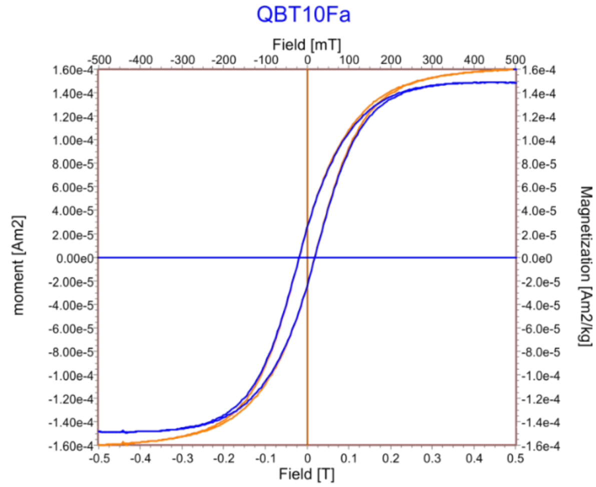
QBT10Fa
Field [mT]
moment [Am2]
Magnetization [Am2/kg]
Field [T]

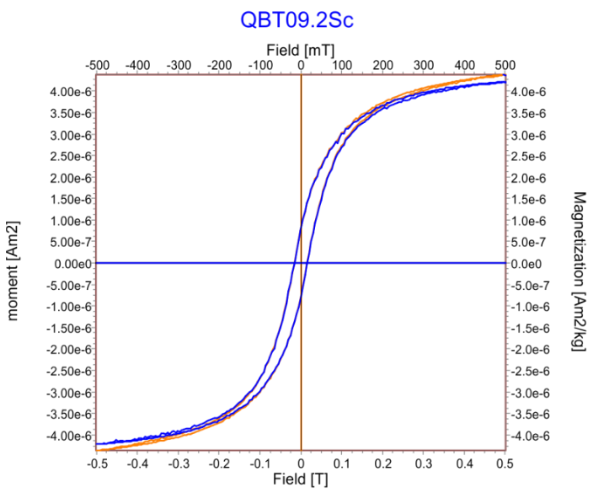
QBT09.2Sc
Field [mT]
moment [Am2]
Magnetization [Am2/kg]
Field [T]

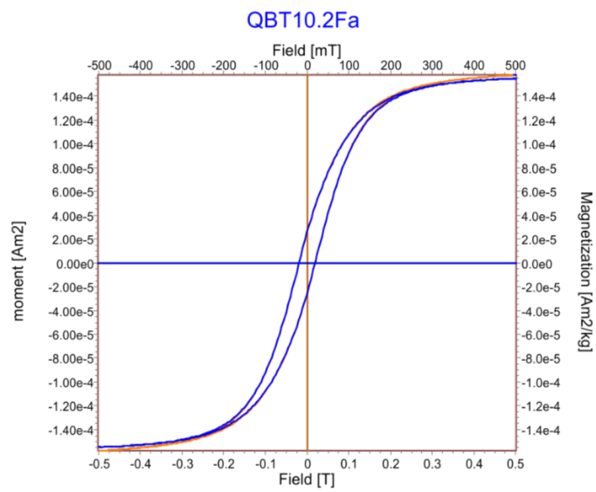
QBT10.2Fa
Field [mT]
moment [Am2]
Magnetization [Am2/kg]
Field [T]

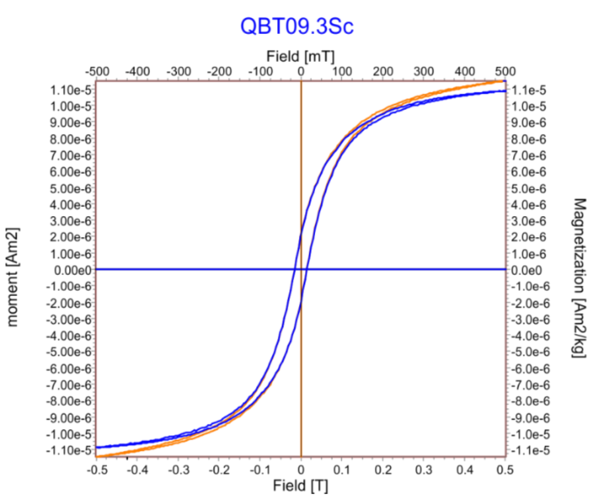
QBT09.3Sc
Field [mT]
moment [Am2]
Magnetization [Am2/kg]
Field [T]

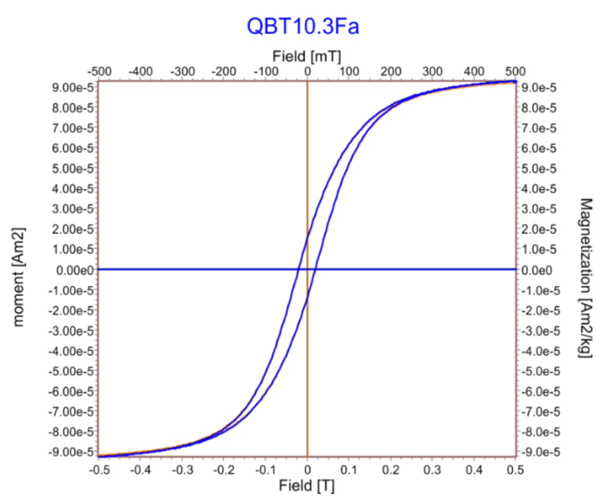
QBT10.3Fa
Field [mT]
moment [Am2]
Magnetization [Am2/kg]
Field [T]

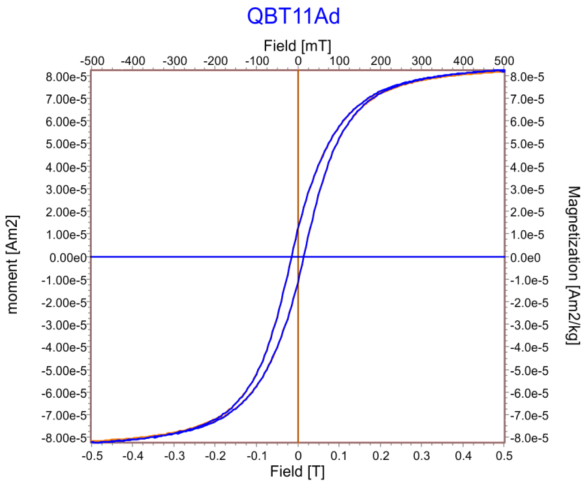
QBT11Ad
Field [mT]
moment [Am2]
Magnetization [Am2/kg]
Field [T]

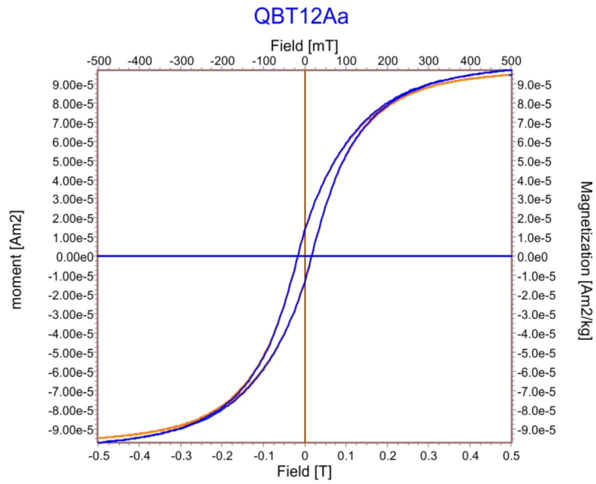
QBT12Aa
Field [mT]
moment [Am2]
Magnetization [Am2/kg]
Field [T]

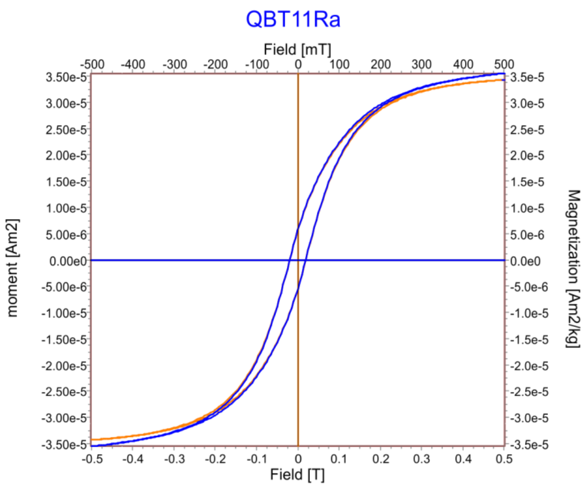
QBT11Ra
Field [mT]
moment [Am2]
Magnetization [Am2/kg]
Field [T]

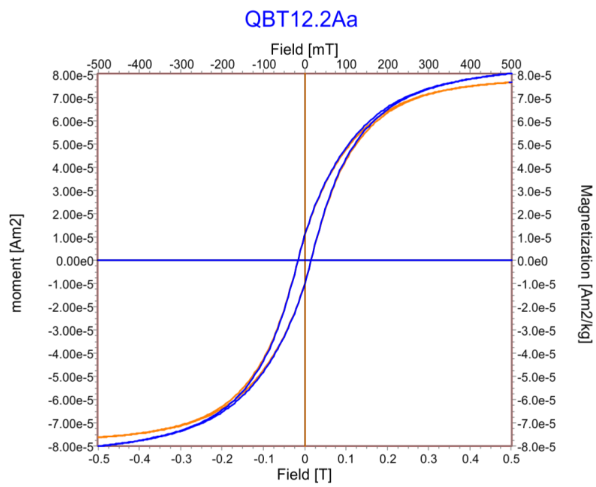
QBT12.2Aa
Field [mT]
moment [Am2]
Magnetization [Am2/kg]
Field [T]

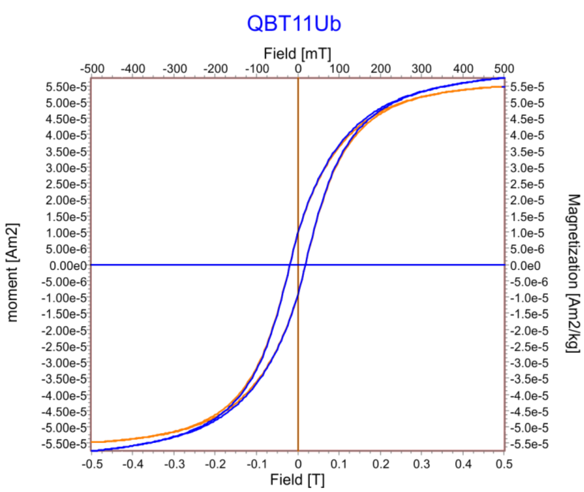
QBT11Ub
Field [mT]
moment [Am2]
Magnetization [Am2/kg]
Field [T]

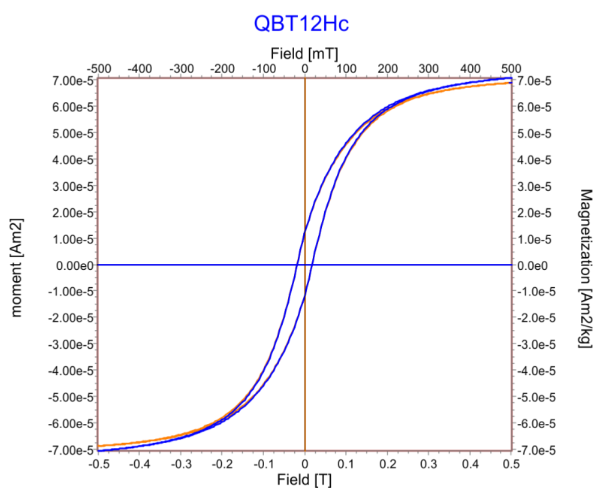
QBT12Hc
Field [mT]
moment [Am2]
Magnetization [Am2/kg]
Field [T]

QBT13Hc

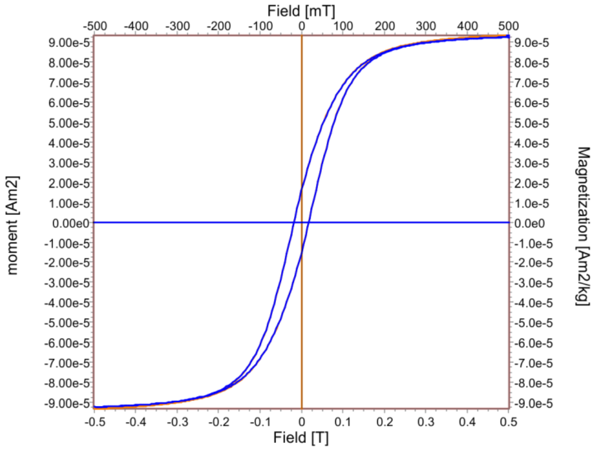

QBT14Fb

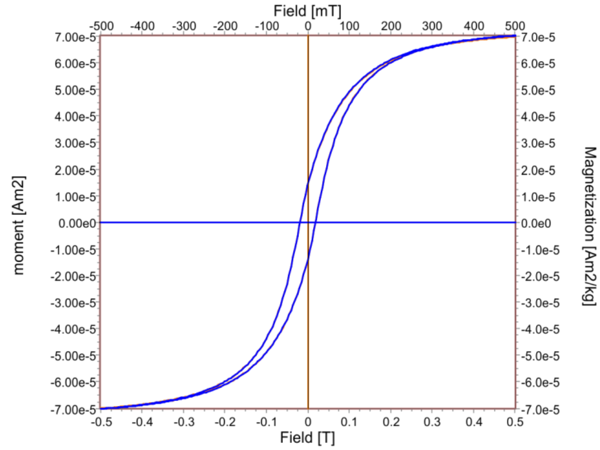

QBT13.2Hc

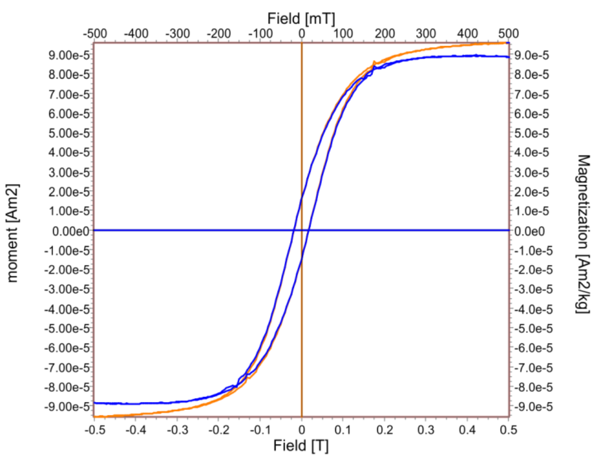

QBT15Ic

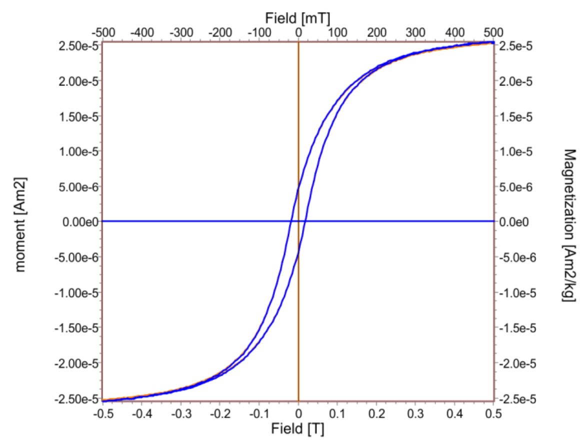

QBT13.3Hc

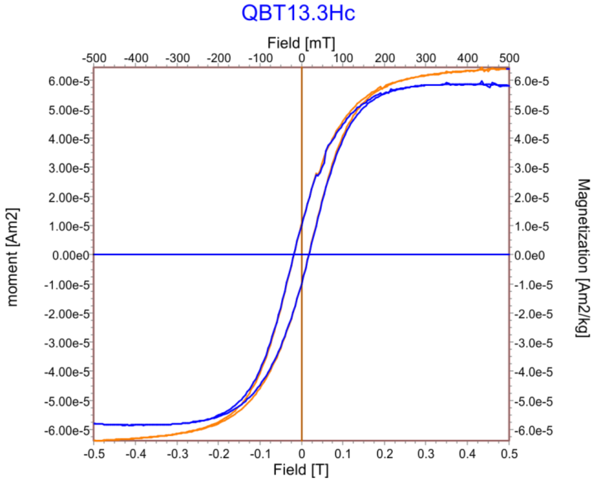

QBT16Fd

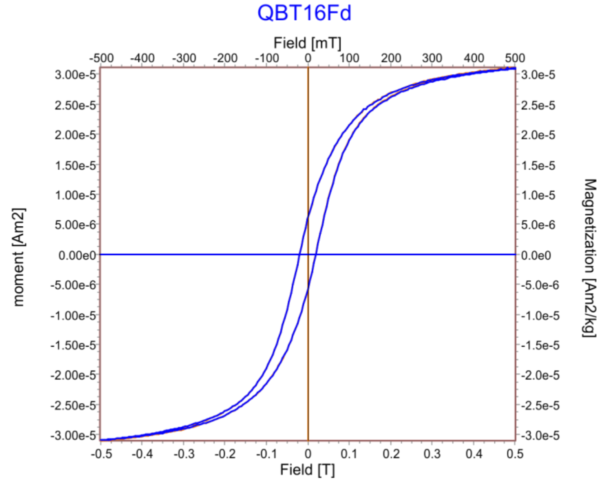

QBT17Jd

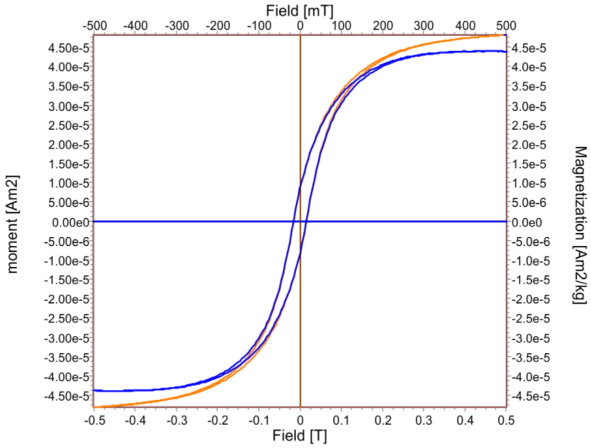

QBT18Bb

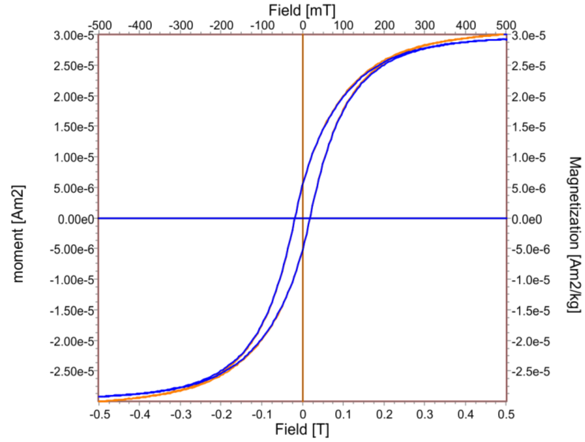

QBT17.2Jd

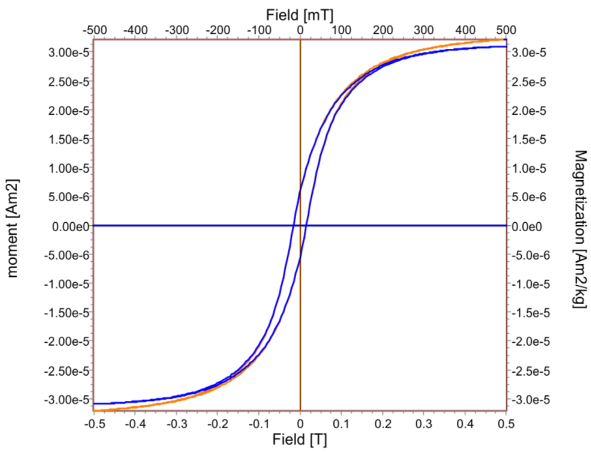

QBT18Pb

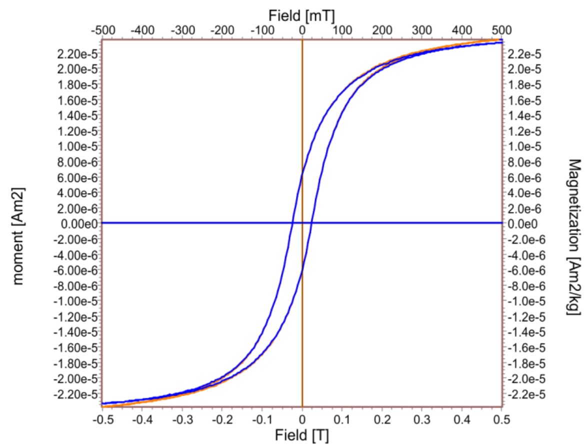

QBT17Ob

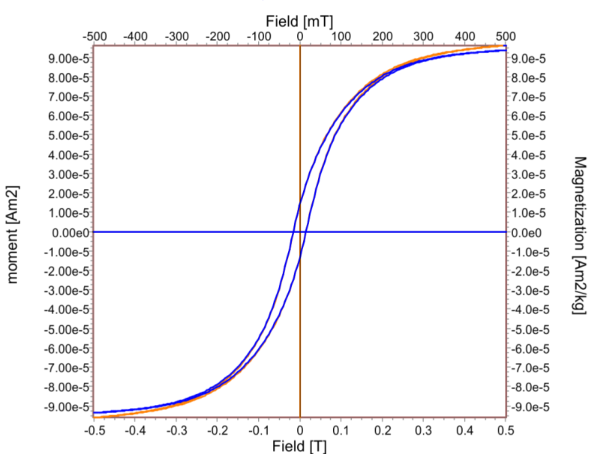

QBT18.2Pb

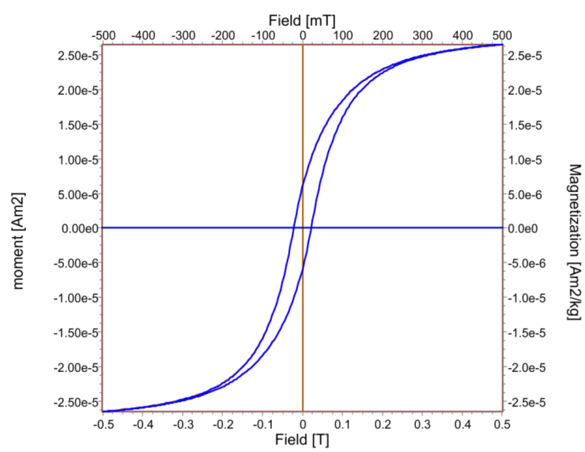

QBT19Jb

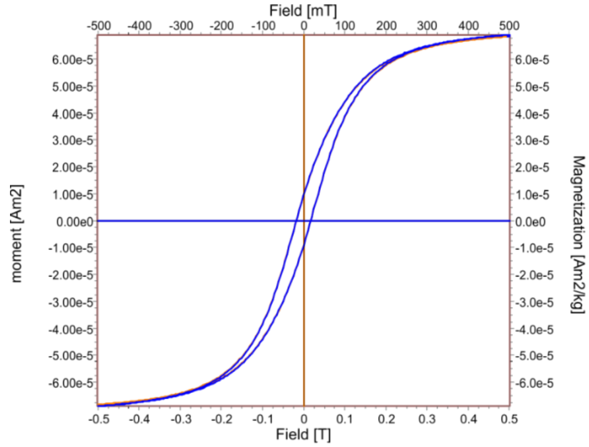

QBT20.1Fc

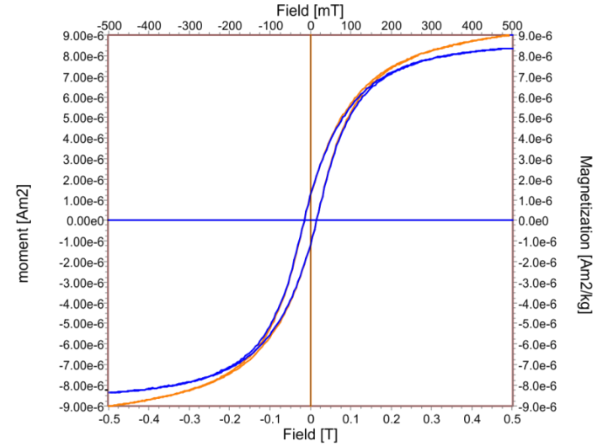

QBT19.2Jb

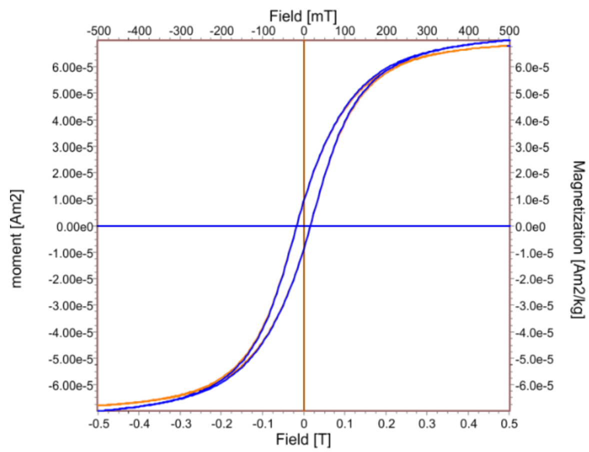

QBT20.1Id

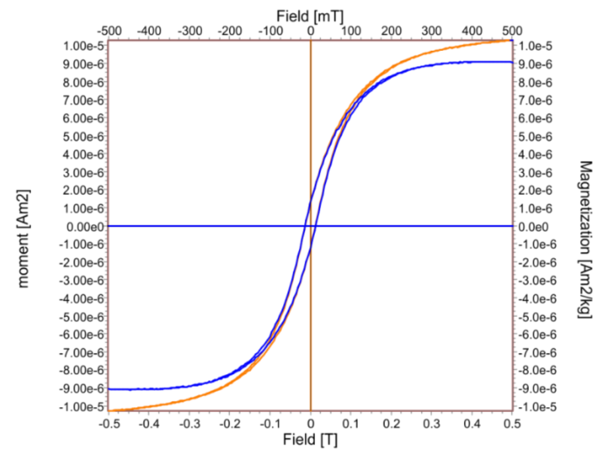

QBT19.3Jb

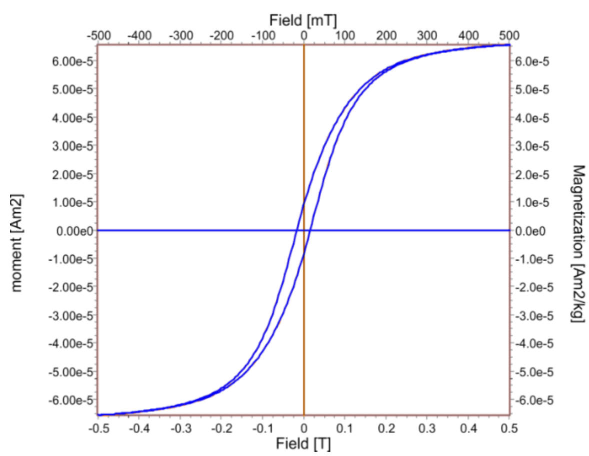

QBT20.1Nb

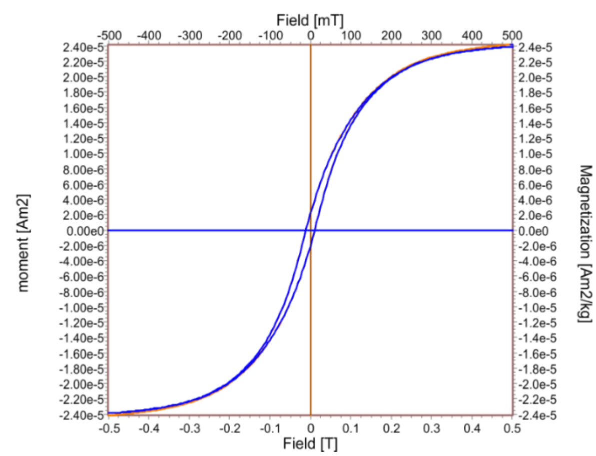

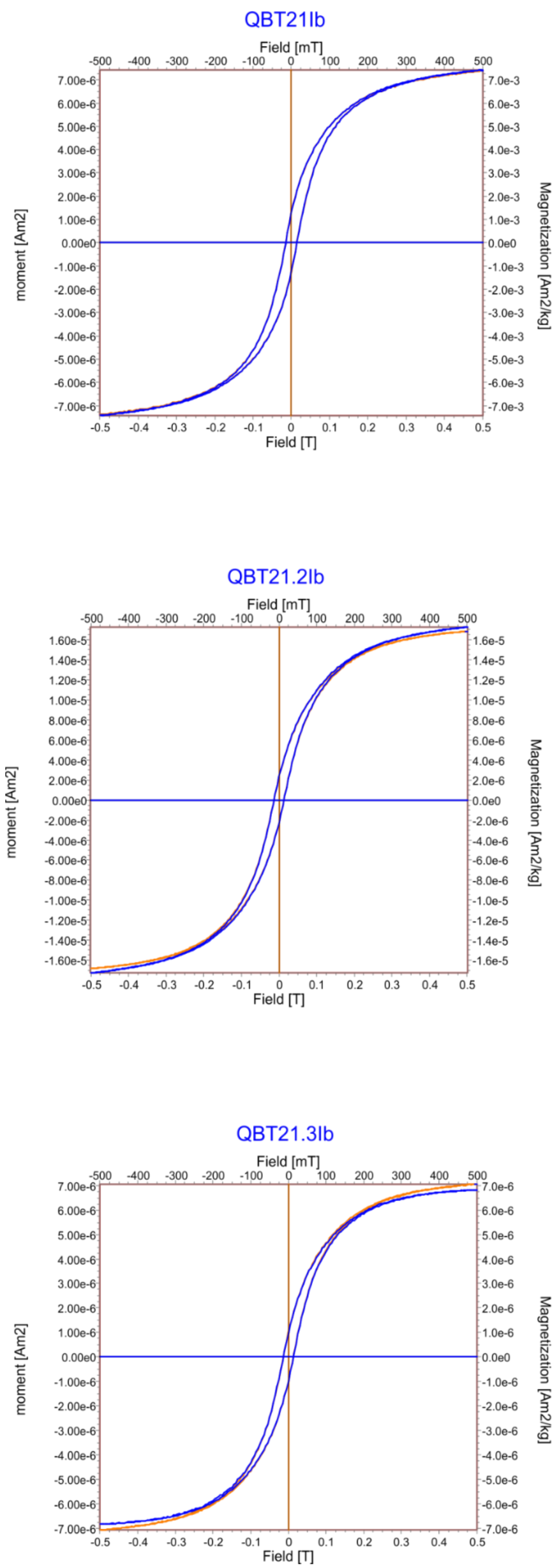

Figure 6.16. Hysteresis Curves for Bandelier Tuffs

6.2.4 First Order Reversal Curve (FORC) Diagrams

First-order reversal curves or FORCs are calculated from a series of partial hysteresis loops that begin by saturating a sample to a large field (H_{SAT}) and then decrease to the reversal field (H_a), where the FORC is defined as the magnetization curve that starts at the reversal field (C) and the applied field is increased back to saturation (H_b), (Roberts et al. 2000). The FORC curve is any point $M(H_a, H_b)$ starting at H_a moving back to positive saturation (Figure 5.2). FORCs can provide information that eliminates some ambiguity that is associated with hysteresis loops by determining distribution of switching fields and interaction fields between particles (Muxworthy and Roberts, 2007). Although hysteresis loops have been widely used for rock magnetic studies, there are several ambiguities associated with them that many authors aim to understand (Corradi and Wohlfarth 1978; Dunlop, 1981; Pike et al. 1999; Sprowl, 1990) such as mixing between magnetic components, mixtures of magnetic particles, grain size, internal stress, and magnetostatic interactions (Roberts et al., 2000; Muxworthy and Roberts, 2007). Roberts et al., 2000 describes differences between contouring patterns and domain wall curvature of SD, MD and PSD particles. Assemblages of interacting SD particles are represented on FORC diagrams by contours that close around a central peak near the Hu = 0 axis with varying distributions of the H_c values that represent different magnetic assemblage. Where MD particles are represented, the contour spread is characteristically increased in the vertical direction, symmetrically away from the origin at Hu = 0 and intersecting at $H_c = 0$, where the diverging contours typically extend beyond 30 mT on the H_c axis (Roberts 2000). While MD contours are symmetrical and divergent, the PSD signature display behavior similar to both SD and MD grains with closed peak and divergent contours (Muxworthy 2007). High-resolution FORC data collected for 21 sites from Bandelier Tuff samples show FORC distributions that are consistent with the characteristics of MD and PSD magnetic particle assemblages with a peak H_c values averaging approximately 20 mT (Figure 6.17), consistent with magnetite being the dominant carrier (Roberts 2000). Sites 6 and 8 exhibited lower coercivity values less than 20 mT (Figure 6.17). Sites 10 and 13 exhibit coercivity values that are higher which may be indicative of a mixing of PSD magnetite and another higher coercivity mineral such as maghemite.

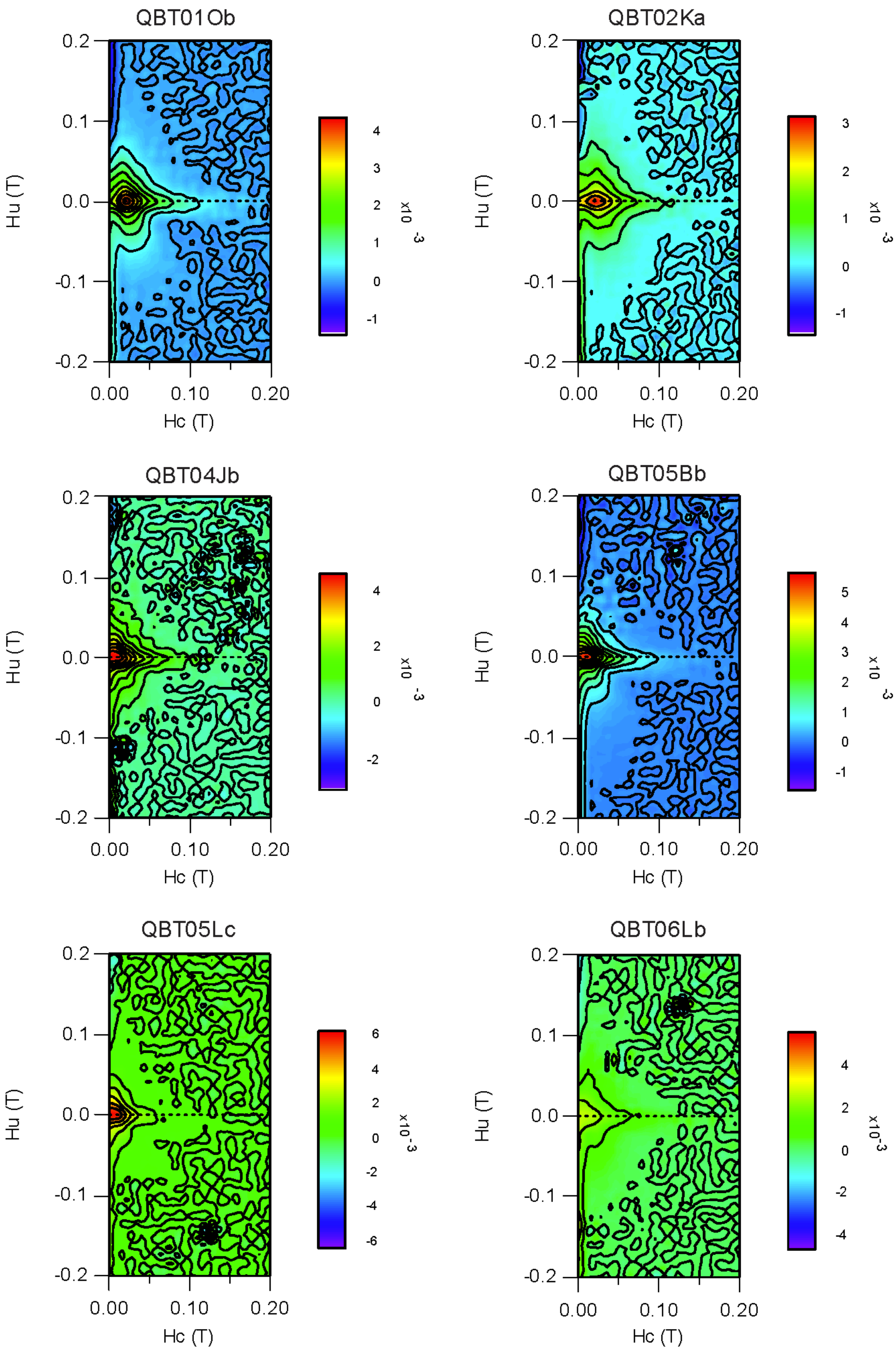
QBT01Ob
QBT02Ka
QBT04Jb
QBT05Bb
QBT05Lc
QBT06Lb
Hu (T)
Hc (T)
x10 -3

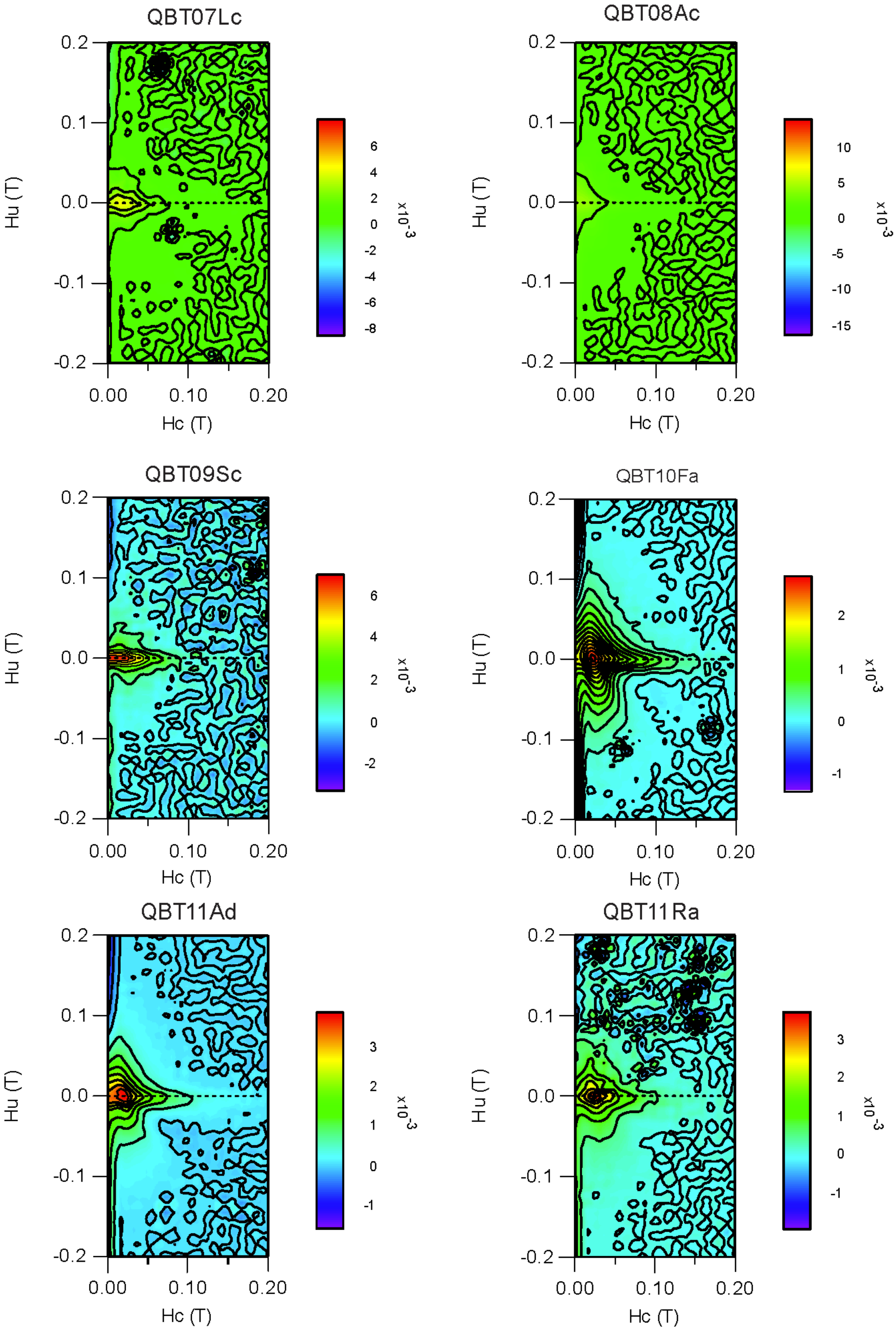
QBT07Lc
QBT08Ac
QBT09Sc
QBT10Fa
QBT11Ad
QBT11Ra
Hu (T)
Hc (T)
0.2
0.1
0.0
-0.1
-0.2
0.00
0.10
0.20
x10-3

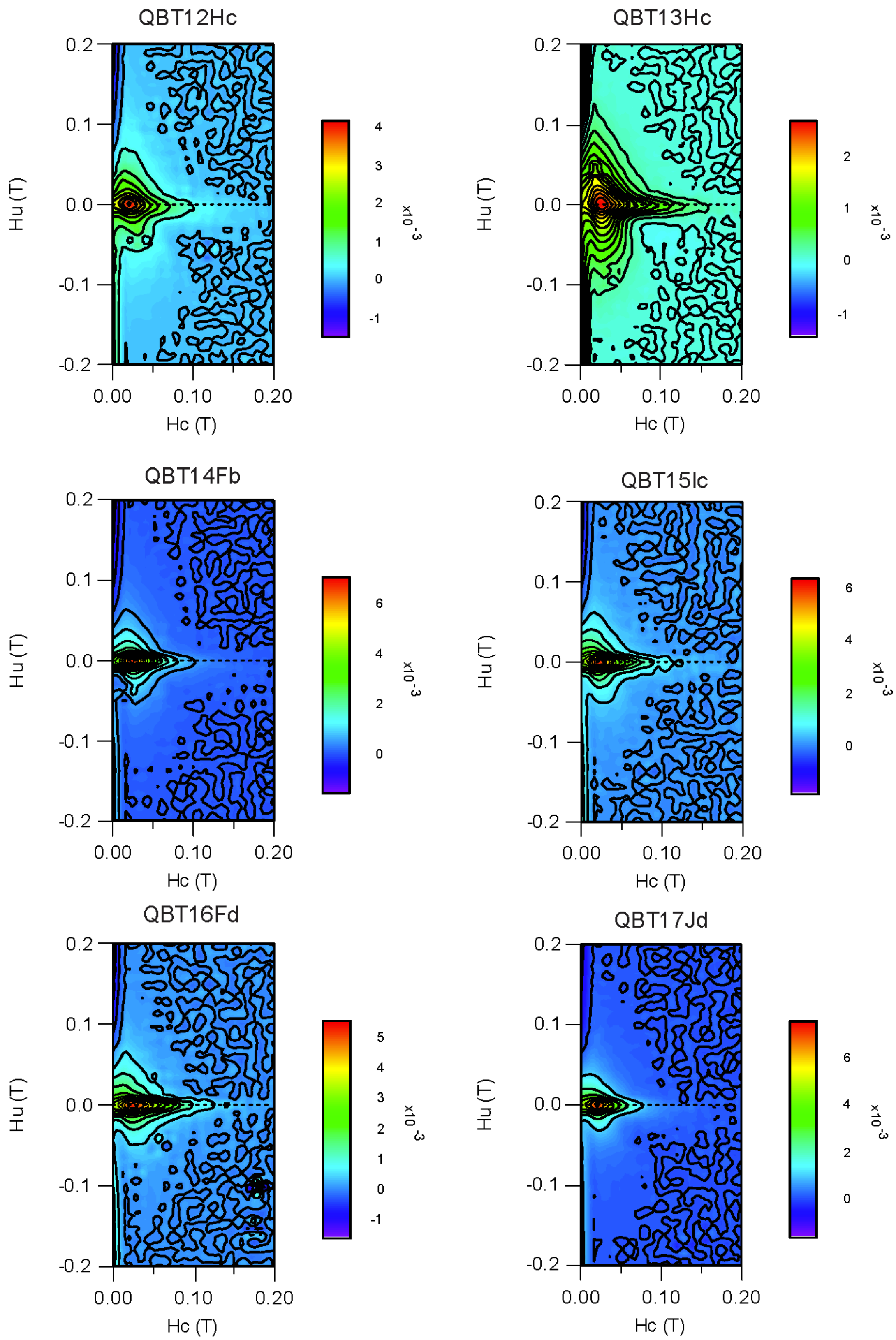
QBT12Hc
QBT13Hc
QBT14Fb
QBT15Ic
QBT16Fd
QBT17Jd
Hu (T)
Hc (T)
x10^-3
0.2
0.1
0.0
-0.1
-0.2
0.00
0.10
0.20

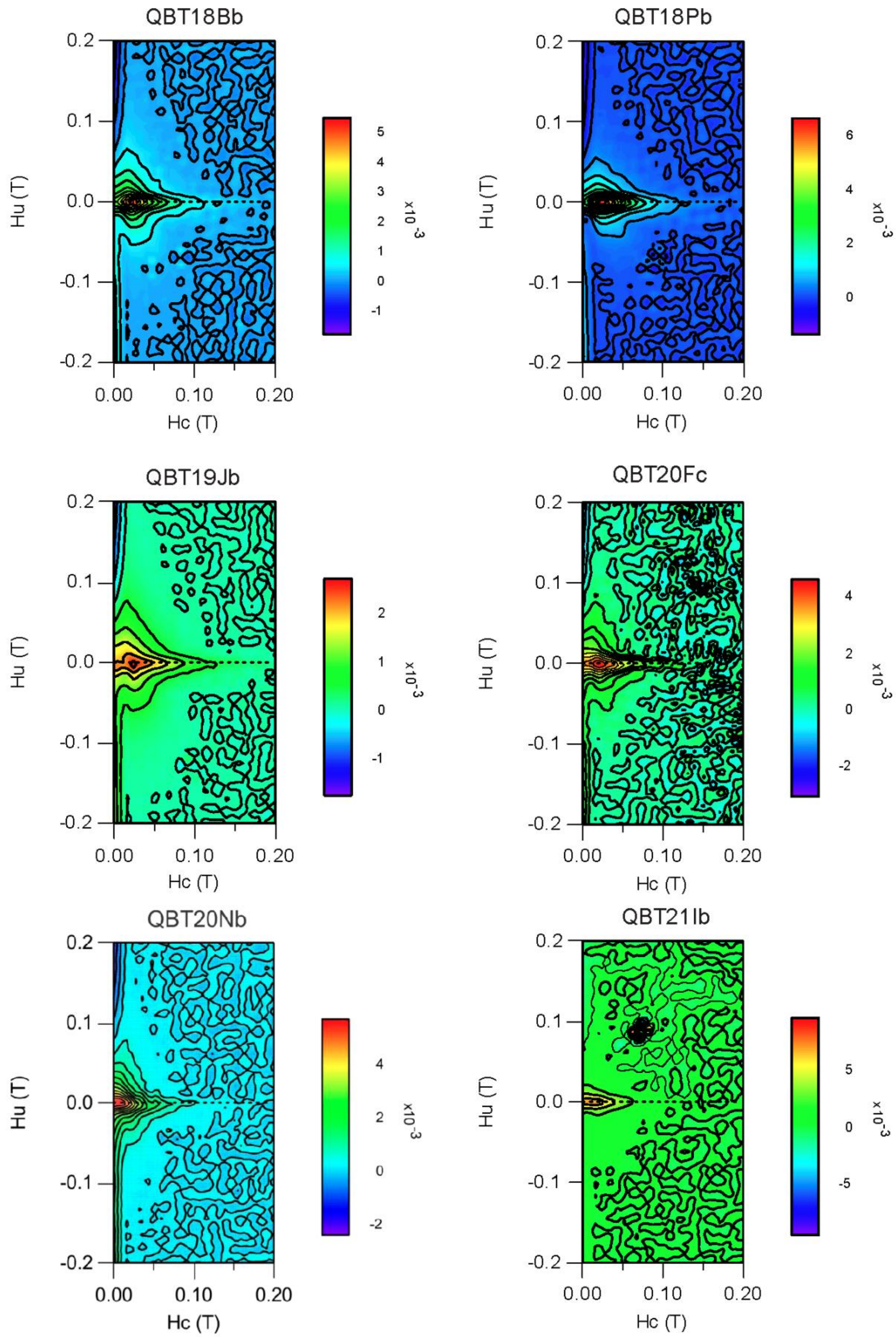

Figure 6.17. FORC Diagrams for Bandelier Tuffs

6.3 ARM Fabrics and Comparison of Anisotropy methods

Comparisons of AMS, AARM, and AIRM fabrics reveal differences in the dominant magnetic fabric at the sites in ignimbrites that originated from the same source caldera (i.e., Valles Caldera), have been extensively studied in the past, and have been demonstrated to show no statistically significant relative tectonic rotations over the area of interest (Sussman et al., 2011). The same methods were then used for a comparison of ignimbrites in a locality that has several sources of emplacement (i.e., Timber Mountain caldera, Stonewall Flat caldera, etc.) that have not been previously examined for rock magnetic properties, and have an extensive structural and tectonic history affecting the area.

Previous investigations that compare AMS and remanence fabrics have categorized at least four relationships between AMS and ARM fabrics (Jackson 1991; Rochette et al 1992 and 1999; Ferre 2002). The four relationships are normal (AMS and ARM have same principal axes), “inverse” (AMS has K1 and K3 reversed), “intermediate” (AMS has K1 and K2 reversed), and “oblique” (AMS has non-coaxial axes) (Figure 6.18). AARM is a technique that can isolate the contribution of specific mineral grains and can therefore help determine the observed relationships.

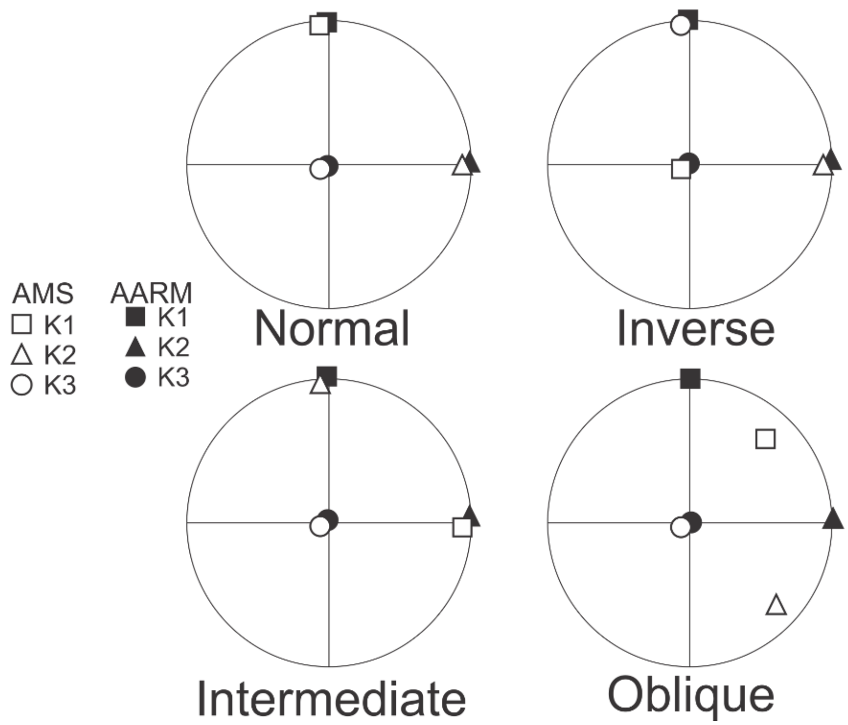

Figure 6.18. The four relationships between AARM and AMS

6.3.1 AIRM Results

AIRM fabrics for the four sites measured in the Bandelier tuff show well defined principal axes, with three of the four sites (5,11, and 18) having steeply inclined minimum susceptibility axes with a sub-horizontal K_1-K_2 foliation plane. However, site 20 yields an intermediate plunge of the minimum susceptibility axis (< 60°) and the K_1-K_2 plane dips > 30° (Figure 6.18). For each site, the percent anisotropy of the AIRM is much stronger than the percent anisotropy from the AMS data (Table 6.2). Three of the sites (5, 11, and 18) have normal fabrics, and site 20 has an inverse fabric, relative to the AMS fabrics. Two of the four sites (sites 11 and 18) have inferred transport directions that are approximately parallel to the expected direction (eastward) and sites 5 and 20 have inferred transport directions that are either in the opposite direction (site 5) or perpendicular (site 20) to the expected direction from the source Valles Caldera.

AIRM fabrics were measured on seven sites from the Gold Point collection; five of which are from Tuff of Stonewall Flat and two are from Tuff of Timber Mountain. The AIRM fabrics for six of the sites show well-defined principal axes, with steeply inclined minimum susceptibility axes that have a sub-horizontal K_1-K_2 foliation plane. The exception is site GP255, showing a very shallow (33°) plunge and a moderate dip of about 60°. Sites 202, 285, and 292 are normal to the AMS fabric, site 206 has an intermediate fabric compared to the AMS and, sites 201, 242, and 255 are oblique.

6.3.2 AARM Results

AARM data were collected for 17 of the 21 Bandelier Tuff sites. Fifteen sites have well defined principal susceptibility axes and two sites (sites 6 and 9) exhibit a high dispersion to the data such that the results from these sites are uninterpretable. Sites 6 and 9 also have shallow (<50°) plunges of 25.6° for site 6 and 45.7° for site 9 K_3 minimum susceptibility axes, with moderate to steep dips of 244.3 and 357.2 of the K_1 maximum susceptibility axes, respectively. Seven sites (sites 3, 7, 8, 10, 11, 13and 15) have moderate (50-70°) plunges of the K_3 minimum susceptibility axes with shallow to moderate dips of the K_1 maximum susceptibility axes, and eight sites (4, 5, 12, 14, 17, 18, 20, 21) have steep (>70°) plunges of the K_3 minimum susceptibility axes and thus a sub-horizontal K_1-K_2 foliation plane (Table 6.7). Seven of the Bandelier sites (sites 3, 4, 8, 11, 12, 14, and 18) yield a normal fabric, two sites (13 and 15) yield and intermediate fabric, eight sites (site 5, 6, 7, 9, 10, 17, 20, and 21) yield an oblique fabric, and no Bandelier sites yielded any inverse fabric relationship (Figure 6.19).

AARM fabrics were measured on all 14 Gold Point area ignimbrite study sites. Ten of the sites have well defined principal axes and four sites (GP 6, 206, 285, and 306) have a higher degree of scatter to the data. Seven sites (GP 6, 63, 206, 242, 255, 285, and 306) have shallow (<40°) plunges with moderate to steep dips. Five sites (48, 86, 201, 241, and 292) have steep (> 60°) plunges with a shallow to sub-horizontal K_1-K_2 foliation plane. Two sites (202 and 219) have moderate (~56°) plunges and a moderately dipping K_1-K_2 foliation plane (Table 6.7). The Tuffs of Timber Mountain AARM data show one site with a normal fabric to the AMS data (GP 48), one an inverse fabric (GP 306), two intermediate fabrics (GP 86 and 285), and two of oblique fabrics (GP 219 and 255. Data from the Stonewall Flat Tuff sites show five sites with an oblique fabric (GP 201, 202, 206, 241, and 242) and one normal of normal fabric (GP 292). The Tuff of Oriental Wash sites (GP 6 and 63) both display an oblique fabric.

Table 6.7. Summary of AARM data for Bandelier Tuff and Gold Point area sites.

Bandelier Tuff AARM

Site	Unit	N	K_1	K_2	K_3	K_1 Dec	K_1 Inc	K_1 Dec C	K_1 Inc C	K_2 Dec	K_2 Inc	K_2 Dec C	K_2 Inc C	K_3 Dec	K_3 Inc	K_3 Dec C	K_3 Inc C	L	F	P
QBT03	3/4	10	1.096	1.011	0.893	252.2	18.80	3.42	7.77	153.60	23.60	6.40	13.59	16.90	59.10	4.10	13.91	1.085	1.132	1.228
QBT04	4	10	1.043	1.009	0.949	232.4	8.70	2.00	9.39	323.10	4.40	2.90	9.39	79.70	80.20	1.40	3.27	1.034	1.063	1.099
QBT05	3/4	10	1.035	1.029	0.936	316.3	9.10	2.16	29.24	46.80	3.30	3.50	29.31	156.60	80.30	2.30	4.29	1.006	1.099	1.106
QBT06	2	10	1.026	1.003	0.971	244.3	12.80	7.72	25.04	358.50	60.90	10.00	35.32	148.00	25.60	6.30	30.93	1.023	1.033	1.057
QBT07	1/2	10	1.035	1.011	0.954	99.8	9.00	6.67	12.03	6.60	19.60	5.80	11.65	213.30	68.30	4.60	8.21	1.024	1.059	1.085
QBT08	2	10	1.036	1.023	0.941	123.1	8.90	4.13	28.27	219.30	34.60	4.50	28.75	20.80	53.90	3.20	8.53	1.014	1.087	1.101
QBT09	2	10	1.031	1.009	0.961	357.2	33.00	7.56	26.46	248.80	26.00	16.20	24.94	128.80	45.70	10.70	20.70	1.022	1.050	1.073
QBT10	3t	10	1.033	1.001	0.966	82.3	3.80	5.02	10.23	350.10	31.10	9.30	30.57	178.60	58.60	6.40	30.59	1.031	1.037	1.069
QBT11	3t	13	1.054	1.003	0.943	343.7	3.20	3.82	5.46	75.40	28.20	5.00	9.75	247.60	61.50	1.10	10.45	1.050	1.064	1.118
QBT12	3t	10	1.045	1.010	0.944	351.2	5.30	4.86	9.73	260.20	11.30	4.00	8.22	105.90	77.50	4.50	7.76	1.034	1.070	1.107
QBT13	4	10	1.035	1.009	0.956	189.4	0.30	4.71	19.60	99.20	54.30	2.90	6.73	279.80	54.30	2.90	6.73	1.027	1.055	1.083
QBT14	4	10	1.050	1.026	0.924	319.3	6.00	1.66	9.80	229.20	0.20	3.00	9.81	137.20	84.00	1.60	3.04	1.024	1.110	1.136
QBT15	3	10	1.042	0.993	0.966	271.9	6.80	1.68	17.77	6.30	32.50	4.00	38.07	171.50	56.60	2.60	34.95	1.050	1.028	1.079
QBT17	3/4	10	1.040	1.019	0.941	67.1	1.80	3.88	14.42	157.40	7.10	7.00	14.91	322.80	82.70	1.80	10.17	1.021	1.083	1.106
QBT18	3/4	10	1.033	1.008	0.959	303.7	7.60	5.27	7.66	35.30	12.10	3.00	7.74	182.40	75.60	3.20	5.31	1.025	1.050	1.077
QBT20	4	13	1.039	1.015	0.946	293	0.10	2.05	6.66	203.00	7.30	2.20	6.68	23.50	82.70	2.00	2.50	1.023	1.073	1.098
QBT21	4	10	1.020	0.999	0.981	68.6	8.50	5.97	7.81	336.80	12.00	6.20	13.76	192.90	75.20	4.80	13.65	1.022	1.018	1.040

Gold Point Tuffs AARM

Site	Unit	N	K_1	K_2	K_3	K_1 Dec	K_1 Inc	K_1 Dec C	K_1 Inc C	K_2 Dec	K_2 Inc	K_2 Dec C	K_2 Inc C	K_3 Dec	K_3 Inc	K_3 Dec C	K_3 Inc C	L	F	P
GP06	OW	7	1.055	1.006	0.939	181.1	2.1	7.39	13.07	88.2	53.8	9.5	45.45	272.6	36.1	6.7	44.98	1.049	1.071	1.124
GP48	TM	10	1.048	1.011	0.941	157.1	1.7	2.41	12.79	66.7	13.3	4.9	12.81	254.2	76.5	2.3	5	1.037	1.074	1.113
GP63	OW	9	1.082	0.105	0.872	132.8	54.8	3.18	9.37	290.9	33.2	4.4	9.51	27.8	10.3	3.2	4.73	1.033	1.201	1.241
GP86	TM	9	1.277	1.153	0.570	29.8	19.6	0.74	9.26	298.4	4.1	3.8	9.69	196.9	69.9	0.7	4.8	1.108	2.022	2.241
GP201	SF	9	1.030	1.001	0.969	266.2	12.4	6.25	14.14	174.5	7.6	11.9	14.48	53.6	75.4	4.8	12.6	1.029	1.032	1.062
GP202	SF	10	1.151	1.099	0.751	325.5	26.7	0.88	29.32	225.8	18.5	0.7	29.31	105.2	56.6	0.7	1.36	1.047	1.464	1.533
GP206	SF	9	1.046	1.021	0.933	47.8	46.3	5.94	33.77	275.0	33.0	13.9	34.63	167.3	25.1	6.3	16.59	1.024	1.095	1.122
GP219	TM	9	1.019	1.013	0.968	229.7	30.6	11.03	58.02	326.8	11.8	10.4	57.77	75.4	56.8	5.2	21.27	1.006	1.046	1.053
GP241	SF	10	1.039	1.024	0.937	238.1	0.4	4.06	31.57	147.9	25.7	7.8	31.63	328.9	64.3	4.1	8.04	1.014	1.093	1.108
GP242	SF	9	1.074	1.019	0.907	13.5	55.1	3.62	17.31	109.9	4.4	8	17.32	203.0	34.5	3.8	8.38	1.054	1.125	1.185
GP255	TM	10	1.122	1.038	0.839	194.7	11.3	1.73	6.45	345.3	77.1	5.8	6.22	103.4	6.1	2.8	6.02	1.081	1.237	1.337
GP285	TM	8	1.009	0.998	0.993	241.4	40.7	16.81	38.1	128.9	24.0	11.8	69.41	17.2	39.8	16.3	59.98	1.012	1.005	1.017
GP292	SF	10	1.025	1.015	0.961	291.5	9.5	1.66	14.4	201.3	1.1	3.4	14.49	104.5	80.4	2	3.98	1.010	1.056	1.066
GP306	TM	9	1.013	0.996	0.990	205.4	72.7	17.07	29.06	335.6	11.4	25.9	62.79	68.3	12.8	18.5	61.81	1.017	1.006	1.023

Bandelier Tuff AARM Data

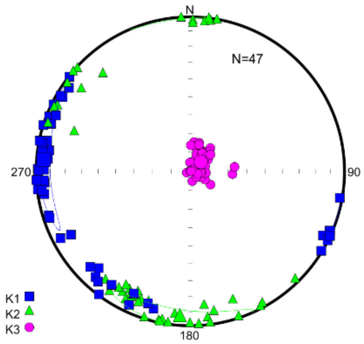

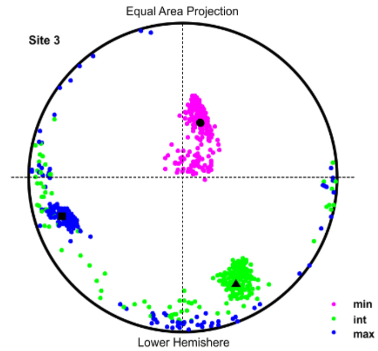

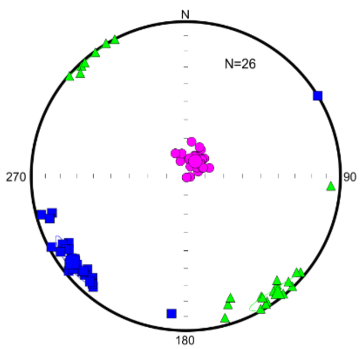

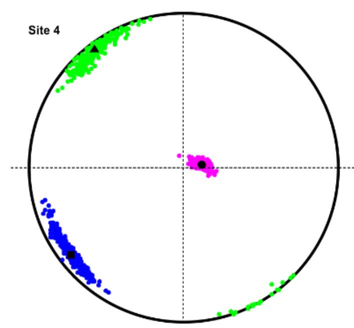

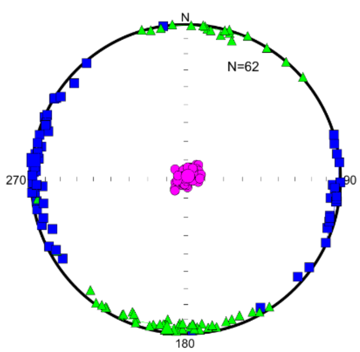

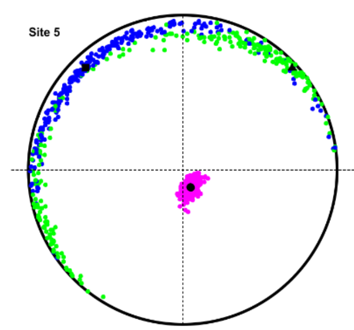

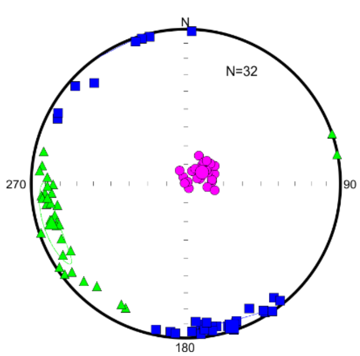

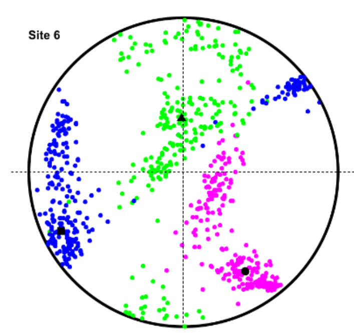

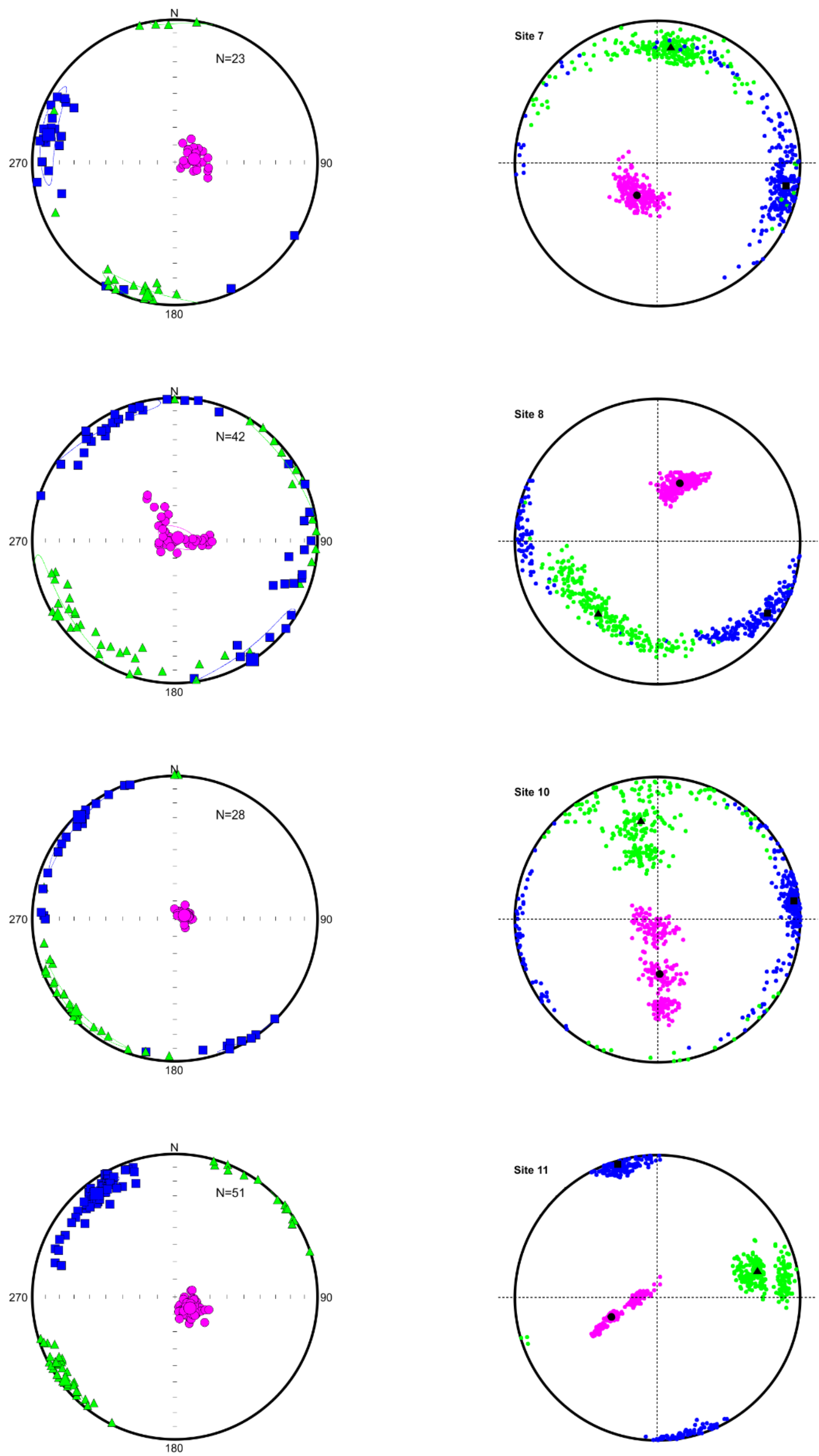
N
N=23
270
90
180
Site 7
N
N=42
270
90
180
Site 8
N
N=28
270
90
180
Site 10
N
N=51
270
90
180
Site 11

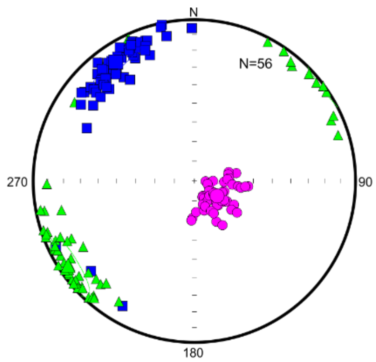
N
N=56
270
90
180

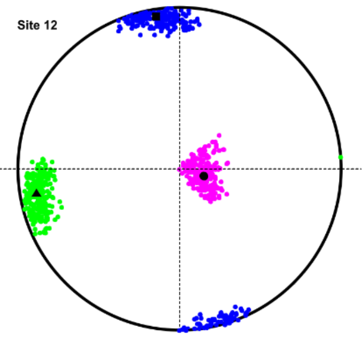
Site 12

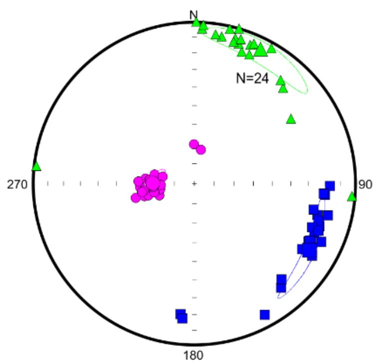
N
N=24
270
90
180

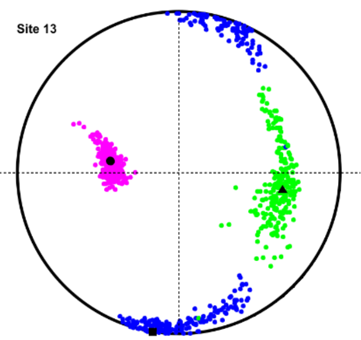
Site 13

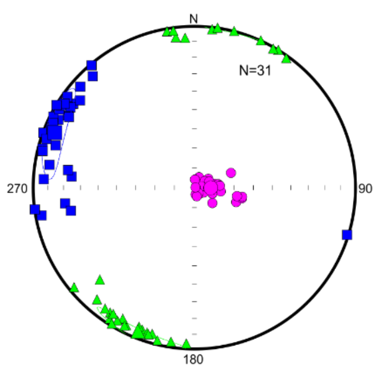
N
N=31
270
90
180

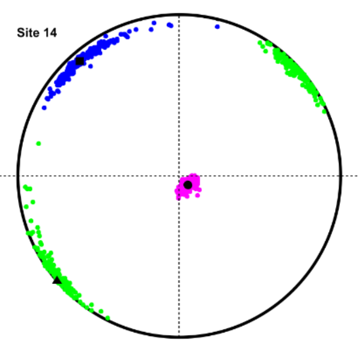
Site 14

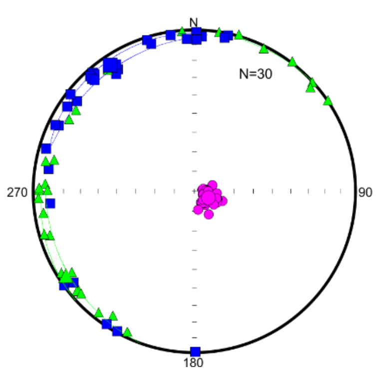
N
N=30
270
90
180

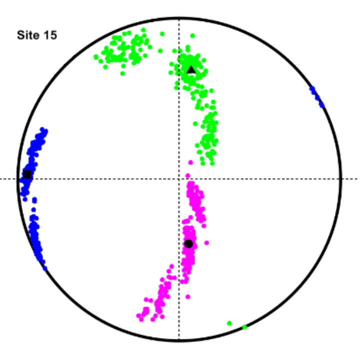
Site 15

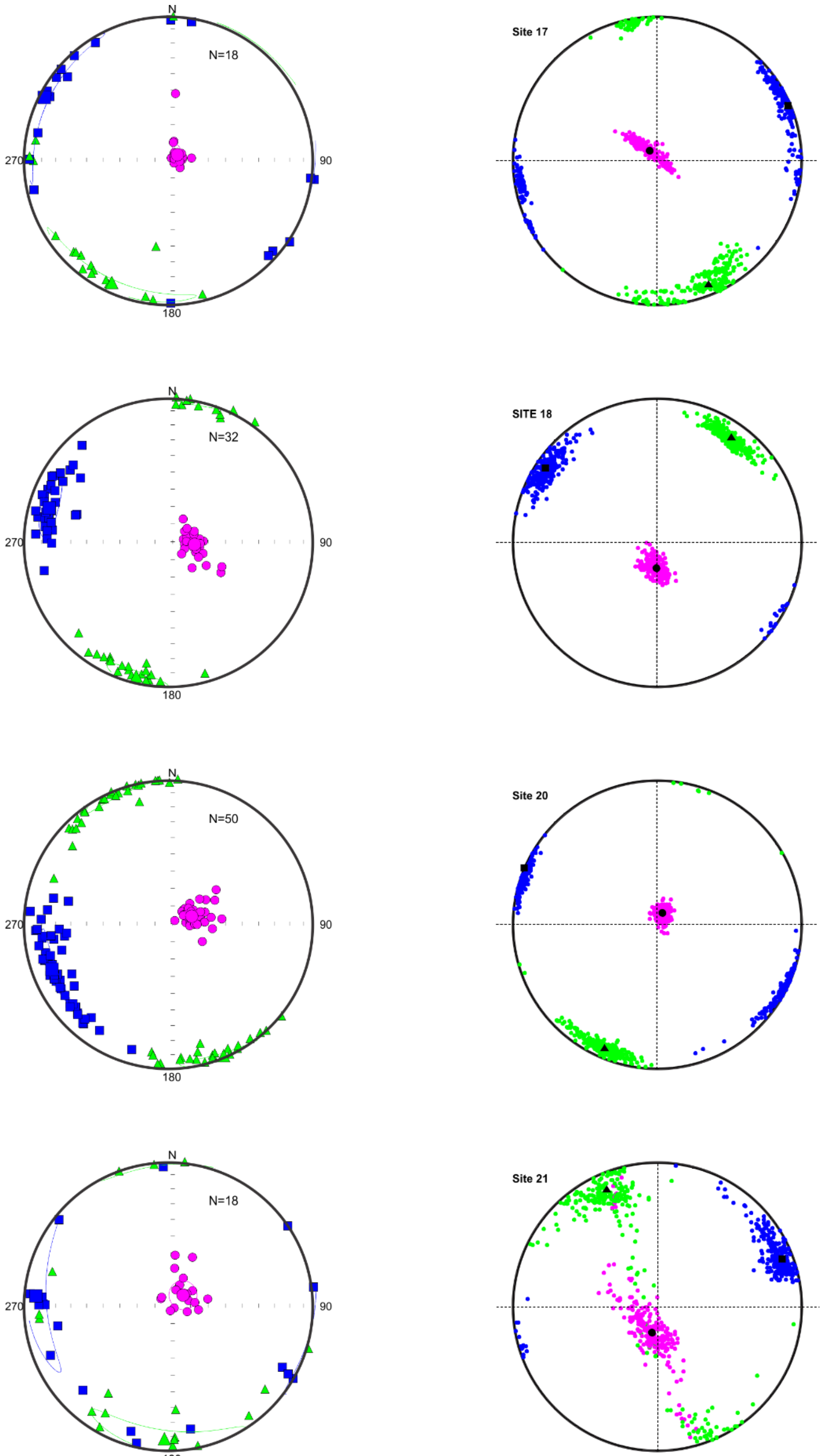
N
N=18
270
90
180
Site 17
N
N=32
270
90
180
SITE 18
N
N=50
270
90
180
Site 20
N
N=18
270
90
180
Site 21

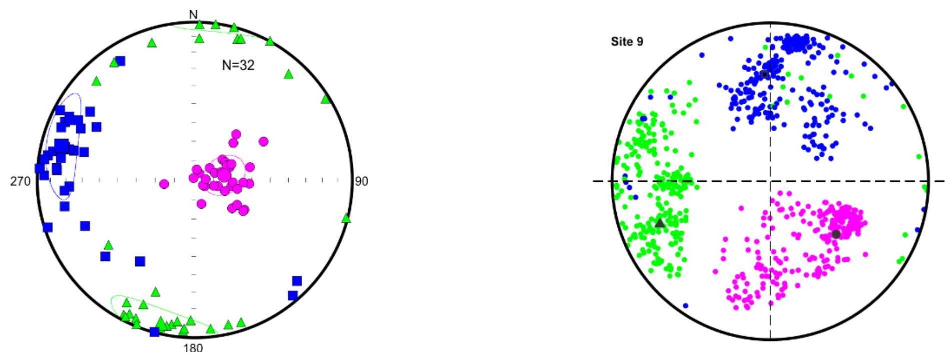

Figure 6.19. Comparison of AMS vs AARM data for Bandelier Tuff sites.

CHAPTER 7

DISCUSSION

Two regionally extensive ignimbrites, from the Valles Caldera, Jemez Mountains, New Mexico and from the Southwest Nevada Volcanic Field (SWNVF) were examined in this study. Both sets of data yield well-defined AMS data. The magnetic mineralogy is dominated by pseudo-single domain and multi-domain magnetite. The cross-plots of the AMS P values (percent anisotropy) versus the ARM P values for both study areas show overall higher anisotropy values for the AARM than the AIRM (Figure 7.3), and the cross-plot for magnetic lineation versus magnetic foliation of AMS to ARM methods shows higher values along the foliation for ARM than AMS indicating an oblate fabrics (Figure 7.4). The method of using the K_1 axis as an indicator to define paleo-flow of ignimbrites may have worked for many authors (Ellwood, 1982, Lipman et al., 1996), in this study we chose to compare that method with using the K_3 axis as the indicator defining the paleo-flow as it is presumed that the K_3 aligns with the imbrication direction, and thus the inferred transport direction. For the Bandelier Tuff AMS, using the K_1 axis as the indicator for inferred transport direction, 15 out of 21 (71%) sites show an inferred transport direction away from the Valles Caldera to the ENE-ESE (Figure 6.5). Compared with using the K_3 axis 18 out of 21 (86%) show an inferred transport direction to the ENE-ESE (Figure 6.6), clearly, in this case the K3 is a better indicator of paleo-flow direction.

Interpreting the Gold Point area data set is not as straightforward as the Bandelier Tuff data set. Other factors needed to be considered. The area sampled lies between Slate Ridge, Gold Mountain and other features that could alter the inferred transport direction locally due to the paleo-topography high relief. All Gold Point area AMS and ARM measurements were structurally corrected to the paleo-horizontal that were measured at each site. Additionally because these specimens were collected in the Walker Lane transfer system in SW Nevada, major displacement or vertical axis rotations may be related sources of error seen within the dataset. Of the six Timber Mountain sites only three (GP 48, 255, and 306) show an inferred transport direction that corresponds to their source caldera. The other three sites show an inferred transport direction that are in the opposite (GP 86 and 219) direction or perpendicular (GP 285) to the source. Of the six Stonewall Flat tuffs only two (GP 241 and 242) show an inferred transport direction that corresponds to their source caldera, the other four sites show directions that are either in the opposite (GP 201, 202, 206) direction or perpendicular (GP 292) to the source. In addition, the Oriental Wash Tuffs, which have no known source show, inferred transport directions that are perpendicular to each other (Figure 6.8).

7.1 Comparison of AMS/AIRM/AARM Fabrics

An in depth look at the comparison of AMS to ARM methods was done by looking at sites across the study areas from both localities in New Mexico and in Nevada. There were four total sites that had complete AMS and AMR measurements completed on them (Figure 7.1), and seven total sites for the Gold Point area Tuffs (Figure 7.7).

Sites 5, 11, 18, and 20 were compared for the Bandelier Tuff ignimbrites for their spacing through the sampling area and because these sites were strategically sampled in a vertical array from the lowest point to the highest point in the outcrop. All of these sites have a very steep plunge and sub-horizontal dips for the AMS and the AARM (Figure 7.1). The AIRM data look similar with the exception of site 20 AIRM showing a moderate plunge and dip. Site 5 AMS and AARM are both indicating an inferred transport direction to the ESE when looking at the K_1 axes in both stereographic projections, however the K_3 imbrication orientation is showing an inferred transport direction to the northeast. The AIRM for site 5 is sowing an inferred transport direction that is opposite to the AMS for both the K_1 and K_3 axes (Figure 7.2). Site 11, K_1 and K_3 axes inferred transport directions for AMS, AARM and AIRM are all to the ESE with the exception of the K_3 imbrication direction which shows an inferred transport direction to the southwest. Site 18, K_1 and K_3 axes inferred transport directions for AMS, AARM and AIRM are all to the ESE with the exception of the K_3 imbrication direction which shows an inferred transport direction to the south. Site 20 shows the most variability, K_1 axes AMS are to the northeast, for AIRM to the southwest, and for AARM southeast. K_3 axes for AMS and AARM are to the northeast and for AIRM to the southeast (Figure 7.2). Both ARM methods show higher values for magnetic foliation than the magnetic lineation for the four sites when compared to AMS (Figure 7.5)

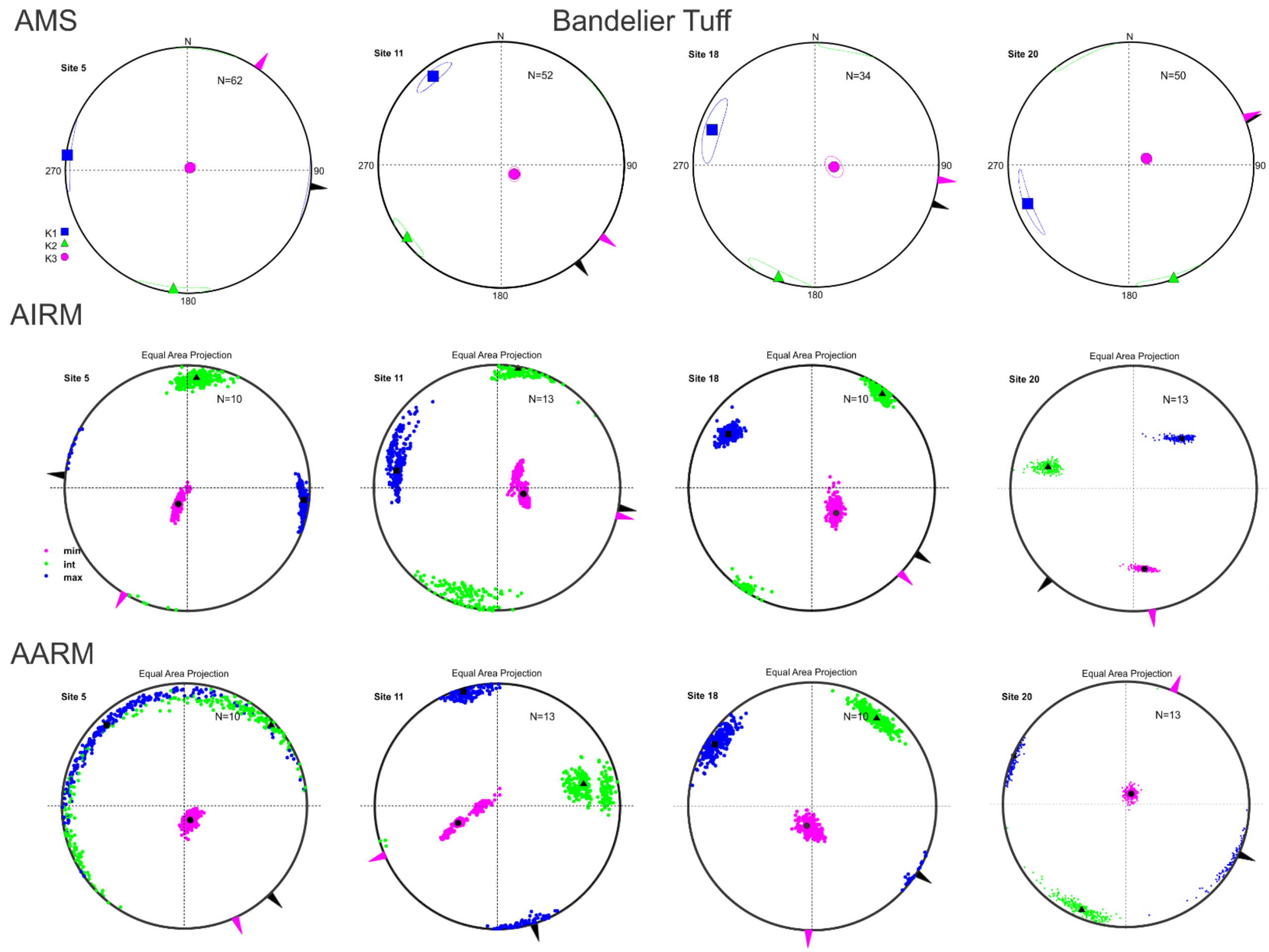

Figure 7.1. Comparison of AMS, AIRM, and AARM data with black arrows indicating K1 transport directions and pink arrows indicating K3 imbrication orientation. AIRM and AARM represented by the bootstrap method of Constable and Tauxe 1990.

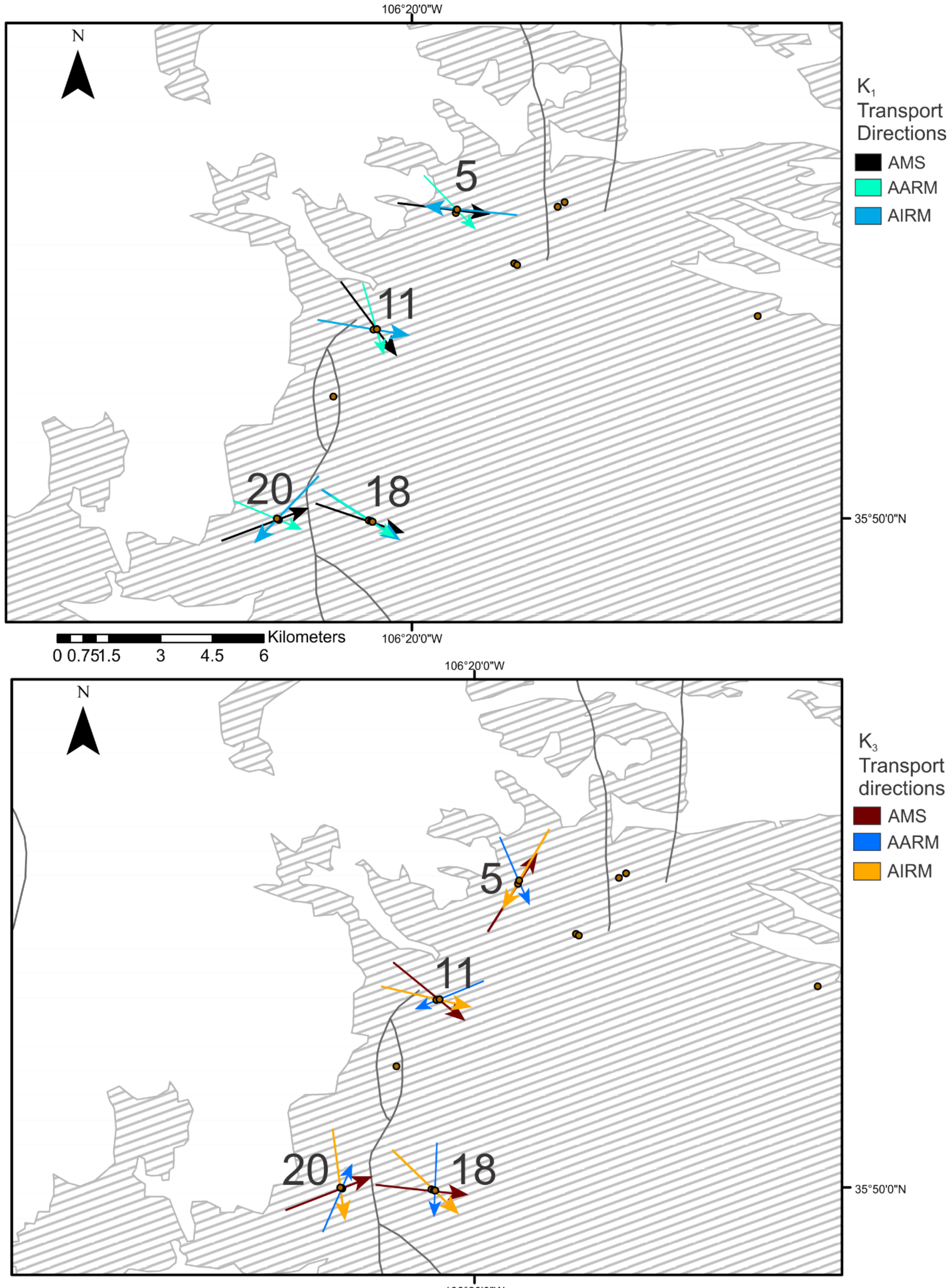

Figure 7.2. TOP- Comparison of AMS, AIRM, and AARM data showing K_1 transport directions and **BOTTOM-** Imbrications direction of the K_3 axes.

Table 7.1. The Comparison between AIRM, AARM and AMS data observed from the Bandelier Tuff and Gold Point, Nevada

Bandelier Tuff

Site AIRM	N	K1	K2	K3	K1 Dec (°)	K1 Inc (°)	K2 Dec (°)	K2 Inc (°)	K3 Dec (°)	K3 Inc (°)	L=K1/K2	F=K2/K3	P=K1/K3
QBT05	10	1.042	1.013	0.945	95.8	5.2	4.8	11.2	210.3	77.6	1.028	1.072	1.103
QBT11	13	1.033	1.020	0.947	279.7	17.5	10	1	103.1	72.4	1.012	1.077	1.090
QBT18	10	1.027	1.006	0.966	302.9	21.1	34.4	3.8	134.1	68.6	1.021	1.041	1.063
QBT20	13	1.039	1.013	0.948	43.8	43.2	283.6	28.2	172.6	33.8	1.026	1.069	1.097

Site AARM	N	K1	K2	K3	K1 Dec (°)	K1 Inc (°)	K2 Dec (°)	K2 Inc (°)	K3 Dec (°)	K3 Inc (°)	L	F	P
QBT05	10	1.035	1.029	0.936	316.3	9.1	46.8	3.3	156.6	80.3	1.006	1.099	1.106
QBT11	13	1.054	1.003	0.943	343.7	3.2	75.4	28.2	247.6	61.5	1.050	1.064	1.118
QBT18	10	1.033	1.008	0.959	303.7	7.6	35.3	12.1	182.4	75.6	1.025	1.050	1.077
QBT20	13	1.039	1.015	0.946	293	0.1	203	7.3	23.5	82.7	1.023	1.073	1.098

Site AMS	N	K1	K2	K3	K1 Dec (°)	K1 Inc (°)	K2 Dec (°)	K2 Inc (°)	K3 Dec (°)	K3 Inc (°)	L	F	P
QBT05	62	1.011	1.008	0.981	277.1	0.9	187.1	1.8	34.1	88.0	1.004	1.027	1.034
QBT11	52	1.006	1.004	0.991	322.4	10.1	231.9	3.0	125.5	79.4	1.002	1.013	1.016
QBT18	32	1.006	1.003	0.991	285.3	12.2	194.9	1.8	96.8	77.6	1.004	1.013	1.017
QBT20	50	1.010	1.006	0.984	249.3	11.5	159.3	0.1	68.7	78.5	1.005	1.022	1.029

Gold Point

Site AIRM	N	K1	K2	K3	K1 Dec (°)	K1 Inc (°)	K2 Dec (°)	K2 Inc (°)	K3 Dec (°)	K3 Inc (°)	L=K1/K2	F=K2/K3	P=K1/K3
GP201	10	1.030	1.023	0.947	168.4	6.9	261.2	22.4	62.3	66.4	1.007	1.080	1.087
GP202	9	1.021	1.014	0.965	135	18.1	41.7	9.9	284.3	69.2	1.008	1.051	1.059
GP206	9	1.033	1.024	0.943	359.8	10.3	90.9	5.7	209.4	78.2	1.008	1.086	1.095
GP242	9	1.025	1.017	0.959	218.3	9.2	125.7	15.9	337.2	71.6	1.008	1.060	1.069
GP255	9	1.026	1.015	0.959	184.1	42.3	62.5	30	310.4	33	1.011	1.059	1.071
GP285	9	1.015	1.004	0.981	329.6	8.9	236.2	20.8	81.5	67.2	1.011	1.024	1.035
GP292	10	1.026	1.012	0.962	272.1	1.9	2.3	5	161.6	84.7	1.014	1.052	1.067

Site AARM	N	K1	K2	K3	K1 Dec (°)	K1 Inc (°)	K2 Dec (°)	K2 Inc (°)	K3 Dec (°)	K3 Inc (°)	L	F	P
GP201	9	1.030	1.001	0.969	266.2	12.4	174.5	7.6	53.6	75.4	1.029	1.032	1.062
GP202	10	1.151	1.099	0.751	325.5	26.7	225.8	18.5	105.2	56.6	1.047	1.464	1.533
GP206	9	1.046	1.021	0.933	47.8	46.3	275.0	33.0	167.3	25.1	1.024	1.095	1.122
GP242	9	1.074	1.019	0.907	13.5	55.1	109.9	4.4	203.0	34.5	1.054	1.125	1.185
GP255	10	1.122	1.038	0.839	194.7	11.3	345.3	77.1	103.4	6.1	1.081	1.125	1.337
GP285	8	1.009	0.998	0.993	241.4	40.7	128.9	24.0	17.2	39.8	1.012	1.005	1.017
GP292	10	1.025	1.015	0.961	291.5	9.5	201.3	1.1	104.5	80.4	1.010	1.056	1.066

Site AMS	N	K1	K2	K3	K1 Dec (°)	K1 Inc (°)	K2 Dec (°)	K2 Inc (°)	K3 Dec (°)	K3 Inc (°)	L	F	P
GP201	33	1.006	1.003	0.991	143.8	17.0	235.1	4.2	338.7	72.4	1.002	1.012	1.016
GP202	37	1.006	1.002	0.992	124.6	44.8	33.5	1.1	302.4	45.2	1.005	1.011	1.015
GP206	46	1.006	1.004	0.990	107.3	30.3	12.9	7.3	270.8	58.6	1.002	1.015	1.018
GP242	21	1.014	1.010	0.976	31.2	25.9	286.0	28.3	156.4	49.9	1.005	1.039	1.042
GP255	43	1.011	1.007	0.982	333.5	61.1	121.0	24.9	217.5	13.6	1.006	1.025	1.032
GP285	30	1.003	1.003	0.994	314.2	14.7	216.8	26.4	70.4	59.3	1.001	1.009	1.011
GP292	26	1.007	1.007	0.986	263.3	22.5	359.0	13.6	117.7	63.3	1.002	1.021	1.025

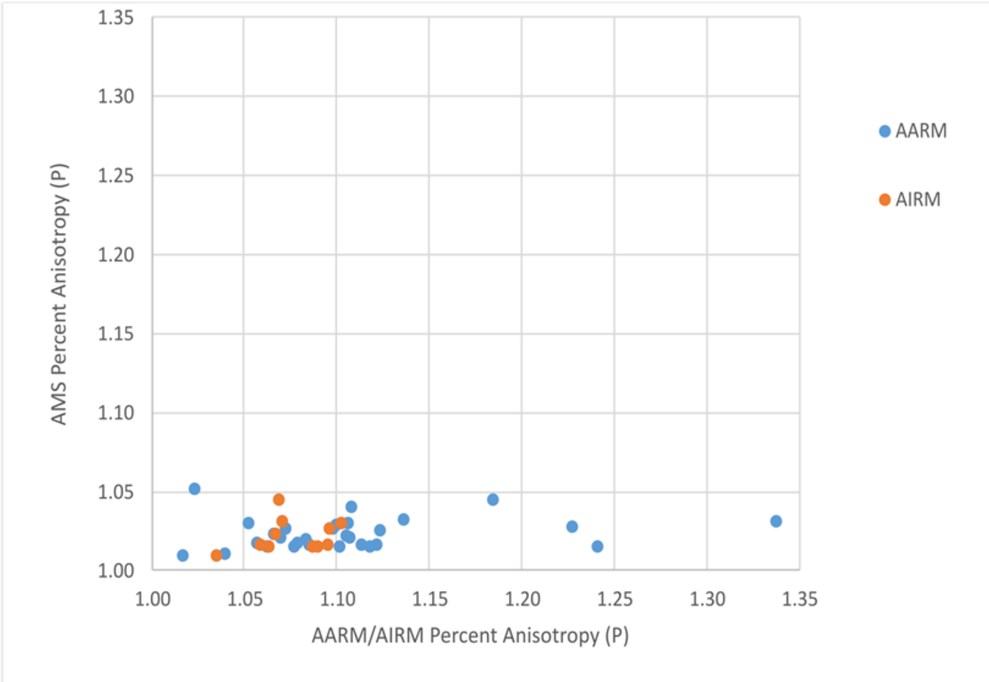

Figure 7.3. AMS P values compared to AARM and AIRM P values for Bandelier Tuff and Gold Point (GP) Tuffs.

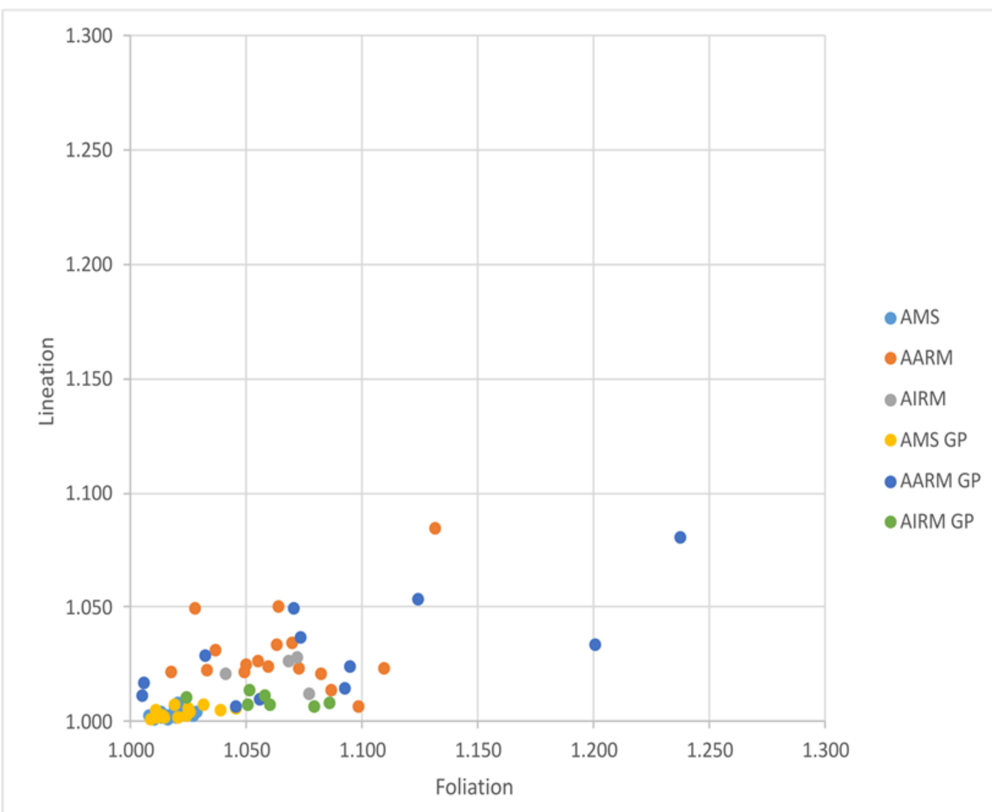

Figure 7.4. Lineation versus Foliation for Bandelier Tuff and Gold Point (GP) Tuffs.

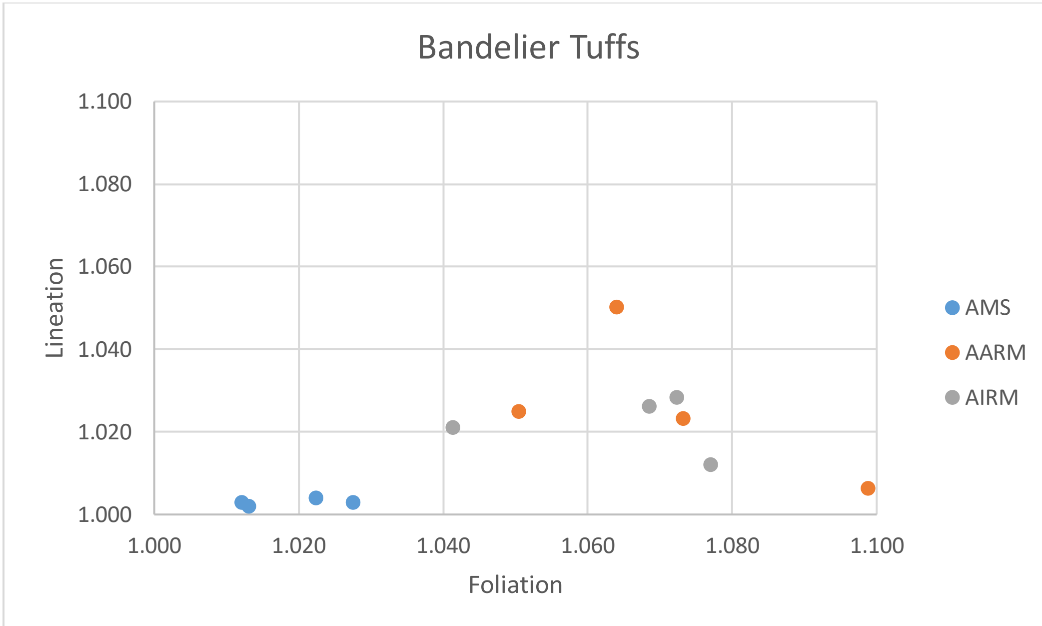

Figure 7.5. Lineation versus Foliation for Bandelier Tuff for the four selected sites with AMS and AMR results.

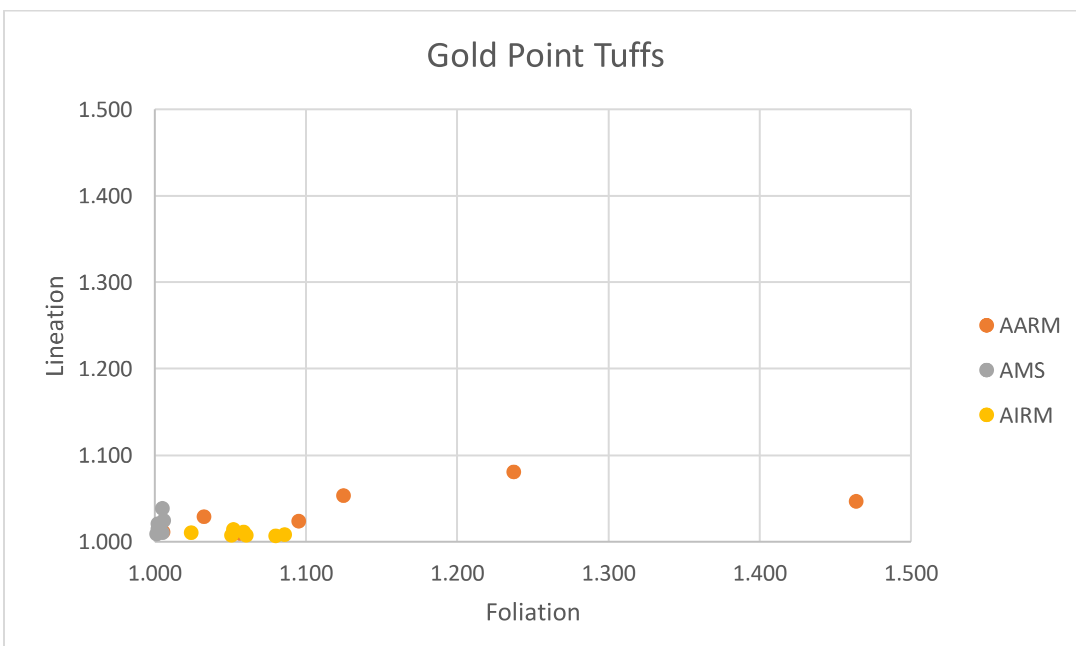

Figure 7.6. Lineation versus Foliation for Gold Point Tuffs for selected sites with AMS and AMR results.

Similarly, AARM and AIRM analysis were compiled for seven sites from the Gold Point area ignimbrites and compared to the AMS. A cross-plot of magnetic lineation versus foliation shows much higher values for AARM and AIRM than for AMS (Figure 7.6). All of the sites had some correlation when comparing the K1 AMS axis to the other K1 ARMs for the same site with the exception of site GP 206 (86%) (Figure 7.8). None of these had a matching inferred transport direction among the three methods. Four of the seven sites (57%) showed matching inferred transport directions along the K1 axis with AMS and AIRM, one site (GP 242) showed matching inferred transport directions of the K1 axis with AMS and AARM, and one site (GP 255) showed matching inferred transport directions of the K1 axis with the AIRM an AIRM only. Only four sites (57%) showed any matching inferred transport directions along the K3 imbrication orientation (Figure 7.9). Two sites (GP 202 and 285) show matching inferred transport directions along the K3 axis with AMS and AIRM, one site (GP 292) shows a matching inferred transport direction along the K3 axis with AMS and AARM, and one site (GP 201) shows a matching inferred transport direction along the K3 axis with AIRM and AARM only. Variability between the AMS, AIRM and AARM analysis could be due to changes in mineralogy or domain state of the magnetic grains.

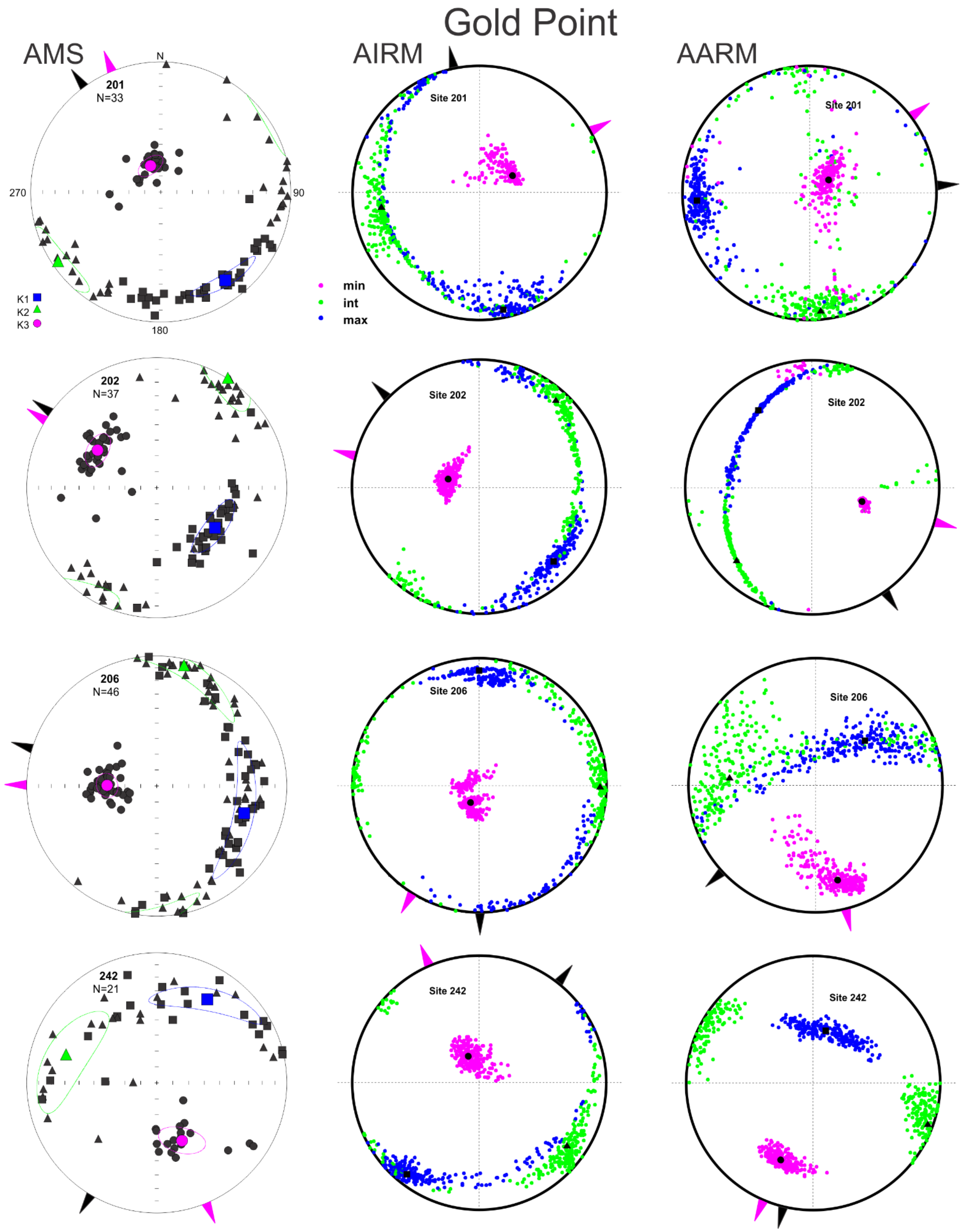
Gold Point
AMS
AIRM
AARM
N
201
N=33
270
90
180
K1
K2
K3
min
int
max
Site 201
202
N=37
Site 202
206
N=46
Site 206
242
N=21
Site 242

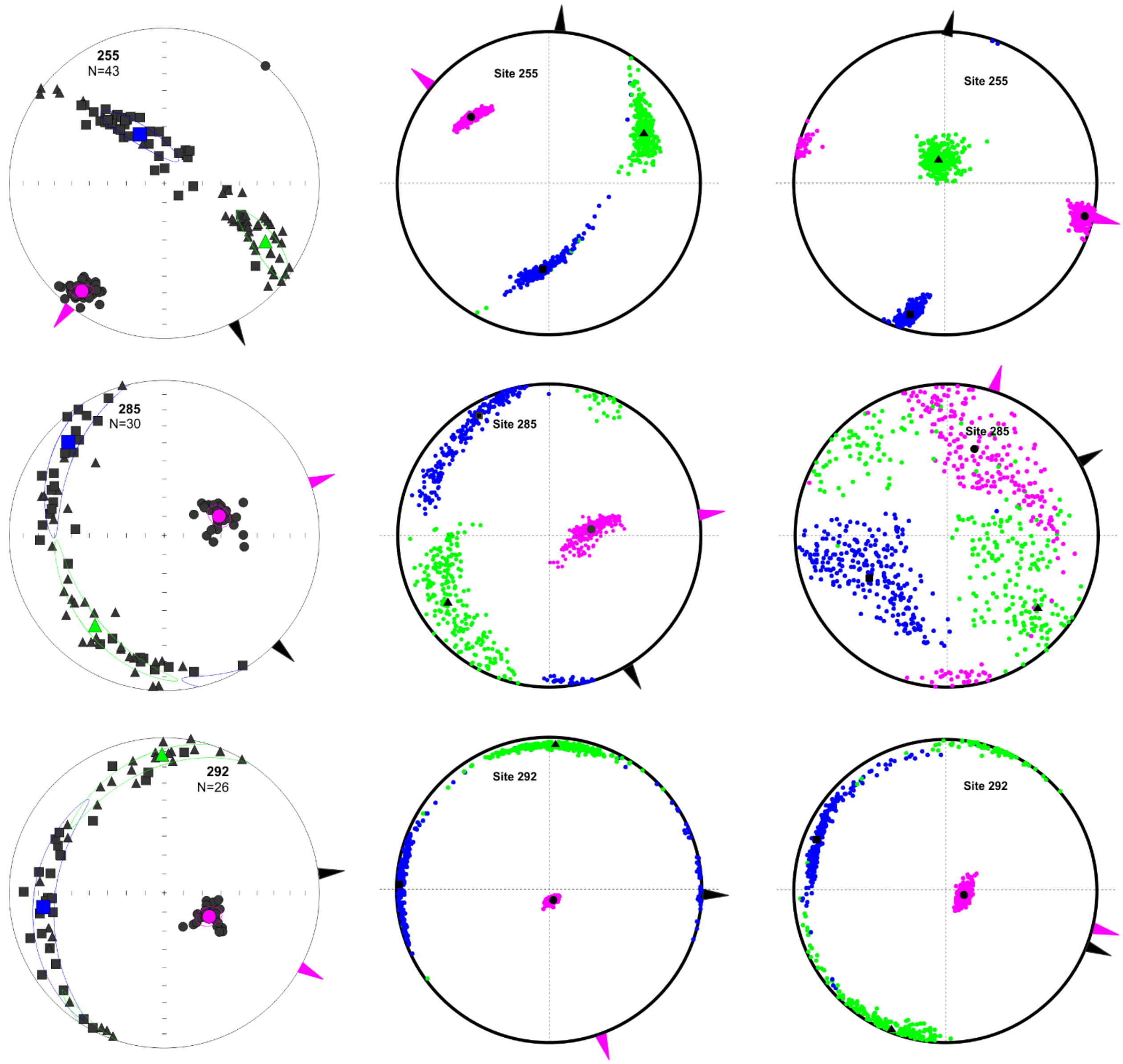

Figure 7.7. Comparison of AMS, AIRM, and AARM data with black arrows indicating K1 flow directions and pink arrows indicating K3 flow direction.

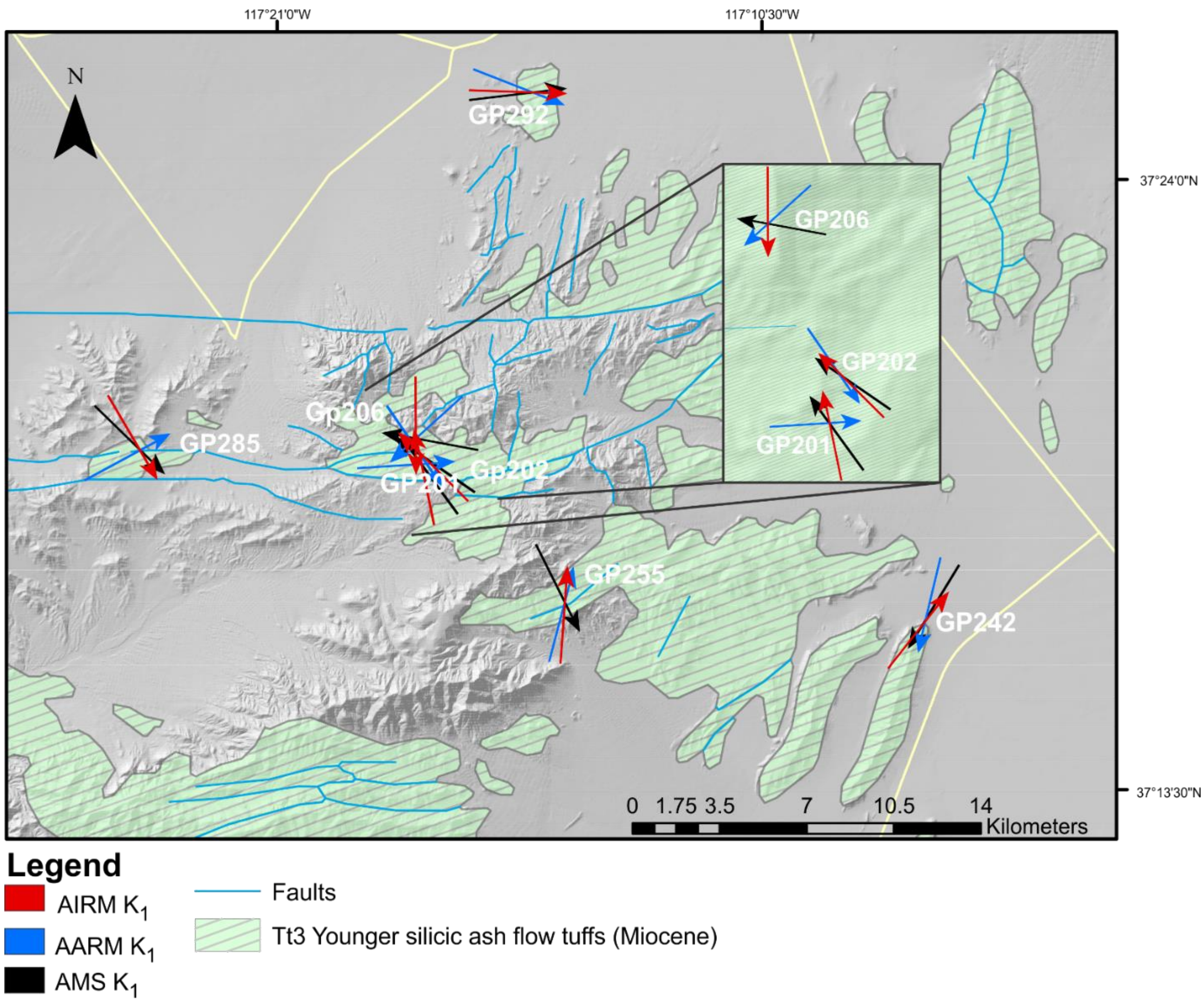

Figure 7.8. Map showing Gold Point Tuff comparisons of AMS, AIRM, and AARM data of inferred K_1 transport directions.

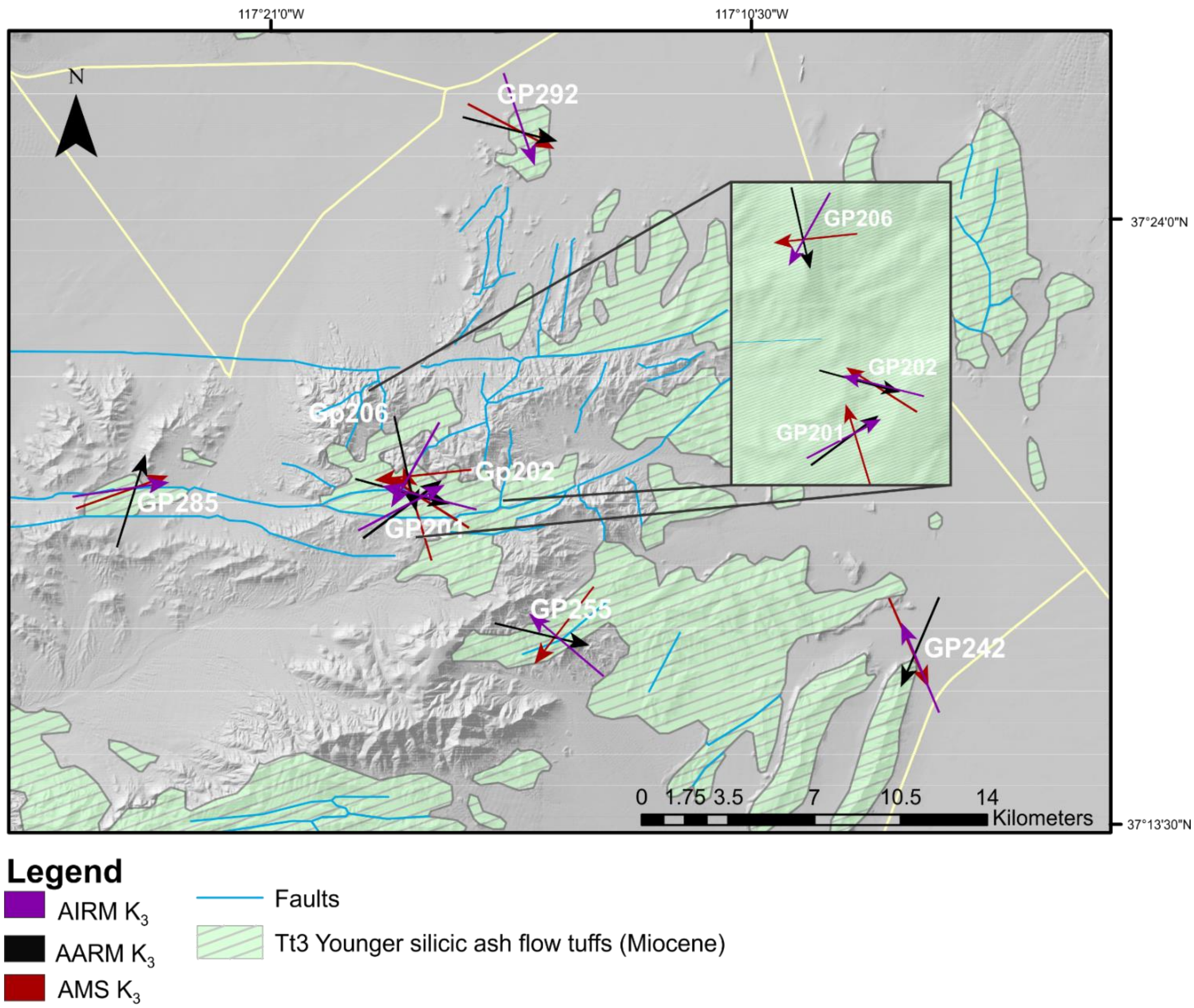

Figure 7.9. Map showing Gold Point comparison of AMS, AIRM, and AARM data with K_3 imbrication orientations.

CHAPTER 8

CONCLUSIONS

Selected exposures of the Quaternary Bandelier Tuff, exposed in the Jemez Mountains, New Mexico, and mid-Miocene ignimbrites in the southern Walker Lane, Gold Point area of the western Great Basin, Nevada, have been studied to systematically compare anisotropy of remanence (ARM) (mainly anhysteretic remanent magnetization, AARM and AIRM) with AMS data from the same sites. Twenty-one sites from the Bandelier Tuff and fourteen sites from the Gold Point area (Stonewall Flat Tuff – 6, Timber Mountain Tuff – 6, and Oriental Wash Tuff – 2) were tested to find out if the use of ARM was a reliable indicator for inferred transport directions when correlated with the AMS. Additionally, the study also compared the functionality of using the K_1 maximum susceptibility axis as the preferred indicator for inferred transport direction to using the K3 minimum susceptibility axis as the preferred indicator of imbrication orientation for inferred transport direction.

The AMS data showed results that implied this method could be used to successfully indicate the inferred transport/source directions when looking at the Bandelier Tuff, however AMS data from the Gold Point area ignimbrites showed only a few sites where data looked like it came from the anticipated sources. Though it is not apparent why the AMS for the Gold Point area ignimbrites don’t show a good correlation of the transport directions with the known sources, there could be many reasons why this is the case such as high relief paleotopography or vertical rotations from the tectonically active area.

This study showed the differences in using the K_1 maximum susceptibility axis as the preferred indicator for inferred transport direction to using the K3 minimum susceptibility axis as the preferred indicator of imbrication orientation for inferred transport direction. In general for the AMS data set shown, it was proven that for the Bandelier Tuff sites using the imbrication orientation as a proxy for inferred transport direction yielded better results than using the methodology of MacDonald and Palmer and others of using the K1 axis of maximum susceptibility as the indicator for transport/source directions.

Lastly, a comparison of AMS to ARM were done for both study areas. There were many differences found between both AARM and AIRM and between AMS and the two ARM methods including higher anisotropies between the AMS to the ARM methods, higher anisotropies from the AARM than the AIRM (Figure 7.3), and larger values of magnetic foliation than magnetic lineation for all the anisotropy methods used (Figure 7.4). More data is needed to fully understand the complex variations between the AARM and AIRM data, and how they compare to AMS. The four sites used for this study from the Bandelier tuff showed that using this methodology of combining AMS data with other ARM methods could be used to determine inferred transport/source directions, however, a larger scaled area around a known source with a larger spread of data points would be better suited for this investigation. In addition, without understanding of the paleomagnetic vertical axis reconstruction it is difficult to anticipate if the Gold Point area ignimbrites show data that is consistent with their source.

REFERENCES

http://www.agico.com/software/winsoft/cureval/

http://www.agico.com/software/winsoft/anisoft/

Agro, A., Zanella, E., Le-Pennec, J., and Temel, A., 2014, Magnetic fabric of ignimbrites: a case study from the Central Anatolian Volcanic Province: Geological Society, London, Special Publications, v. 396, SP396-9

Bath, G., 1868, Aeromagnetic anomalies related to remanent magnetism in volcanic rock, Nevada Test Site: Geological Society of America Memoirs, v. 110, p. 135-146.

Borradaile, G.J., and Henry, B., 1997, Tectonic applications of magnetic susceptibility and its anisotropy: Earth Sci. Rev. v. 42, p. 49-93.

Borradaile, G.J., 2001, Magnetic fabrics and petrofabrics: their orientation distributions and anisotropies: J. Struct. Geol., v. 23, p. 1581-1596.

Borradaile, G.J., and Jackson, M., 2004, Anisotropy of magnetic susceptibility (AMS): magnetic petrofabrics of deformed rocks: Geological Society, London, Special Publications, v. 238, p. 299-360.

Borradaile, G.J., and Jackson, M., 2010, Structural geology, petrofabrics and magnetic fabrics (AMS, AARM, AIRM): Journal of Structural Geology, v. 32, p. 1519-1551.

Broxton, D. E., and Reneau, S. L., 1995, Stratigraphic nomenclature of the Bandelier Tuff for the environmental restoration project at Los Alamos National Laboratory: Los Alamos National Laboratory Report LA-13010-MS, p 21.

Butler, R.F., 1992, Paleomagnetism: magnetic domains to geologic terranes: Blackwell Scientific Publications Boston.

Byers, F.M., Orkild, P.P., Carr, W.J., and Quinlivan, W.D., 1968, Timber Mountain Tuff, southern Nevada, and its relation to cauldron subsidence: Geological Society of America Memoirs, v. 110, p. 87-98.

Byers, F.M., Carr, W.J., and Orkild, P.P., 1989, Volcanic centers of southwestern Nevada: Evolution of understanding, 1960-1988: J. Geophs. Res. Solid Earth, v. 94, no. B5, p. 5908-5924.

Cagnoli, B., and Tarling, D.H., 1997, The reliability of anisotropy of magnetic susceptibility (AMS) data as flow direction indicators in friable base surge and ignimbrite deposits: Italian examples: J. of Vol. and Geoth. Res., v. 75, p. 309-320.

Christiansen, R.L., and Lipman, P.W., 1972, Cenozoic volcanism and plate-tectonic evolution of the western United States. II. Late Cenozoic: Philosophical Trans. of the Royal Soc. of London, v. 271, p. 249-284.

Christiansen et al. 1977, Timber Mountain- Oasis Valley caldera complex of southern Nevada: GSA Bulletin, v. 88, p. 943-959.

Constable, C., and Tauxe, L., 1990, The bootstrap for magnetic susceptibility tensors, J. Geophys. Res., v, 95, p. 8383-8395.

Crafford, A.E.J., 2007, Geologic Map of Nevada: U.S. Geological Survey Data Series 249, 1 CD-Rom, 46 p., 1 Plate.

Crowe, B. M., Linn, G. W., Heiken, G., & Bevier, M. L., 1978, Stratigraphy of the Bandelier Tuff in the Pajarito Plateau*:* Applications to waste management: Los Alamos National Laboratory Report LA-7225-M, p 57.

Day, R., Fuller, M., and Schmidt, V.A., 1977, Hesteresis properties of titanomagnetites: grain-size and compositional dependence: Physics of the Earth and Planetary Interiors, v. 13, n. 4, p. 260-267.

Doell, R.R., Dalrymble, G.B., Smith, R.L., and Bailey, R.A., 1968. Paleomagnetism, potassium-argon ages, and geology of rhyolites and associated rocks of the Valles caldera, New Mexico: GSA Memoirs, v. 116, p. 211-248.

Dunlop, D.J., 1995, Magnetism in rocks: Journal of Geophysical Research: Solid Earth, v. 100, n. B2, p. 2161-2174.

Dunlop, D.J., 2002, Theory and application of the Day plot (Mrs/Ms versus Hcr/Hc) 1. Theoretical curves and tests using titanomagnetite data: Journal of Geophysical Research: Solid Earth, v. 107, n. B3, EPM-4.

Ellwood, B. B. 1982. Estimates of flow direction for calc-alkaline welded tuffs and paleomagnetic data reliability from anisotropy of magnetic susceptibility measurements: Central San Juan Mountains, southwest Colorado: Earth and Planetary Sciences Letters, v. 59, p. 303–314.

Ferre, E.C., 2002, Theoretical models of intermediate and inverse AMS fabrics: Geophysical Research Letters, v. 29, n. 7, p. 31-1.

Fitter, T., 2014, Anisotropy of magnetic susceptibility (AMS) and anisotropy of remanent magnetization (ARM) data from Miocene ignimbrites, western Great Basin: A magnetic fabric study and comparison of magnetic fabric methods (UTD Thesis).

Fisher, R.V., 1990, Transport and deposition of a pyroclastic surge across an area of high relief: the 18 May 1980 eruption of Mount St. Helens, Washington: Geological Society of America Bulletin, v. 102, p. 1038-1054.

Fisher, R.V., Orsi, G., Ort, M., and Heiken, G., 1993, Mobility of a large-volume pyroclastic flow—emplacement of the Campanian ignimbrite, Italy: Journal of Volcanology and Geothermal Research, v. 56, n. 3, p. 205-220.

Gardner, J., and Goff, F., 1986, Stratigraphic relations and lithologic variations in the Jemez Volcanic Field, New Mexico: Journal of Geophys. Res., v. 91, n. B2, p. 1763-1778.

Gardner, J., Lavine, A., Wolde Gabriel, G., Krier, D., Vaniman, D., Caporuscio, F., Lewis, C., Reaneau, P., Kluk, E., and Snow, M., 1999. Structural Geology of the Northwestern Portion of Los Alamos National Laboratory, Rio Grande rift, New Mexico: Implications for Seismic Surface Rupture Potential from TA-3 to TA-55. United States: N. p. 1999. Web. doi:10.2172/8197.

Geissman, J.W., Holm, D., Harlan, S.S., and Embree, G.F., 2010, Rapid, high-temperature formation of large-scale rheomorphic structures in the 2.06 Ma Huckleberry Ridge Tuff, Idaho, USA: Geology, v. 38, i. 3, p. 263-266.

Hargraves, R.B., Johnson, D., and Chan, C.Y., 1991, Distribution Anisotropy: The cause of AMS in igneous rocks?: Geophysical Research Letters, v. 18, n. 12, p. 2193-2196.

Harrison, R.J., and Feinberg, J.M., 2008, FORCinel: An improved algorithm for calculating first-order reversal curve distributions using locally weighted regression smoothing: Geochem, Geophys, Geosys, v. 9, n. 5, p. 1-11.

Housen, B.A., Richter, C., and Van Der Pluijm, B.A., 1993, Composite magnetic anisotropy fabrics: experiments, numerical models and implications for the quantification of rock fabrics: Tectonophysics, v. 220, n. 1, p. 1-12.

Hrouda, F., 2010, Modeling relationship between bulk susceptibility and AMS in rocks consisting of two magnetic fractions represented by ferromagnetic and paramagnetic minerals-Implications for understanding magnetic fabrics in deformed rocks: J. of Geological Society of India, v. 75, n. 1, p. 254-266.

Hudson, M.R., Paleomagnetic data bearing on the origin of arcuate structures in the French-Peak-Massachusetts Mountain area of southern Nevada: GSA Bulletin, v. 104, p. 581-594.

Jackson, M., 1991, Anisotropy of magnetic remanence: A brief review of mineralogical sources, physical origins and geological applications, and comparison with susceptibility anisotropy: PAGEOPH, v. 136, p. 1-28.

Jackson, M., and Solheid, P., 2010, On the quantitative analysis and evaluation of magnetic hysteresis data: Geochem, Geophys, Geosys, v. 11, n. 4, p. 1-25.

Jelinek, V., 1978, Statistical processing of anisotropy of magnetic susceptibility measured on groups of specimens: Studia geophysica et geodaetica, v. 22, n. 1, p. 50-62.

Jelinek, V., 1981, Characterization of the magnetic fabric of rocks: Tectonophysics, v. 79, n. 3, p. 63-67.

Jezek, J., and Hrouda, F., 2004, Determination of the orientation of magnetic minerals from the anisotropy of magnetic susceptibility: Geol. Soc. London. Special Publications, v. 238, p. 9-20.

Le Pennec, J., Chen, Y., Diot, H., Froger, J., and Gourgaud, A., 1998, Interpretation of anisotropy of magnetic susceptibility fabric of ignimbrites in terms of kinematic and sedimentological mechanisms: An Anatolian case-study: Earth and Planetary Science Letters, v. 157, p. 105-127.

Lewis, C.J, Lavine, A., Reneau, S.L., Gardner, J.N., Channell, R., Criswell, C.W., 2002, Geology of the western part of Los Alamos National Laboratory (TA-3 to TA-16), Rio Grande Rift, New Mexico: United States: N.p., 1999.

Lewis, C.J., Gardner, J.N., Schultz-Fellenz, E.S., Lavine, A., Reneau, S., and Olig, S., 2009, Fault interaction and along-strike variation in throw in the Pajario fault system, Rio Grande rift, New Mexico: Geosphere, v. 5, n. 3, p. 252-269.

Lipman P.W., Dungan M.A., Brown L.L., and Deino A., Recurrent eruption and subsidence at the Platoro caldera complex, southeastern San Juan volcanic field, Colorado: New tales from old tuffs: GSA Bulletin, v. 108, n. 8, p. 1039-1055.

MacDonald, W.D., and Ellwood, B.B., 1987, Anisotropy of magnetic susceptibility: Sedimentological, igneous, and structural-tectonic applications: Reviews of Geophysics, v. 25, n. 5, p. 905-909.

MacDonald, W.D., and Palmer, H.C., 1990, Flow directions in ash-flow tuffs: a comparison of geological and magnetic susceptibility measurements, Tshirege member (upper Bandelier Tuff), Valles caldera, New Mexico, USA: Bulletin of Volcanology, v. 53, p. 45-59.

Martin-Hernandez, F., Luneburg, C.M., Aubourg, C., and Jackson, M., 2004, Magnetic fabric: methods and applications-an introduction: Geological Society, London, Special Publications, v. 238, p. 1-7.

Mason, S.N., 2011, Paleomagnetic and AMS results from Oligocene ash-flow tuffs of the eastern San Juan Mountains: implications for the evolution of the western margin of the San Luis Basin, Northern Rio Grande Rift (UNM Thesis)

McCabe, C., Jackson, M., and Ellwood, B.B., 1985, Magnetic anisotropy in the Trenton limestone: results of a new technique, anisotropy of anhysteretic susceptibility: Geophysical Research Letters, v. 12, n. 6, p. 333-336.

Mills, J.G., Saltoun, B.W., and Vogel, T.A., 1997, Magma batches in the Timber Mountain magmatic system, southwestern Nevada volcanic field, Nevada, USA: Journal of Volcanology and Geothermal Research, v. 78, n. 3, p. 185-208.

Moskowitz, B.M., 1991, Hitchhiker's guide to magnetism: Environmental Magnetism Workshop (IRM), v. 279, p. 48.

Muxworthy, A., Heslop, D., and Williams, W., 2004, Influence of magnetostatic interactions on first-order-reversal-curve (FORC) diagrams: a micromagnetic approach: Geophysical Journal International, v. 158, n. 3, p. 888-897.

Muxworthy, A.R., and Roberts, A.P., 2007, First-order reversal curve (FORC) Diagrams, Encyclopedia of Geomagnetism and Paleomagnetism, Springer, p. 266-272.

Muxworthy, A.R., and Williams, W., 2004, Distribution anisotropy: the influence of magnetic interactions on the anisotropy of magnetic remanence: Geological Society, London, Special Publications, v. 238, p. 37-47.

Noble, D.C., 1972, Some observations on the Cenozoic volcano-tectonic evolution of the Great Basin, western United States: Earth and Planetary Science Letters, v. 17, p. 142-150.

Noble, D.C., Vogel, T.A., Weiss, S.I, Erwin, J.W., McKee, E.H., and Younker, L.W., 1984, Stratigraphic relations and source areas of ash-flow sheets of the Black Mountain and Stonewall Mountain volcanic centers, Nevada: Journal of Geophysical Research, v. 89, n. B10, p. 8593-8602.

Oldow, J.S., Geissman, J.W., and Stockli, D.F., 2008, Evolution and strain reorganization within late Neogene structural stepovers linking the central Walker Lane and northern Eastern California shear zone, western Great Basin: International Geology Review, v. 50, n. 3, p. 270-290.

Ort, M.H., Newkirk, T.T, Vilas, J.F., and Vazquez, J.A., 2014, Towards the definition of AMS facies in the deposits of pyroclastic density currents: Geological Society, London, Special Publications, v. 396, SP396-8.

Ort, M.H., Orsi, G., Pappalardo, L., and Fisher, R.V., 2003, Anisotropy of magnetic susceptibility studies of depositional processes in the Campanian Ignimbrite, Italy: Bulletin of Volcanology, v. 65, p. 55-72.

Palmer, H.C., and MacDonald, W.D., 1999, Anisotropy of magnetic susceptibility in relation to source vents of ignimbrites: empirical observations: Tectonophysics, v. 307, p. 207-218.

Palmer, H.C., and MacDonald, W.D., 2002, The Northeast Nevada Volcanic Field: Magnetic properties and source implications: Journal of Geophys Res, v. 107, n. B11, doi:10.1029/2001JB000690, 2298.

Phillips, E.H., Goff, F., Kyle, P.R., McIntorsh, W.C., Dunbar, N.W., and Gardner, J.N., 2007, The $^{40}Ar/^{39}Ar$ age constraints on the duration of resurgence in the Valles caldera, New Mexico: Journal of Geophysical Research, v. 112, B08021, doi:10.1029,2006JB004511.

Pokorny, J., Suza, P., and Hrouda, F., 2004, Anisotropy of magnetic susceptibility of rocks measured in variable weak magnetic fields using the LKY-4S Kappabridge: Geological Society, London, Special Publications, v. 238, p. 69-76.

Pioli, L., Lanza, R., Ort, M., and Rosi, M., 2008, Magnetic fabric, welding texture and strain fabric in the Nuraxi Tuff, Sardinia, Italy: Bulletin of Volcanology, v. 70, n. 9, p. 1123-1137.

Potter, D.K., and Stephenson, A., 1990, Field-impressed anisotropies of magnetic susceptibility and remanence in minerals: Journal of Geophysical Research, Solid Earth, v. 95, n. B10, p. 15573-15588.

Potter, D.B., and Oberthal, C.M., 1987, Vent sites and flow directions of the Otowi ash flows (lower Bandelier Tuff), New Mexico: GSA Bulletin, v. 98, p. 66-76.

Quane, S.L., and Russell, J.K., 2005, Ranking welding intensity in pyroclastic deposits: Bulletin of Volcanology, v. 67, p. 129-143.

Roberts, A.P., Cui, Y., and Verosub, K.L., 1995, Wasp-waisted hysteresis loops: Mineral magnetic characteristics and discrimination of components in mixed magnetic systems: v. 100, n. B9, p. 17,909- 17,924.

Roberts, A.P., Pike, C.R., and Verosub, K.L., 2000, First-order reversal curve diagrams: A new tool for characterizing the magnetic properties of natural samples: Journal of Geophysical Research, Solid Earth, v. 105, n. B12, p. 28461-28475.

Rochette, P., Jackson, M., and Aubourg, C., 1992, Rock magnetism and the interpretation of anisotropy of magnetic susceptibility: Reviews of Geophysics, v. 30, 209-226.

Rochette, P., Aubourg, C., and Perrin, M., 1999, Is this magnetic fabric normal? A review and case studies in volcanic formations: Tectonophysics, v. 307, p. 219-234.

Sawyer, D. A., Fleck, R. J., Lanphere, M. A., Warren, R. G., Broxton, D. E., & Hudson, M. R., 1994. Episodic caldera volcanism in the Miocene southwestern Nevada volcanic field: Revised stratigraphic framework, 40Ar/39Ar geochronology, and implications for magmatism and extension. GSA Bulletin, v. 106(10), p 1304-1318.

Sawyer, D.A., Fleck, R.J., Lanphere, M.A., Warren, R.G., and Broxton, D.E., 1990, Episodic volcanism in the southwest Nevada volcanic field: New 40Ar/39Ar geochronologic results: EOS Trans. Am. Geophysical Union, v. 71, P. 1296

Spell et al., 1996, Cerro Toledo Rhyolite, Jemez Volcanic Field, New Mexico: $^{40}Ar/^{39}Ar$ geochronology of eruptions between two caldera-forming events: Geological Society of America Bulletin, v. 108, p. 1549-1566.

Smith, R.L., 1960, Ash flows: Geological Society of America Bulletin, v. 71, n. 6, p. 795-841.

Smith, R.L., and Bailey, R.A., 1966, The Bandelier Tuff: a study of ash-flow eruption cycles from zoned magma chambers: Bulletin of Volcanology, v. 29, p. 83-103.

Sparks, R., 1976, Grain size variations in ignimbrites and implications for the transport of pyroclastic flows: Sedimentology, v. 23, 147-188.

Stephenson, A., Sadikun, S., and Potter, D.K., 1986, A theoretical and experimental comparison of the anisotropies of magnetic susceptibility and remanence in rocks and minerals: Geophysical Journal International, v. 84, p. 185-200.

Stephenson, A., 1994, Distribution anisotropy: two models for magnetic lineation and foliation, Phys. of Earth and Planetary Interiors, v. 82, p. 49-53.

Stewart, J.H., and Carlson, J.E., 1978, Geologic Map of Nevada: U.S. Geological Survey and Nevada Bureau of Mines and Geology, 1:500,000 (not part of any formal series, printed and distributed by the U.S Geological Survey, G75163, reprinted 1981, G81386).

Sussman, A.J., Lewis, C.J., Mason, S.N., Geissman, G.J., Schultz-Fellenz, E., Olivia-Urcia, B., Gardner, J., 2011, Paleomagnetism of the Quaternary Bandelier Tuff: Implications for the tectonic evolution of the Espanola Basin, Rio Grande rift: Lithosphere, v. 3, n. 5, p. 328-345.

Tauxe, L., and Mullender, T., and Pick, T., 1996, Potbellies, wasp-waists, and superparamagnetism in magnetic hysteresis: Journal of Geophysical Research, Solid Earth, v. 101, n. B1, p. 571-583.

Turbeville, B.N., and Self, S., 1988, San Diego Canyon ignimbrites: Pre-Bandelier tuff explosive rhyolitic volcanism in the Jemez Mountains, New Mexico: Journal of Geophysical Research, Solid Earth, v. 93, n. B6, p. 6148-6156.

Valentine, G.A., 1987, Stratified Flow in pyroclastic surges: Bulletin of Volcanology, v. 49, n. 4, 616-630.

Weiss et al., 1993, Neogene tectonism from the Southwestern Nevada Volcanic Field to the White Mountains, California. Part 1. Miocene volcanic stratigraphy, paleotopography, and extensional faulting and uplift between northern Death Valley and Pahute Mesa: Cordilleran/Rocky Mountain Section, GSA Guidebook, Department of Geological Sciences, University of Nevada, Reno, P. 353-382.

Weiss, S.I., and Noble, D.C., 1989, Stonewall Mountain Volcanic Center, Southern Nevada: stratigraphic, structural and facies relations of outflow sheets, near-vent tuffs, and intracaldera units: Journal of Geophysical Research, v. 94, p. 6059-6074.

Wilson, C., and Walker, G., 1982, Ignimbrite depositional facies: the anatomy of a pyroclastic flow: Journal of the Geological Society, v. 139, n. 5, 581-592.

Worthington, J.E., 1992, Neogene structural and volcanic geology of the Gold Mountain-Slate Ridge area, Esmeralda County, Nevada [M.S. thesis]: Reno, Nevada, University of Nevada, Reno, 76p.

Wright, J.V., and Walker, G.P.L., 1981, Eruption, transport and deposition of ignimbrite: a case study from Mexico: Journal of Volcanology and Geothermal Research, v. 9, p. 111-131.

BIOGRAPHICAL SKETCH

Ranyah Lycka was born in Wichita, Kansas in 1988. She moved to Dallas as a young child and graduated from Allen High School, Allen, Texas in 2007. Ranyah continued her undergraduate studies, which she began while in high school for dual credit. In 2008, she was admitted to the Arts and Technology (ATEC) undergraduate program at The University of Texas at Dallas. While in the ATEC program, she began doing research within the geosciences department, Cybermapping Lab, involved with three-dimensional modeling of virtual geological outcrops. She graduated with a B.A in ATEC and a minor in geosciences in the fall of 2011. Ranyah was admitted to the Geosciences Master's program in the spring of 2012 where she began working with Dr. John Geissman in the paleomagnetism lab. She remained very active, while simultaneously working on graduate research she started an American Association of Petroleum Geologists (AAPG) Student Chapter at the university and served as the President for a year and a half during which she planned field trips to visit conventional and unconventional drilling operations, organized trips to national meetings and recruiting events, and generated $8,000 in funds. Concurrently she was on the steering committee for the Dallas Geological Society Young Professionals group after which she took over as chair of the YP's for the 2015-2016 year. Ranyah has developed professionally with internships at Laredo Petroleum summer 2014, Bell and Murphy and Reed Engineering Group in summer 2015, and Kalnin Ventures Fall 2016, and by presenting a poster related to her thesis topic at American Geophysical Union (AGU), and attending monthly and yearly continued education seminars and lectures put on by Dallas geological society, AAPG and Society for Exploration Geophysicists (SEG).

CURRICULUM VITAE

Ranyah Lycka

Education and Qualifications

Master's Degree in Geosciences (Paleomagnetism and Rock Magnetism)

The University of Texas at Dallas, Richardson, TX (GPA 3.601/4.0) *08/2017*

- Rock magnetic research of pyroclastic deposits; investigating the magnetic mineral grain fabric in order to understand particle alignment and transport direction of ignimbrites. Studying the comparison of ignimbrite sequences near Gold Point, Nevada in the western Great Basin and the Bandelier Tuff in the Jemez Mountains, New Mexico.

Prizes:

- GSA research Grant-In Aid recipient, 2013
- NSM- Pioneer Nat. Resources Scholarships, 2011-2013

B.A Arts & Technology

The University of Texas at Dallas, Richardson, TX (GPA 3.443/4.0) *Jan 2008-Dec 2011*

- 2011: Paleomagnetic Field work in Central Great Basin near Gold Point, Nevada
- 2011: Vz400 Operations Certificate – trained for acquisition and processing with Riegl VZ-400
- 2010: NSM- Geos/ 3D – Digital Scholarship
- 2010: Hales Fellowship Scholarship

Work Experience and Volunteer Work

<u>Oct 2016 – Present Contract Geologist at Kalnin Ventures</u>

- Overseeing project and environmental due diligence for new acquisitions
- Manage company geological database and generates geologic maps
- Interpret logs and create structural, isopach, and OGIP maps

<u>Feb 2016 – Oct 2016 Environmental Geologist at Reed Engineering Group</u>

- Primary focus includes providing environmental services related to real estate due diligence and closure of contaminated properties through the Texas Commission on Environmental Quality (TCEQ)
- Perform all aspects of a Phase I and Phase II Environmental Site Assessment (ESA). Responsibilities include technical oversight, project coordination, site inspection, regulatory database review, report preparation and completion of field activates including soil and groundwater sampling.
- Evaluated and completed multiple Phase I ESA's for various properties throughout the Dallas-Fort Worth Metroplex including vacant/undeveloped land and developed commercial sites.

May 2015 – Mar 2016 Geophysical Intern at Bell & Murphy and Associates

- International oil exploration in Cooper Basin in South Australia and Queensland, Australia.
- Domestic oil exploration projects throughout Grayson County, Harris County, Jack County, and Young County, Texas for various clients.
- Duties include seismic interpretation, logging suite interpretation, data loading into SMT Kingdom, and generating geological prospect maps for clients.

2015 - Geotechnical Engineering Intern at Reed engineering Group, Dallas TX

- Major project evaluating a limestone bluff slope failure at Lake Whitney, TX
- Daily work: wrote up proposals for clients, set up geotechnical drilling jobs, and logged cores.
-

2011 - Present Graduate research assistant

- Teaching assistant for three consecutive summer Field Geology courses : 2013, 2014 & 2015
- Teaching assistant for Intro/physical Geology Lab spring 2015 and Fall 2016
- Presented research results at the American Geophysical Union (AGU), Dec-2013
-

2014 - Geophysical Intern at Laredo Petroleum

- Mapped and evaluated the shallow Clearfork formation in the Midland Basin while using geological (Petra) and geophysical (SMT Kingdom) software.
- Obtained invaluable Experience working in a corporate environment
-

2010 - 2011 Undergraduate Research assistant

- The Digital integrated Stratigraphy Project –Wales, UK, 2011
- Galveston Island Terrestrial Scanning Survey – 2011
- Historical Preservation of WWII Corsair Bomber Plane by Laser Scanning- Cavanaugh Flight Museum- 2010
- Data post processing from SAUDI Aramco Project – MAY 2010
-

Achievements, Interests and Skills

- Dallas Geological Society Young Professionals Chair 2015-2016
- President of AAPG UT-Dallas Student Chapter 2013-2014
- Started the inaugural Southwest Section IBA team for UT Dallas, 2014
- Steering committee member for the Young Professionals group in the Dallas area. 2013-15
- Member of AAPG, GSA, SEG, AGU, DGGS
- First-Aid/CPR Certified
- Languages: English and Arabic

- Certified 200hr Yoga Teacher
- Proficient in using Paleomagnetic instrumentation, and using a plethora of analytical and graphical software
  Published: MUNNECKE, A., CRAMER, B.D., BOON, D.P., KHARWAT, R., AIKEN, C.L. & SCHOFIELD, D.I. 2012. The Digital Integrated Stratigraphy Project (DISP). Bulletin of Geosciences 87(4), 705–712. DOI 10.3140/bull.geosci.1318
- Taught the geology merit badge for boy scouts
- SEG-SEP Travel Grant, ExxonMobil Geophysical "Subsurface Integration" short course Nov. 2012
- ExxonMobil Permian Basin Field Course (Guadalupe Mountains) April 2013